



**Experimental and Theoretical Characterization of
Negative Deuterium Ion Distributions in a
Gridded Inertial-Electrostatic Confinement Device**

Eric C. Alderson

August 2012

UWFDM-1415

Ph.D. thesis.

**FUSION TECHNOLOGY INSTITUTE
UNIVERSITY OF WISCONSIN
MADISON WISCONSIN**

**Experimental and Theoretical Characterization of
Negative Deuterium Ion Distributions in a Gridded
Inertial-Electrostatic Confinement Device**

Eric C. Alderson

Fusion Technology Institute
University of Wisconsin
1500 Engineering Drive
Madison, WI 53706

<http://fti.neep.wisc.edu>

August 2012

UWFDM-1415

Ph.D. thesis.

Experimental and Theoretical
Characterization of Negative Deuterium Ion
Distributions in a Gridded
Inertial-Electrostatic Confinement Device

by:

Eric C. Alderson

A dissertation submitted in partial fulfillment of
the requirements for the degree of
Doctor of Philosophy

(Electrical and Computer Engineering)

at the

University of Wisconsin – Madison

2012

Date of final oral examination: 8/3/2012

Dissertation approved by the following members of the Final Oral Committee:
David T. Anderson, Professor, Electrical and Computer Engineering
Gerald L. Kulcinski, Professor, Nuclear Engineering – Engineering Physics
John F. Santarius, Research Professor, Nuclear Engineering – Engineering Physics
Amy E. Wendt, Professor, Electrical and Computer Engineering
Gregory A. Moses, Professor, Nuclear Engineering – Engineering Physics

Abstract

The research described in this dissertation was performed in the UW-Madison Inertial Electrostatic Confinement (IEC) fusion research laboratory at the University of Wisconsin-Madison, in pursuit of a doctoral degree from the Electrical and Computer Engineering Department. This work extends the 2008 discovery and subsequent studies of a significant negative ion current produced in a gridded IEC device operating with deuterium fuel. This study has been carried out through experimental, analytical, and computational research as described below.

The discovery of a significant negative ion current in a gridded IEC device immediately prompted exploration of this phenomenon. Studies were carried out on the energy spectrum of the negative ion current. Following this, studies were made of the magnitude and changes in the negative ion current density in response to the IEC device cathode potential, current supplied to the cathode, and background pressure. While early examination showed the negative ion current varies in response to the orientation of the cathode, the early research was limited to two cathode orientations.

Because the cathode of a gridded IEC device has structure, electrostatic potential in an IEC device is a rippled profile with the strongest potential at the surface of the grid-wires, and dips in potential

between the grid-wires. This rippled potential induces channels through-which negatively charged particles tend to travel, producing jets. While these jets have been observed in some of the earliest IEC device experiments, the profiles of these jets have never been directly measured before this thesis work.

This work measures the outgoing negative ion current with a mobile Faraday cup to produce the first measurements of the IEC device jet azimuthal profile. It also measures the negative ion radial profile to produce the first measurements of how negative ion current density in the jet changes with radius outside the anode. These measurements show that the profile of the negative ions in the jet is a function of cathode potential, showing more peaking at higher potential in the range examined. The negative ion current showed a purely linear response to current supplied to the cathode between 15 and 45 mA. Extrapolations of the negative ion current in the jet studied show the total negative ion current leaving the jet is on the order of 0.3-0.4% of the current supplied to the cathode.

This thesis work also explores the mean free path analog of a sequence of reactions. Such study is relevant to negative ion research because negative ions can be produced by a reaction chain of positive ion to fast neutral to negative ion. Comparing the importance of this sequence of reactions with a single step reaction from positive ion to negative ion was undertaken by a series of analytic derivations and showed that the chain of

reactions was the dominant path for negative ion creation, even though the fast neutrals are not confined. This analysis was extended to an arbitrary number of reactions and is applicable to a wide field of study.

Negative ion modeling capabilities were added to the Voltera Integral Code for Transport in Electrostatic Reactors (VICTER) code. This one dimensional code modeled ion and fast neutral currents in an IEC device and predicts fusion rates and radial distributions. Adding negative ion modeling to this code improves the VICTER code's accuracy, enables parametric studies of negative ion production in an IEC device, and provides another avenue to benchmark the accuracy of the VICTER code. Benchmarking shows good agreement with the negative ion current response to supplied cathode current and distance from the cathode. Similar trends in response to changes in cathode potential have also been demonstrated.

Acknowledgments

It is daunting to consider all the people who deserve acknowledgment for their contribution to this work. Those who have primarily shaped my graduate academic career will receive first recognition, then those outside my research group who have aided my research, and finally my loved ones; for brevity numerous worthy contributors will be neglected, but I pray they know my gratitude is genuine, even if they are not specifically named here.

It is proper that my first acknowledgment goes to my research advisor Gerald Kulcinski, whose faith in me and direction has shaped my career as a researcher more than any other. Professor David Anderson has been helpful as an academic advisor and his recommendations, academic or professional, have always been welcome. The assistance of John Santarius has been invaluable; I hope we can continue to collaborate in the future. Working with Gil Emmert has been rewarding and instructive. I thank the experimentalist members of the UW-IEC research laboratory, past and present. I would specifically like to thank those I have had the privilege of working with: Bob Ashley, Richard Bonomo, Alex Wehmeyer, Tracy Radel, Gregory Piefer, Ross Radel, Logan Campbell, Carlos Paz-Soldan, John Sorebo, Zachary Courter, Sam Zenobia, Brian Egle, David Donovan, Gabriel Becerra, Lauren Garrison, Matt Micalak, Craig Schuff, Aaron McEvoy, and Karla Hall. Special thanks goes to my colleague David Boris, whoes work

became the foundation that this dissertation built from; it has been a true pleasure to collaborate with him. Working with the UW-IEC research group has been more rewarding than I could have imagined when I first came to the University of Wisconsin-Madison.

I am please to also extend acknowledgments to those outside of the UW-IEC group who have contributed to my research. Arthur Phelps provided cross sections gathered in the course of his research that were extremely helpful in the computational research carried out in this work. Joe Khachan provided guidance that was instrumental to my M.S. work, and deserves another acknowledgment here. Thanks also goes to the unnamed reviewer who provided a suggestion to my and Santarius' paper that simplified the algebra of the derivation presented in Chapter III.

Finally, I have overwhelming gratitude for my loved ones. My aunts, uncles, cousins, and grandparents have always been there for me and I am grateful. I offer my thanks (even if they can't read this) to my in-laws who have always been loving and supportive. My sister has been my longest friend, and I know I am lucky to have her in my life. My parents have shaped me, and just as importantly, made me believe that I can overcome obstacles in the way of what I want; I would not be here if you did not believe I could be here. My dearest Dacīte has always supported me, loved me, given me strength, and has given me a family. Liels paldies, mana mīļā! Mūsu piedzīvojums ir tikai sācies.

Table of Contents

Abstract	i
Acknowledgments	iv
Table of Contents	vi
Table of Figures	viii
Table of Tables	xxiii
Chapter I: Introduction	1
Chapter II: Previous work	7
II.1: Inertial Electrostatic Confinement device background	7
II.2: Negative ion reactions and background	13
II.3: Negative ion measurements in an IEC device	27
Chapter III: Analytic determination of the mean free path of sequential reactions	44
III.1: Mean free path for a single reaction	44
III.2: Two step sequential mean free path	46
II.3: Sequential mean free path of arbitrarily high number of collisions	51
II.4: Sequential mean free path applied to currents in an IEC device	54
Chapter IV: Negative ion physics in the VICTER code	60
IV.1 VICTER code background	60
IV.2 Negative ion physics implementation in the VICTER code	67
Chapter V: Experimental approach	80
V.1 Laboratory facility	80
V.2 HOMER IEC Device	82
V.3 High voltage switch	84
V.4: Design of a movable Faraday cup for use in the HOMER	94

IEC device	
Chapter VI: Results	114
VI.1: VICTER negative ion results	114
VI.2: Faraday cup measurements	120
Chapter VII: Discussion of results	160
VII.1: Experimental and modeling energy spectrum comparisons	160
VII.2: Experimental and modeling parametric comparisons	167
VII.3: Negative ion jet profiles and extrapolations	180
Chapter VIII: Conclusions	191
VIII.1: Measurements of negative ions in an IEC device	191
VIII.2: Negative ion subroutine in the VICTER code	193
VIII.3: Related work	195
Chapter IX: Future work	196

Table of Figures

Figure Caption	page
II-1: Sketch of generic IEC device geometry and potential profile – not to scale.	11
II-2: A graph of the total cross sections that give rise to hydrogenic fast neutrals	16
II-3: Graph of deuterium negative ion creation charge exchange cross sections on a background of D2target gas.	18
II-4: The cross sections for the dissociative electron attachment reaction for a variety of target hydrogen molecule vibrational states. “v” is the vibrational quantum number of the H2 molecule.	19
II-5: Cross sections for destruction of deuterium negative ions through collision with molecular background gas	24
II-6: Cross section of hydrogen negative ion photodetachment as a function of photon energy.	25
II-7: Electron attachment cross section for hydrogen (teal pentagons) and detachment cross section for negative ion collision with an electron (red diamonds). Assuming the electron is the projectile, the cross section should be unchanged for deuterium	26
II-8: Photograph of a gridded IEC device operating in a regime to exhibit visible plasma jets [II-42].	28
II-9: IEC device cathode with a single enlarged grid hole. The jet emanating from the large hole is dominant, to the point that the other jets are not visible.	30
II-10: Spectroscopic Doppler shift results of fast neutral particles in the IEC device, offset by distance from the cathode center.	31
II-11: Method for calibrating the energy of the measured negative ion current with the applied magnetic field in the Magnetic Deflection Energy Analyzer. (Left) curve showing simulation results and equation fitting the curve. (Right) the result of a SIMION simulation used to develop the calibration curve.	34

II-12: (a) Illustration of the Magnetic Deflection Energy Analyzer, aligned so the negative ion jet is first reduced by a pair of 2 mm collimation irises, then bent by the field of an electromagnet, (b) then collimated by a pair of 100 μm diameter holes and then detected by a solid state charged particle detector.	35
II-13: The results of the Magnetic Deflection Energy Analyzer measurement of the negative ion energy spectrum at a variety of cathode voltages, in a system with a 20 cm cathode and 50 cm anode, at 2 mTorr background pressure, and 30 mA cathode current. Each cathode voltage is offset by 0.1 a.u..	36
II-14: Negative ion energy spectrum measured by the Magnetic Deflection Energy Analyzer, and decomposed into 5 Gaussians, the centroid of each listed as c_1 - c_5	37
II-15: Diagram of Faraday Trap used to measure negative ion current produced by HOMER IEC device.	38
III-1: Diagram of current evolution where I_1 produces I_2 , which produces I_3 . The currents produced by I_1 other than I_2 are summed into the current I_1' and the currents produced by I_2 other than I_3 are summed into the current I_2' . The mean free path for a particle of species 1 to produce a particle of species 3 is denoted by λ_{13} .	48
III-2: Sequential mean free path for three species of ions to become atomic fast neutrals and those fast neutrals to become negative ions in a 2 mTorr D ₂ gas at room temperature, where the ions start with a kinetic energy between 5 to 100 keV, and undergo no acceleration	55
II-3: A plot of the mean free path for the reaction of an ion to collide with neutral D ₂ and become a negative ion directly, through a double electron capture in a 2 mTorr D ₂ gas at room temperature. The y-axis is in logarithmic scale. This plot shows the mean free path for double electron capture is much longer than the sequential mean free path for an ion to produce a fast neutral, which becomes a negative ion. An ion would have to undergo hundreds of passes before it reached a path length that is a significant fraction of the mean free path for creation of negative ions.	57
III-4: Sequential mean free path for atomic ions to produce	58

atomic fast neutrals and those fast neutrals to become atomic ions in a 2 mTorr D ₂ gas at room temperature, when the particles have between 5 to 100 keV of kinetic energy.	
IV-1: Graphical depiction of current sources and how they are described by the kernel used in Eqn. IV- 1. The blue arrow (fine dotted line) represents the path of the sum of current sources for currents born inward at radial bin r from currents born at radial bin r', while the red arrow (dashed line) represents the path of the sum of current sources for the currents born inward at radial bin r from currents born at radial bin r'. The arrows in the diagram omit the oscillations from r' to the center-line before the final pass to react in radial bin r.	63
IV-2: Example input file for the molecular version of the VICTER code; after defining each parameter, that parameter is described by the following bracketed statement. The switches control how the system is modeled and what optional results are calculated. The physical parameters define the physical system modeled. The grid mesh defines the energy and radial resolution the code uses to model the system.	67
IV-3: Cross section for creation of negative deuterium ions by charge exchange from each parent species (left) and electron stripping of deuterium negative ions (right)	70
IV-4: The three types of negative ion trajectories, as dependent on total energy and direction. Cathode potential energy is outlined in blue. Negative ions of type (1) are born traveling outward, and are accelerated outward as the the electrostatic potential increases. Negative ions of type (2) are born traveling inward with enough energy to reach the cathode, decelerating as they approach the cathode, pass through the cathode and accelerate outward. Negative ions of type (3) do not have enough energy to reach the cathode, decelerating until they reach a turning point of zero kinetic energy and then accelerate out. The energy of the outward portion of the inward born currents are the same as the inward portion of these currents, but are offset for clarity.	72
V-1: The four experimental devices in the UW-IEC laboratory	80

	clock-wise from the top left: HOMER, HELIOS, MITE-E, and SIGFE.	
V-2:	Diagram of the HOMER Inertial Electrostatic Confinement device	82
V-3:	Diagram of resistor system, with shield made transparent. The printed circuit boards are green and the resistors are the white 'fins'. The strings of resistors are arranged in a pentagon, each face a continuous string. At the top is a switch assembly to engage or disengage the strings from the power supply to the shield which is connected to an experiment. One of the switch pins controls a short that bypasses the resistors altogether.	88
V-4:	Electrode arrangement and grounded tank laid out in Maxwell-3D™. The large L-shaped assembly holds the resistor strings within, the top of which is connected by high voltage cable to the power supply. This electrode is connected by a high voltage cable that runs along the z-axis to the selector electrode, which is connected by the shown bridge electrode (the other three bridge electrodes are not shown) to the chamber electrode which is connected by cable to an experiment by a high voltage cable. Only the connected chamber electrode is at voltage, the others are grounded	90
V -5:	Electrostatic fields in switch as modeled in Maxwell-3D™ with 300 kV applied to the electrodes. Left shows fields in the plane of the bridge electrode axis, right shows the field in the YZ-plane.	91
V-6:	Left: SolidWorks design of a set of connected electrodes with support structure. Right: the constructed electrodes, hanging with support structure from the lid of the switch as they are installed in the switch. The selector electrode and bridge electrode are covered in a plastic wrap to protect the copper plating on the aluminum electrode bodies during assembly.	92
V-7:	(Left) Full SolidWorks assembly of the high voltage switch design; on the rear wall of the tank is the pulsing system, which is engaged by rotating the rod and ball into contact with the resistor shield electrode. (Right) Constructed switch elements before installation in the switch tank for initial testing. The tank and the pulsing	93

system are not shown here.	
V-8: Results of a Maxwell-3D™ simulation of the potential at the equator of an IEC device with a cathode of 20 cm diameter at applied potential of 90 kV and anode of 30 cm diameter at ground potential. This simulation shows a nearly 30% dip in potential between the cathode wires Inset top is an isometric view of the simulated anode and cathode grids and inset bottom is a top down view of the simulation. Note, only two latitude lines are included in the simulation to reduce complexity of the simulation. It is expected the latitude lines far from the equator have less influence on the potential at the equator	96
V-9: Maxwell-3D™ magnetostatics model of two K&J Magnetics BX082SH magnets held 3.3 cm apart, with the magnetic scale truncated above 300 Gauss to show that thermal ions will not penetrate to the collection aperture.	102
V-10: Maxwell-3D™ magnetostatics model of two K&J Magnetics BX082SH magnets held 3.3 cm apart with the magnetic scale truncated above 3400 Gauss to show that energetic negative ions will penetrate to the collection aperture.	102
V-11: Isometric through-cut diagram of the Faraday cup showing magnets (black), front aperture, front case, ceramic spacer, secondary electron suppression electrode, ceramic spacer, collection electrode, ceramic spacer, and rear case. The rear hole is for mounting, with a set screw hole shown. Inset is a diagram of the assembled Faraday cup, without the shroud.	105
V-12: Assembled Faraday cup, without magnets or shroud.	106
V-13: Picture of Faraday cup installed for radial measurement. A ceramic stand off isolates the metal tube of the feed-through from the case of the Faraday cup. This image shows the Mu-metal shroud, held in place by a hose clamp.	108
V-14: Picture of azimuthal scan system. The Faraday cup mounting pivots on a bearing in the center of the chamber. This bearing is connected by chain to a rotational feed-through (behind the mesh on the bottom left hand corner of the picture). The Faraday cup and	109

mounting is counterbalanced by stainless steel weights (off frame on the bottom of the picture). The range of motion of the azimuthal scanning system is limited by the grids that shield the filaments.	
V-15: Illustration of field of view of azimuthal Faraday cup scanning mount. Shown is 20 cm diameter cathode grid to illustrate that two jets and part of a third are in the azimuthal mount's field of view.	111
V-16: Collage of Faraday cup positioning reference pictures. The vertical black line shows the center of the central jet in the field of view of the Faraday cup. The blue line shows the positioning of the Faraday cup is evenly spaced, as the apertures mostly conform to a straight line.	112
VI-1: Typical negative ion results from the VICTER negative ion subroutine. This example is for a 20 cm diameter cathode and a 50 cm diameter anode with -100 kV potential applied to the cathode and 30 mA meter current supplied to the cathode, with a 2 mTorr background gas pressure. The vertical dotted line shows the cathode potential, and the horizontal dashed lines shows the radii of the electrodes.	115
VI-2: VICTER simulation of the negative ion energy spectrum at 45 cm from center of an IEC device with a 20 cm diameter cathode, 50 cm diameter anode with a -100 kV potential applied to the cathode and 30 mA of meter current supplied to the cathode, with a 2 mTorr background pressure.	116
VI-3: VICTER simulation with the same parameters as fig. VI-2, but with each parent isolated. The y-axis is shown in log scale so the parent species curves are distinguishable. This analysis predicts that nearly all negative ions produced in the IEC device from charge exchange and disassociation reactions are produced by reactions of fast neutrals.	118
VI-4: VICTER simulation of negative ion spectra under the same conditions as in fig. VI-3. The total spectrum is shown and divided into spectra of negative ions segregated by grandparent ion species that produce a fast neutral that produces the final negative ion.	119
VI-5: Cathode voltage, current, and negative ion measurement	122

<p>radius parametric scan in an IEC device aligned with an IEC device plasma jet produced by a 50 cm diameter anode and 20 cm diameter cathode at 2 mTorr operating pressure. All measurements were taken from a 1 cm² collection area in the diagnostic.</p>	
<p>VI-6: Comparison of how Faraday cup measurements of negative ion current changes with radius in an IEC device with a 50 cm diameter anode and 20 cm diameter cathode, aligned with a plasma jet. This plot shows three different negative ion currents, with 30 kV of potential applied to the cathode. This is the same data is shown in fig. VI-5.</p>	123
<p>VI-7: Comparison of how Faraday cup measurements of negative ion current changes with radius in an IEC device with a 50 cm diameter anode and 20 cm diameter cathode, aligned with a plasma jet. This plot shows three different negative ion currents, with 45 kV of potential applied to the cathode. This is the same data is shown in fig. VI-5.</p>	124
<p>VI-8: Comparison of how Faraday cup measurements of negative ion current changes with radius in an IEC device with a 50 cm diameter anode and 20 cm diameter cathode, aligned with a plasma jet. This plot shows three different negative ion currents, with 60 kV of potential applied to the cathode. This is the same data is shown in fig. VI-5.</p>	125
<p>VI-9: Comparison of how Faraday cup measurements of negative ion current changes with radius in an IEC device with a 50 cm diameter anode and 20 cm diameter cathode, aligned with a plasma jet. This plot shows three different negative ion currents, with 15 mA of meter current supplied to the cathode. This is the same data is shown in fig. VI-5.</p>	126
<p>VI-10: Comparison of how Faraday cup measurements of negative ion current changes with radius in an IEC device with a 50 cm diameter anode and 20 cm diameter cathode, aligned with a plasma jet. This plot shows three different negative ion currents, with 30 mA</p>	127

<p>of meter current supplied to the cathode. This is the same data is shown in fig. VI-5.</p>	
<p>VI-11: Comparison of how Faraday cup measurements of negative ion current changes with radius in an IEC device with a 50 cm diameter anode and 20 cm diameter cathode, aligned with a plasma jet. This plot shows three different negative ion currents, with 45 mA of meter current supplied to the cathode. This is the same data is shown in fig. VI-5.</p>	128
<p>VI-12: Cathode voltage, current, and negative ion measurement radius parametric scan aligned with a cathode grid wire in an IEC device with a 50 cm diameter anode and 20 cm diameter cathode at 2 mTorr operating pressure. All measurements were taken from a 1 cm² collection area in the diagnostic.</p>	129
<p>VI-13: Comparison of how Faraday cup measurements of negative ion current changes with radius in an IEC device with a 50 cm diameter anode and 20 cm diameter cathode, aligned with a cathode wire. This plot shows three different negative ion currents, with 30 kV of potential applied to the cathode. This is the same data is shown in fig. VI-12.</p>	130
<p>VI-14: Comparison of how Faraday cup measurements of negative ion current changes with radius in an IEC device with a 50 cm diameter anode and 20 cm diameter cathode, aligned with a cathode wire. This plot shows three different negative ion currents, with 45 kV of potential applied to the cathode. This is the same data is shown in fig. VI-12.</p>	131
<p>VI-15: Comparison of how Faraday cup measurements of negative ion current changes with radius in an IEC device with a 50 cm diameter anode and 20 cm diameter cathode, aligned with a cathode wire. This plot shows three different negative ion currents, with 60 kV of potential applied to the cathode. This is the same data is shown in fig. VI-12.</p>	132

VI-16: Comparison of how Faraday cup measurements of negative ion current changes with radius in an IEC device with a 50 cm diameter anode and 20 cm diameter cathode, aligned with a cathode wire. This plot shows three different negative ion currents, with 15 mA of meter current supplied to the cathode. This is the same data is shown in fig. VI-12.	133
VI-17: Comparison of how Faraday cup measurements of negative ion current changes with radius in an IEC device with a 50 cm diameter anode and 20 cm diameter cathode, aligned with a cathode wire. This plot shows three different negative ion currents, with 30 mA of meter current supplied to the cathode. This is the same data is shown in fig. VI-12.	134
VI-18: Comparison of how Faraday cup measurements of negative ion current changes with radius in an IEC device with a 50 cm diameter anode and 20 cm diameter cathode, aligned with a cathode wire. This plot shows three different negative ion currents, with 45 mA of meter current supplied to the cathode. This is the same data is shown in fig. VI-12.	135
VI-19: Cathode voltage, current, and negative ion measurement radius parametric scan aligned with a plasma jet in an IEC device with a 30 cm diameter anode and 20 cm diameter cathode at 2 mTorr operating pressure. All measurements were taken from a 1 cm ² collection area in the diagnostic.	136
VI-20: Comparison of how Faraday cup measurements of negative ion current changes with radius in an IEC device with a 30 cm diameter anode and 20 cm diameter cathode, aligned with a plasma jet. This plot shows three different negative ion currents, with 30 kV of potential applied to the cathode. This is the same data is shown in fig. VI-19.	137
VI-21: Comparison of how Faraday cup measurements of negative ion current changes with radius in an IEC device with a 30 cm diameter anode and 20 cm	138

<p>diameter cathode, aligned with a plasma jet. This plot shows three different negative ion currents, with 45 kV of potential applied to the cathode. This is the same data is shown in fig. VI-19.</p>	
<p>VI-22: Comparison of how Faraday cup measurements of negative ion current changes with radius in an IEC device with a 30 cm diameter anode and 20 cm diameter cathode, aligned with a plasma jet. This plot shows three different negative ion currents, with 60 kV of potential applied to the cathode. This is the same data is shown in fig. VI-19.</p>	139
<p>VI-23: Comparison of how Faraday cup measurements of negative ion current changes with radius in an IEC device with a 50 cm diameter anode and 20 cm diameter cathode, aligned with a cathode wire. This plot shows three different negative ion currents, with 15 mA of meter current supplied to the cathode. This is the same data is shown in fig. VI-16.</p>	140
<p>VI-24: Comparison of how Faraday cup measurements of negative ion current changes with radius in an IEC device with a 50 cm diameter anode and 20 cm diameter cathode, aligned with a cathode wire. This plot shows three different negative ion currents, with 30 mA of meter current supplied to the cathode. This is the same data is shown in fig. VI-19.</p>	141
<p>VI-25: Comparison of how Faraday cup measurements of negative ion current changes with radius in an IEC device with a 50 cm diameter anode and 20 cm diameter cathode, aligned with a cathode wire. This plot shows three different negative ion currents, with 45 mA of meter current supplied to the cathode. This is the same data is shown in fig. VI-19.</p>	142
<p>VI-26: Photograph of Faraday cup and its field of view in the HOMER IEC device in the 30 cm anode - 20 cm cathode configuration. The cathode holes that give rise to the left, central, and right jets are called out.</p>	143

VI-27: Full azimuthal range field of view at 30 kV potential applied to the cathode and 30 mA meter current supplied to the cathode, at 27 and 32 cm from the center of the cathode. The HOMER IEC device was run with a 20 cm diameter cathode and 30 cm diameter anode, with a background pressure of 2 mTorr.	144
VI-28: Full azimuthal range field of view at 60 kV potential applied to the cathode and 30 mA meter current supplied to the cathode, at 27 and 32 cm from the center of the cathode. The HOMER IEC device was run with a 20 cm diameter cathode and 30 cm diameter anode, with a background pressure of 2 mTorr.	145
VI-29: Cathode current parametric scan of the negative ion jet with a 30 kV potential applied to the cathode. The HOMER IEC device was run with a 20 cm diameter cathode and 30 cm diameter anode, with a background pressure of 2 mTorr.	146
VI-30: Cathode current parametric scan of the negative ion jet with a 30 kV potential applied to the cathode. The HOMER IEC device was run with a 20 cm diameter cathode and 30 cm diameter anode, with a background pressure of 2 mTorr.	147
VI-31: Cathode voltage parametric scan of negative ion central jet profile at 27 cm from the center of the HOMER IEC device with a cathode of 20 cm diameter and anode of 30 cm diameter, 30 mA of meter current supplied to the cathode, and background pressure of 2 mTorr.	148
VI-32: Cathode voltage parametric scan of negative ion central jet profile at 32 cm from the center of the HOMER IEC device with a cathode of 20 cm diameter and anode of 30 cm diameter, 30 mA of meter current supplied to the cathode, and background pressure of 2 mTorr.	149
VI-33: Cathode voltage parametric scan of total negative ion	150

<p>central jet current measured across the azimuth of the jet at 27 cm and 32 cm from the center of the HOMER IEC device with a cathode of 20 cm diameter and anode of 30 cm diameter, 30 mA of meter current supplied to the cathode, and background pressure of 2 mTorr.</p>	
<p>VI-34: Negative ion current measurements by Faraday cup in HOMER IEC device across multiple jets, showing change as single filament columns are disconnected. The cathode diameter is 20 cm and the anode diameter is 30 cm; 30kV of potential is applied to the cathode, and 30 mA of meter current is supplied to the cathode, with a background pressure of 2 mTorr. The legend utilizes a simple diagram of the IEC device, with anode-cathode at the center, Faraday field of view at the top, and yellow filament positions showing the filaments that are active.</p>	152
<p>VI-35: Negative ion current measurements by Faraday cup in HOMER IEC device across multiple jets, showing change as single filament columns are powered. The cathode diameter is 20 cm and the anode diameter is 30 cm; 30kV of potential is applied to the cathode, and 30 mA of meter current is supplied to the cathode, with a background pressure of 2 mTorr. The legend utilizes a simple diagram of the IEC device, with anode-cathode at the center, Faraday field of view at the top, and yellow filament positions showing the filaments that are active. The black line shows all the filaments on.</p>	153
<p>VI-36: Negative ion current measurements by Faraday cup in HOMER IEC device across multiple jets, showing change as opposite pairs of filament columns are powered. The cathode diameter is 20 cm and the anode diameter is 30 cm; 30kV of potential is applied to the cathode, and 30 mA of meter current is supplied to the cathode, with a background pressure of 2 mTorr. The legend utilizes a simple diagram of the IEC device, with anode-cathode at the center, Faraday field of view at the top, and yellow filament positions showing the filaments that are active. The black line shows all the filaments on.</p>	154

VI-37: Hysteresis scan taken in the HOMER IEC device with a cathode of diameter 20 cm and anode of 30 cm, 30 kV potential on the cathode and 30 mA meter current supplied to the cathode. The measurements were taken 27 cm from the center of the cathode. The hysteresis scan shows that the data measured currents overlap within the variation of the measurement, confirming that the negative Ion current is mainly insensitive to time dependent phenomenon.	156
VII-1: VICTER simulation of the negative ion energy spectrum at 45 cm from center of an IEC device with a 20 cm cathode, 50 cm anode with a -100 kV potential on the cathode and 30 mA supplied to the cathode, with a 2 mTorr background pressure.	162
VII-2: The negative ion energy spectrum determined by the Magnetic Deflection Energy Analyzer in the HOMER IEC device with a cathode dia. of 20 cm and anode dia. of 50 cm with -100 kV potential on the cathode and 30 mA of current supplied to the cathode, with 2 mTorr background pressure [VII-3]. The purple dots are data points, and the thin red line is the sum of the five Gaussian curves.	163
VII-3: Energy spectrum of deuterium producing fusion in HOMER with -70 kV potential on the cathode and 30 mA meter current supplied to the cathode and a background pressure of 1.25 mTorr.	164
VII-4: Voltage parametric scan from the Magnetic Deflection Energy Analyzer diagnostic in the HOMER IEC device at 30 mA supplied to the cathode and 2 mTorr background gas pressure.	166
VII-5: Normalized change in negative ion current with radial position at 30 mA supplied to the cathode and 30, 45, and 60 kV supplied to the cathode, as predicted by the VICTER negative ion subroutine, and as measured by the Faraday cup in the HOMER IEC device.	169

VII-6: Normalized change in negative ion current with radial position at 45 mA supplied to the cathode and 30, 45, and 60 kV supplied to the cathode, as predicted by the VICTER negative ion subroutine, and as measured by the Faraday cup in the HOMER IEC device.	170
VII-7: Normalized change in negative ion current with radial position at 30 kV supplied to the cathode and 15, 30, and 45 mA supplied to the cathode, as predicted by the VICTER negative ion subroutine, and as measured by the Faraday cup in the HOMER IEC device.	171
VII-8: Normalized change in negative ion current with radial position at 45 kV supplied to the cathode and 15, 30, and 45 mA supplied to the cathode, as predicted by the VICTER negative ion subroutine, and as measured by the Faraday cup in the HOMER IEC device.	172
VII-9: Cathode potential parametric comparison between the VICTER negative ion subroutine and Faraday cup measurements in the HOMER IEC device at 27 cm from the center of the potential well. This comparison shows qualitatively similar behavior, but differences in slope are evident.	174
VII-10: Cathode potential parametric comparison between the VICTER negative ion subroutine and Faraday cup measurements in the HOMER IEC device at 32 cm from the center of the potential well. This comparison shows qualitatively similar behavior, but differences in slope are evident.	175
VII-11: Cathode meter current parametric comparison between the VICTER negative ion subroutine and Faraday cup measurements in the HOMER IEC device at 27 cm from the center of the potential well. This comparison shows good agreement in highly linear behavior.	176
VII-12: Pressure parametric negative ion measurements in the HOMER IEC device, on and off jet, with a 30 kV	178

<p>potential and 60 kV potential on the cathode and 30 mA supplied to the cathode. This parametric scan shows the negative ion current is essentially insensitive to chamber pressure, so long as cathode potential and supplied current are constant.</p>	
<p>VII-13: Pressure parametric negative ion prediction by the VICTER negative ion subroutine 30 kV potential on the cathode and 30 mA supplied to the cathode. This parametric scan predicts the negative ion current is highly sensitive to chamber pressure, even when cathode potential and supplied current are constant.</p>	113
<p>VII-14: Spherical coordinate system, where azimuth is labeled by the symbol θ, and elevation is labeled by the symbol ϕ.</p>	183
<p>VII-15: Faraday cup measurement of the azimuthal profile of the negative ion current in an IEC device plasma jet with a cathode of diameter 20 cm and anode of diameter 30 cm, with 30 kV potential on the cathode, 30 mA meter current and a pressure of 2 mTorr, taken 27 cm from the center of the cathode. This profile is taken at the center of the elevation range (the equator of the cathode).</p>	185
<p>VII-16: The azimuthal profile is the same as in fig. VII-15, the profile about the center of the elevation is based on normalizing the width, and interpolating the positions in the profile.</p>	186
<p>VII-17: This full extrapolation is extend from fig. VII-16, with the profile between the peak azimuthal and elevation profiles inferred from the product of the peak azimuthal and elevation profiles.</p>	187

Table of Tables

Table Caption	page
I-1: A summary of research on negative ion profiles that has been carried out in previously as well as in this work	4
VII-1:Percent increase from plasma jet negative ion profile minimum to maximum at 30 kV and 60 kV potential applied to the cathode for an IEC device with a cathode diameter of 20 cm and an anode diameter of 30 cm, operating at 2 mTorr. The profile used at 27 cm is shown in fig. VI-31 and the profile used at 32 cm is shown in fig. VI-32	182

I: Introduction

An Inertial Electrostatic Confinement (IEC) device is an apparatus that utilizes a spherically symmetric electrostatic potential well produced by biased, highly transparent, spherical grids that accelerate ions to fusion relevant energies. Ions introduced into the potential well converge on the center of the system, where the potential well is deepest; if an ion fails to undergo a reaction it recirculates in the potential well and is thereby confined until it undergoes a reaction, fusion or otherwise. A gridded IEC device may not be suitable for producing fusion power in the near term; however, an IEC device produces a steady state fusion rate and associated fusion products, such as protons and neutrons, that may be useful for a variety of near term applications. Reactions competing with the fusion reactions must be considered to understand IEC device physics.

A significant deuterium negative ion current, produced by a number of competing reactions, was discovered in a University of Wisconsin IEC device in late 2008 [I-1,2]. Measurements of the negative ion energy spectrum were made using the Magnetic Deflection Energy Analyzer, a mass spectrometer designed to measure energetic particles produced by an IEC device [I-1]. The negative ion measurements were also confirmed using a Faraday trap, and the parametric responses to cathode voltage, cathode current, and chamber pressure were measured [I-1]. Measurements at two

different cathode orientations showed that the magnitude of the negative ion current varied with the azimuthal angle, but the spatial profile of the negative ion current was unknown until this thesis work. The negative ion current was also expected to change with distance from the center of the spherical potential well, but this was unconfirmed until this thesis work. The VICTER code developed at the University of Wisconsin-Madison had no ability to model negative ion physics until this thesis work.

There are a variety of reasons why negative ions in an IEC device are of importance. Since negative ions are a significantly energetic species (some fraction of the negative ion current is the most energetic species in an IEC device), they can have important contributions to the fusion rate. Due to the high energy of the negative ions, they may produce a more significant contribution to the fusion rate than their numbers would suggest when compared to the positive ion current.

Negative ions are also a valuable way to study IEC device physics. Negative ion currents contribute to plasma jets in an IEC device, so measuring negative ion profiles yields information about these jets. In addition, plasma jets are not visible at low pressure, so measuring negative ions directly becomes a way to unambiguously confirm that plasma jets exist in an IEC device at low pressure.

The modeling of IEC devices is currently an ongoing avenue of research. Inclusion of negative ion physics in these models is valuable to

improve the accuracy of the models and, paired with negative ion measurements, produces a valuable way to benchmark IEC device models. Thus far, measurements of fusion products have been the only option available to benchmark modeling efforts. An IEC device utilizes strong potentials with steep gradients, so probes are not viable inside the potential well of an IEC device. Spectroscopic measurements are not viable at low pressure or with a great deal of light pollution from incandescent grids heated by energetic particle impact.

Negative ion sources are being used in numerous applications, from producing energetic neutral beams that heat magnetically confined plasmas for fusion energy to semiconductor processing. There exists the possibility that an electrostatic device utilizing IEC physics could represent a valuable negative ion source for some applications. Studying negative ions in an IEC device is a necessary step in exploring that potential.

To improve understanding of negative ions in IEC devices this work explores a variety of negative ion spatial and energetic profiles through measurement and modeling. A Faraday cup has been used to measure spatial profiles (radial and azimuthal) in an IEC device. An existing one dimensional IEC device simulation code has been extended to model negative ion creation, destruction, and propagation in an IEC device, producing energy and radial profiles of negative ion currents.

This work extends the initial study following the 2008 discovery of

negative ion currents in an IEC device [I-1,2]. The characteristics of negative ions studied previously and in this work are summarized in Table I- 1 below. Energy Spectrum describes the energy distribution of the negative ion current. Radial Profile and Azimuthal Profile describe spatial variation in the negative ion current, described in spherical coordinates about the center of the potential well. The Parametric Response describes the negative ion current magnitude response to variation in IEC device conditions, i.e. cathode current, cathode voltage, and background pressure.

Study Profile	Previous Work		Current Work	
	Magnetic Deflection Energy Analyzer	Faraday Trap	VICTER negative ion subroutine	Faraday Cup
Energy Spectrum	Yes	No	Yes	No
Radial Profile	No	No	Yes	Yes
Azimuthal Profile	No	Very limited	No	Yes
Parametric Response	No	Yes	Yes	Yes

Table I-1: A summary of research on negative ion profiles that has been carried out in previously [I-1,2] as well as in this work.

A variety of work has been done in the course of this research, not all of which will be discussed in this thesis. This work can be found in refereed publications [I-2, 3, 4], an M.S. thesis [I-5], posters presented at conferences [I-6 to 9], and workshop presentations [I-10 to 27].

- [I-1] D. R. Boris, "Novel Diagnostic Approaches to Characterizing the Performance of the Wisconsin Inertial Electrostatic Confinement Plasma," Ph.D. Thesis, University of Wisconsin - Madison, 2009.
- [I-2] D. R. Boris, E. C. Alderson, et al., "Deuterium anions in inertial electrostatic confinement devices," *Physical Review E*, vol. 80, no. 3, p. 036408, 2009.
- [I-3] E. C. Alderson and J. F. Santarius, "Analytic determination of the mean free path of sequential reactions," *American Journal of Physics*, vol. 80, no. 4, p. 316, Apr. 2012.
- [I-4] R. F. Radel et al., "Detection of highly enriched uranium using a pulsed D-D fusion source," *Fusion Science and Technology*, vol. 52, no. 4, pp. 1087-1091, 2007.
- [I-5] E. C. Alderson, "Spectroscopic Diagnosis of a Dense Hydrogen Plasma Source," M.S. Thesis, UW-Madison, 2008.
- [I-6] E.C. Alderson, et al., "Spectroscopic Diagnosis of Plasma in the IEC," [presented at the U.S.-Japan IEC Workshop on Small Plasma and Accelerator Neutron Sources, May 22-24, 2007, Argonne National Laboratory, Argonne, IL].
- [I-7] E.C. Alderson, et al., "Spectroscopic Diagnosis of Hydrogen Helicon Plasma Discharge," Bulletin of the American Physical Society APS-DPP Meeting, 17-21 November 2008, Dallas TX.
- [I-8] E.C. Alderson, et al., 'Negative Ion Generation in an IEC Fusion Device,' Bulletin of the American Physical Society APS-DPP Meeting, 8-12 November 2010, Chicago IL.
- [I-9] E.C. Alderson, et al., "Negative Ion Studies in an IEC Fusion Device," Bulletin of the American Physical Society APS-DPP Meeting, 14-18 November 2011, Salt Lake City UT.
- [I-10] R.P. Ashley, et al., "A Decade of IEC Research at the University of Wisconsin," [presented at the US-Japan IEC Workshop, 14-16 March 2005, Los Alamos National Laboratory, Los Alamos NM].
- [I-11] G.R. Piefer, et al., "Progress in the Development of a 3He Ion Source for IEC Fusion," [presented at the US-Japan IEC Workshop, 14-16 March 2005, Los Alamos National Laboratory, Los Alamos NM].
- [I-12] A.L. Wehmeyer, et al., "Progress in Explosives Detection Using D-D Fusion at the University of Wisconsin-Madison," [presented at the US-Japan IEC Workshop, 14-16 March 2005, Los Alamos National Laboratory, Los Alamos NM].
- [I-13] G.L. Kulcinski, et al., "Progress in IEC Research at the University of Wisconsin Since the 7th US-Japan Workshop," [presented at the 8th U.S.-Japan Workshop, 10-12 May 2006, Kansai University, Osaka, Japan].
- [I-14] R. Radel, et al., "Detection of HEU Using a Pulsed D-D Fusion Source," [presented at the 2007 ANS Student Conference, Oregon State University, Corvallis OR, 29-31 March 2007]
- [I-15] G.L. Kulcinski, et al., "Progress in IEC Research at the University of Wisconsin Since the 8th US-Japan Workshop," [presented at the U.S.-Japan IEC Workshop on Small Plasma and Accelerator Neutron Sources, May 22-24, 2007, Argonne National Laboratory, Argonne, IL].
- [I-16] S.J. Zenobia, et al., "Results of Steady State Implantation of He+ and D+ in Carbon Velvet and W-Coated Carbon Velvet," [presented at the High Average Power Laser (HAPL) meeting, October 30, 2007, Naval Research Laboratory, Washington DC.].
- [I-17] G.L. Kulcinski, et al., "Progress in Understanding the Performance of IEC Devices at the University of Wisconsin," [presented at the 11th U.S.-Japan Workshop on IEC Fusion, 12--13 October 2009, Madison WI].
- [I-18] R. Bonomo, et al., "UW-Madison IEC Laboratory Continuing Capacity Upgrades and Infrastructure Upgrades," [presented at the 11th U.S.-Japan Workshop on IEC Fusion, 12--13 October 2009, Madison WI].
- [I-19] E.C. Alderson, "A Campaign to Study Negative Ion and Fast Neutral Currents Produced by the IEC Device in a Variety of Configurations," [presented at the 11th U.S.-Japan Workshop on IEC Fusion, 12--13 October 2009, Madison WI].

- [I-20] E.C. Alderson, "Theoretical and Experimental Studies of Negative Ions in IEC Devices at UW-Madison: Current Results and Plans for Future Work," [presented at the 12th US-Japan Workshop on Inertial Electrostatic Confinement Fusion, 20-21 October 2010, Osaka, Japan].
- [I-21] G.L. Kulcinski, et al., "Overview of University of Wisconsin IEC Research," [presented at the 12th US-Japan Workshop on Inertial Electrostatic Confinement Fusion, 20-21 October 2010, Osaka, Japan].
- [I-22] R. L. Bonomo, et al., "UW IEC Group 2010: Further Infrastructure Improvements and Preparations for 300 kV Operation" [presented at the 12th US-Japan Workshop on Inertial Electrostatic Confinement Fusion, 20-21 October 2010, Osaka, Japan].
- [I-23] G.L. Kulcinski, et al., "Overview of the University of Wisconsin IEC Research Program-2011," [presented at the 13th US-Japan Workshop on Inertial Electrostatic Confinement Fusion, 7-8 December 2011, Sydney, Australia].
- [I-24] R.L. Bonomo, et al., "UW IEC Group 2011: Continuing Preparations for 300 kV Operation -- Device Switching," [presented at the 13th US-Japan Workshop on Inertial Electrostatic Confinement Fusion, 7-8 December 2011, Sydney, Australia].
- [I-25] G.A. Emmert, et al., "Update on the VICTER Code for Modeling Gridded, Spherically Symmetric IEC Devices," [presented at the 13th US-Japan Workshop on Inertial Electrostatic Confinement Fusion, 7-8 December 2011, Sydney, Australia].
- [I-26] E.C. Alderson, et al., "Negative Ion Studies in an IEC Fusion Device," [presented at the 13th US-Japan Workshop on Inertial Electrostatic Confinement Fusion, 7-8 December 2011, Sydney, Australia].
- [I-27] J.F. Santarius, et al., "Theoretical Exploration of UW IEC Device Operation at Moderate Pressures," [presented at the 13th US-Japan Workshop on Inertial Electrostatic Confinement Fusion, 7-8 December 2011, Sydney, Australia].

II: Previous Work

II.1: Inertial Electrostatic Confinement device background

II.1.1: Historical review of IEC device research

This section will examine the established understanding of the Inertial Electrostatic Confinement (IEC) device. The IEC device relies on an electrostatic potential to drive and confine positive ions to produce fusion. The principles of electrostatically driven confinement and fusion were first explored by Elmore, Tuck, and Watson in the 1950's [II-1]. Following this work, in the early 1960's P. Farnsworth patented an IEC device [II-2], which was advanced by R. Hirsch [II-3, 4, 5]. Hirsch reported a deuterium-deuterium fusion rate of 10^8 s^{-1} or $5 \times 10^7 \text{ n/s}$, and $3 \times 10^9 \text{ n/s}$ from deuterium-tritium fusion in an IEC device.

This work was continued by others in the US, though interest in the IEC device waned in the 1980's. This may have been because the IEC device, as envisioned at the time, faced the seemingly insurmountable challenge of grid melting if high power is achieved. In 1983 an IEC device variant called the Polywell™ was proposed by R.W. Bussard, which reinvigorated interest in the IEC device concept [II-6]. The Polywell™ concept uses cusped magnetic fields to trap electrons in a virtual cathode to

create a central potential well that accelerates ions to fusion relevant energies.

In the 1990's gridded IEC devices were re-examined as valuable, simple, and potentially mobile fusion *product* sources for near term applications, rather than as fusion power sources [II-7]. Thus exploration began on utilization of IEC devices as the source of high energy protons and neutrons for a variety of applications. Research on IEC devices and their variants has been sustained at a variety of educational institutions [II-8, 9, 10, 11] and government laboratories [II-12, 13, 14] in the US, as well as university research in Japan [II-15, 16, 17], Australia [II-18], South Korea [II-19] and Iran [II-20]. There is also an active 'hobbyist' community surrounding the IEC device concept for homemade fusion devices [II-21].

IEC devices have been deployed as a neutron source for assay of coal impurities [II-22, 23, 24]. There have been a number of IEC device architectures that have been proposed for this application, often revolving around cylindrical devices [II-19]. There are further non-destructive testing applications for fusion neutrons from an IEC device that have been proposed, but not yet realized[II-7].

IEC device application research is currently ongoing using fusion neutrons for detection of clandestine materials. Highly Enriched Uranium (HEU) can be detected by using fusion neutrons to cause fissions in the

HEU. This can be done by pulsing the neutron source and detecting delayed neutrons between pulses[II-25], or by detecting a difference in the neutron pulse decay due to prompt fission neutrons (a technique called Differential Die Away) [II-26]. Chemical explosives and illicit materials can be detected by gamma rays produced by neutron activation. Further, neutron imaging can be used in conjunction with x-ray imaging for a comprehensive assay of cargo [II-27].

Work on using fusion protons to produce medical isotopes is also ongoing. This research has focused on production of Positron Emission Tomography (PET) isotopes, as the compact IEC device could be deployed at many hospitals to produce the short-lived isotopes that often must be administered at the production site [II-28]. Today these isotopes are utilized mainly at research hospitals with accelerator facilities.

These applications have been successful at the proof of principle stage, but IEC device fusion rates will need to increase for successful application. Currently the University of Wisconsin – Madison holds the record IEC device fusion rate, producing 2.4×10^8 n/s steady state in D-D fusion, and 5×10^9 n/s in pulsed operation. It has also produced the IEC device record 5×10^7 p/s from D-He³ fusion reactions [II-29].

II.1.2: A description of a typical IEC device

The following description will be of the 'standard' spherical gridded

IEC device, used at the University of Wisconsin – Madison. While there are a number of variants in the literature, most take advantage of the physical attributes discussed here.

A typical IEC device consists of a spherical cathode of high geometric transparency that is held at a high negative voltage surrounded by a concentric spherical anode at ground, producing a potential well between them. The highly transparent electrodes are often in the shape of a latitude-longitude grid, but a variety of alternatives have been explored. The spherical electrode arrangement produces a spherically symmetric potential well, as diagrammed in fig. II-1.

Positive charges introduced to the potential well inside the anode experience the electrostatic force accelerating the ions toward the cathode, at energies high enough to produce fusion. The main advantage of an IEC device as a fusion source over a beam accelerated into a target is that an ion in the IEC device may experience recirculation. Further, target heating issues are reduced, longer life times are anticipated for gas targets than for solid targets, and there is no appreciable tritium inventory accumulated in the device when a deuterium tritium fuel is fused.

In recirculation, an ion is accelerated down the potential well of the IEC device, passes through the cathode, and decelerates as it climbs the potential well on the other side. It runs out of kinetic energy at the anode

and is drawn back down the potential well for another pass. This motion confines the energetic ions in the IEC device potential well so they may undergo multiple collisions before producing a fusion reaction.

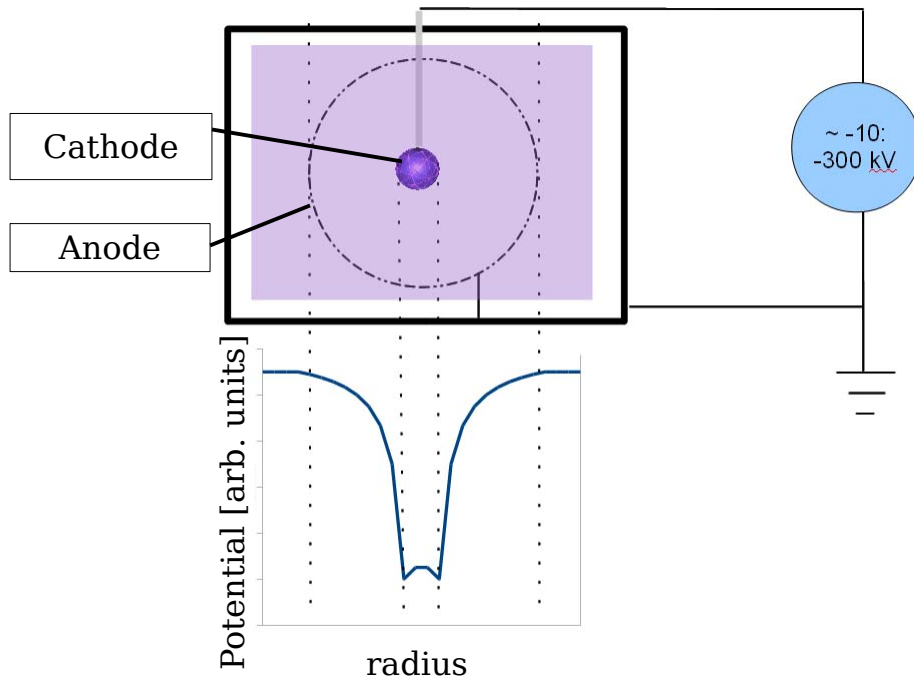


Figure II-1: Sketch of generic IEC device geometry and potential profile – not to scale.

The previous description of ion recirculation ignores the variety of interactions with background gas the ions may undergo while on their trajectories through the IEC device. These interactions are quite significant to IEC device operation; some of these reactions will be discussed, in the context of the IEC device, in some detail in section II.2.1.

Fusion in the IEC device occurs by three mechanisms. Beam-beam fusion occurs when two fast charged particles interact. This happens most often when inward moving particles converge on a central point, creating a high ion density. In the earliest conception of IEC device operations, a dense core of these reactions (called a converged core in the literature) was thought to be the dominant fusion source. However, it is now recognized that reaching converged core conditions is much more difficult than originally thought.

Beam-embedded fusion in the IEC device cathode also occurs, because the cathode grid has on the order 10 percent opacity to the circulating ions. A fraction of the inward ion current will impact the grid wires at high enough energy to undergo fusion with the fusible nuclei previously embedded in the grid wires. It has been determined that beam-embedded fusion is a dominant source of fusion in D-³He plasmas in IEC devices that create both D and ³He ions in the same region. This occurs due to Penning ionization of D by metastable excited ³He ions. Ion collisions with atoms embedded in the grid wires not only produces fusion, but they also produce secondary electrons. While secondary electron emission coefficients have not been determined with high precision because they are difficult to measure or calculate, they are expected to be on the order of 2 [II-30].

Finally, beam-gas target fusion in the IEC device occurs as

accelerated species collide with cold background neutral gas to produce fusion. Studies of fusion sources in the IEC device have shown that this is the dominant fusion source in D-D fusion for most IEC device operation regimes. However, as will be discussed, fusion is only one of many reactions fast-moving species can have with this background neutral gas.

II.2: Negative ion reactions and background

The creation of negative ions in an IEC device is achieved by two types of processes:

- charge exchange reactions between atoms or molecules and ions
- electron attachment reactions by cold electrons and neutral molecules

This thesis will exclusively consider hydrogenic negative ions, as all experimentation and simulation were done with the deuterium isotope. Many of these reactions are well documented [II-31].

II.2.1: Charge exchange reactions

A fast deuterium ion traveling through a neutral gas target may produce a number of reactions. Because an IEC device accelerates positively charged particles radially inward toward the cathode region, reactions are produced with the background gas in the IEC device, their cross sections varying as the ion energy changes with radius. These

reactions produce a variety of impacts on IEC device operations. All the charge exchange and dissociation reactions impact the creation of negative ion current. These reactions either produce negative ions, daughter products that can produce negative ions, compete with the reactions that create negative ions, or attenuate negative ions.

In the reactions discussed in this section, the cross sections are a function of the relative velocity and exhibit no other isotope effect; a hydrogen reaction cross section and deuterium reaction cross section are the same at equivalent relative velocity [II-32]. In the projectile-stationary target case, a deuterium reaction cross section is the same as the hydrogen reaction cross section at twice the deuterium projectile energy, as the deuterium is twice as massive.

Before discussing the negative ion creation reactions we will discuss the creation of fast neutrals, as fast neutrals are a dominant daughter product produced by positive ions and a potential parent of negative ions, with a stronger cross section than any positive ion double electron capture reaction (that produces a negative ion directly from a positive ion). Generally, the creation of fast neutrals occurs by charge exchange, dissociation, or a combination of the two. The energetics and cross sections of these reactions are controlled by the quantum mechanics governing the allowed states. The most prevalent reactions are the ones with the least difference in energy between the parent and daughter states. The atomic

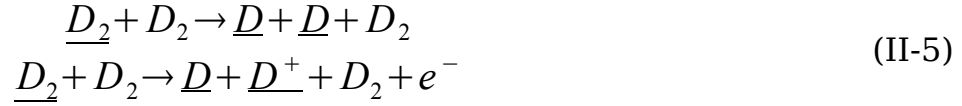
fast neutral can be born from a variety of projectiles impacting on a (predominantly) diatomic cold neutral gas present as a background gas in the IEC device. The relevant (but not all) ion reactions producing the atomic fast neutral are spelled out below, with the fast species underlined.



In cases where parent species may produce a daughter projectile by multiple branches the sum of these cross sections can be collapsed into a single generation cross section. It should be noted that multiple reactions with D_3^+ occur, and while the individual reactions are still under study, the total generation cross section of fast neutral D production by collision of D_3^+ with D_2 is well characterized [II-30].

Molecular fast neutrals also must be considered. They are created by the reaction in eqn II-4, and can undergo the reactions in eqn II-5:





The total fast neutral creation cross sections are shown in fig. II-2.

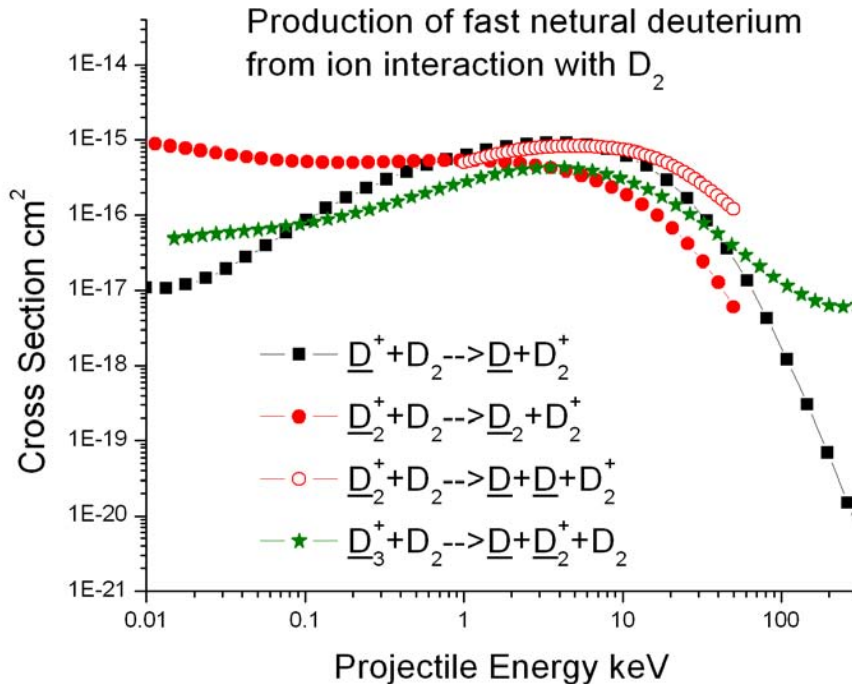


Figure II-2: A graph of the total cross sections that give rise to hydrogenic fast neutrals [II-31].

The cross sections that produce atomic fast neutrals follow a similar profile, peaking in the 10's of keV range, between 10^{-16} to 10^{-15} cm^2 . Assuming a roughly room temperature 2 mTorr background gas, the shortest mean free path for the atomic fast neutral creation is on the order of 15 cm.

The direct creation of negative ions occurs by the following reactions [II-31, 33]:



As illustrated for hydrogen collisions in fig. II-3, the cross section responsible for negative ion formation from a fast neutral is higher than the cross section for double charge exchange (i.e. equations II-8, 9, and 10), but not drastically so. Further analysis is carried out in chapter III.4 to determine if double electron capture is as significant as sequential reactions in an IEC device.

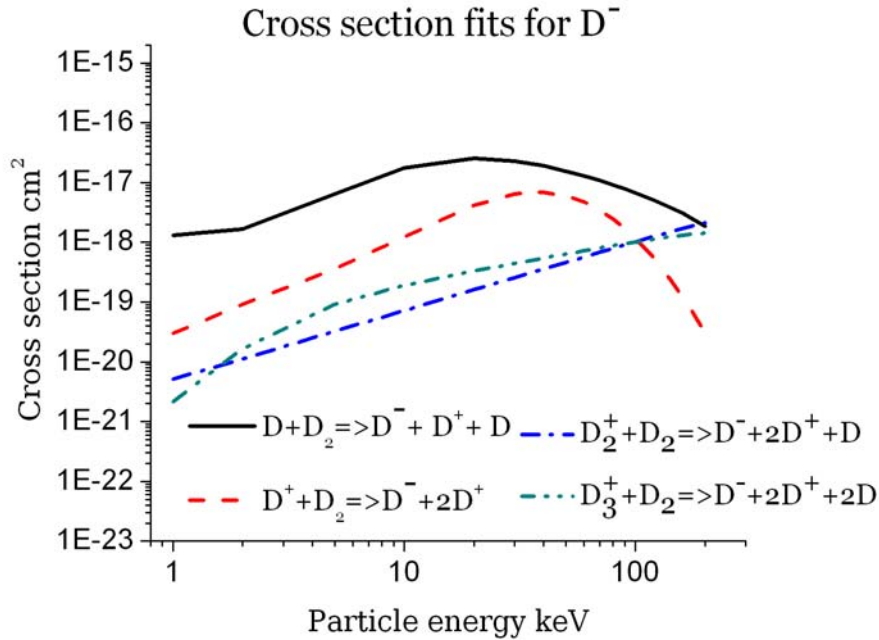


Figure II-3: Graph of deuterium negative ion creation charge exchange cross sections on a background of D_2 target gas [II-31,33].

II.2.2: Electron attachment creation of negative ions

For deuterium negative ion formation by electron impact the dominant reaction is dissociative attachment, as follows:



A molecular hydrogen negative ion does form, but it is unstable and decays into an atomic negative ion and neutral; in most cases the molecular negative ion has a half-life of femtoseconds [II-34].

The cross section for this reaction is strongly dependent on the state of the hydrogen molecule at the time of electron impact, as seen from the

cross sections illustrated in fig. II-4. This is because a molecule in the ground state is more likely to produce an autodetachment reaction where no negative ion is formed, while an excited negative ion is more likely to produce the desired dissociative electron attachment reaction.

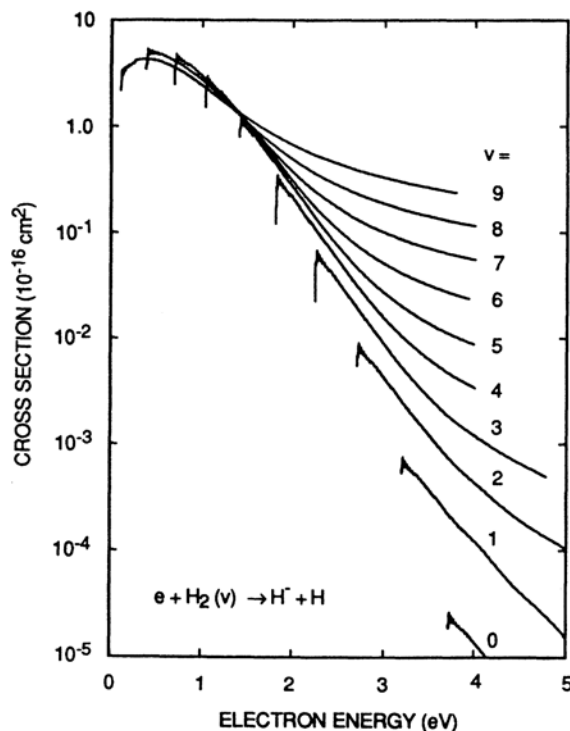


Figure II-4: The cross sections for the dissociative electron attachment reaction for a variety of target hydrogen molecule vibrational states. "v" is the vibrational quantum number of the H₂ molecule [II-32].

Vibrational excitation of the diatomic hydrogen molecule is known to happen by a handful of reactions, only two of which are significant to this work: electron collision and wall collision. The optimum temperature for electron excitation of hydrogen molecules is 40 eV, but for reasons described in Chapter II.2.3 a 40 eV electron population is detrimental to a

negative ion population. This excitation also occurs by interaction with a solid surface; molecular ion neutralization from wall collision and atom recombination on the wall are two such paths. However, the principle loss process for excited molecular ion states is wall relaxation.

In the earlier discussion regarding electron dissociative attachment it was stated that the negative molecular ion is unstable, and typically lasts on the order of femtoseconds; however, even in early experiments on hydrogen negative ion formation, some experiments produced results that could be attributed to the presence of molecular negative ions [II-35]. These results could not be verified, and the extremely short measured and calculated lifetime of molecular negative ions made these results inexplicable, as the molecular negative ions were not expected to have a long enough lifetime to be extracted and detected in their molecular state.

In 2006, the existence of long lived negative ions was verified unambiguously in experiment [II-36]. In the following year work with theoretical quantum mechanics models revealed that a metastable molecular negative ion can be produced from highly rotationally excited states, with rotational quantum numbers that exceeding 25 for hydrogen and 35 for deuterium. These states can be thought of as a negative ion and a neutral orbiting a common center. The D_2^- molecule has been observed exhibiting a mean lifetime of 1.8 ms in extremely high rotational states [II-37].

Early IEC device negative ion research suggested the metastable D₂⁻ molecule could be a surprisingly high constituent of the IEC device negative ion population [II-38], though this result is somewhat ambiguous, and it will be discussed in Chapter VII.1.

II.2.3: Surface reaction creation of negative ions

While surface reactions are not expected to be a significant source of negative ions in an IEC device, it is worth discussing this physics for completeness, as these processes are the most commonly utilized in commercial negative ion sources. When a low work function substrate is deposited on a high work function adsorbate, in proper coverage, the base adsorbate is induced to give up an electron to the substrate. When this occurs across the surface the resulting image charges produce a dipole layer in the substrate that has a decreased work function.

The most effective combination of adsorbate and substrate used today is tungsten and cesium. The minimum work function of this combination is 1.5-1.6 eV with a 0.5 to 0.7 coverage of the substrate. Improved surfaces are in development, using molecules for the adsorbate and substrate that depress the work function farther, though these are not in wide usage in application. These sources require cesium to be redeposited periodically. There are applications where the redeposition of cesium is not possible or desirable, which motivates the development of alternative negative ion

sources [II-39].

The relevant materials in the IEC device, a tungsten cathode, a stainless steel anode, and aluminum chamber, do not have a particularly low work function. There is no significant cesium in the IEC device, and any that might inadvertently be deposited on the IEC device tungsten cathode would quickly be boiled off by cathode heating.

It is possible for a fast neutral hydrogenic atom to impact a surface and recoil as a negative ion. This has been examined as a source of energetic negative ions in the source region, near the wall of the IEC device, but in the case of deuterium impacting aluminum, between 1% and 0.1% of the incident current has been observed to recoil as a negative ion in experiment [II-40]. Recoil as a fast neutral is more likely and requires further investigation to determine if this plays an important role in IEC devices.

II.2.3: Neutralization of negative ions

Multiple processes are significant in negative ion destruction, as the electron affinities that bind the extra electron to the negative ion are low, no more than a few eV and typically a fraction of an eV. The impact of these processes on the negative ion population cannot be neglected. Adding complexity to the question of analyzing the negative ion population is the fact that many of the mechanisms responsible for producing negative ions

also destroy negative ions.

When a negative ion passes through a thick gas target, the fraction of neutralization is given by eqn. (II-12) [II-32]

$$f = 2N \sum_i \int_0^l \sigma_i \cdot P dl \quad (\text{II-12})$$

where

- N is the constant $3.54 \times 10^{16} \text{ Torr}^{-1} \text{ cm}^{-3}$
- $\Sigma_i \sigma_i$ is the sum of all the destruction cross sections produced by collisions with species present in the region
- P is the pressure in the region in Torr
- l is the path length in cm

The two dominant negative ion electron stripping reactions in an IEC device are:



The primary reaction that destroys the deuterium negative ion is reaction (II-13), due to the cross section as shown in fig. II-5.

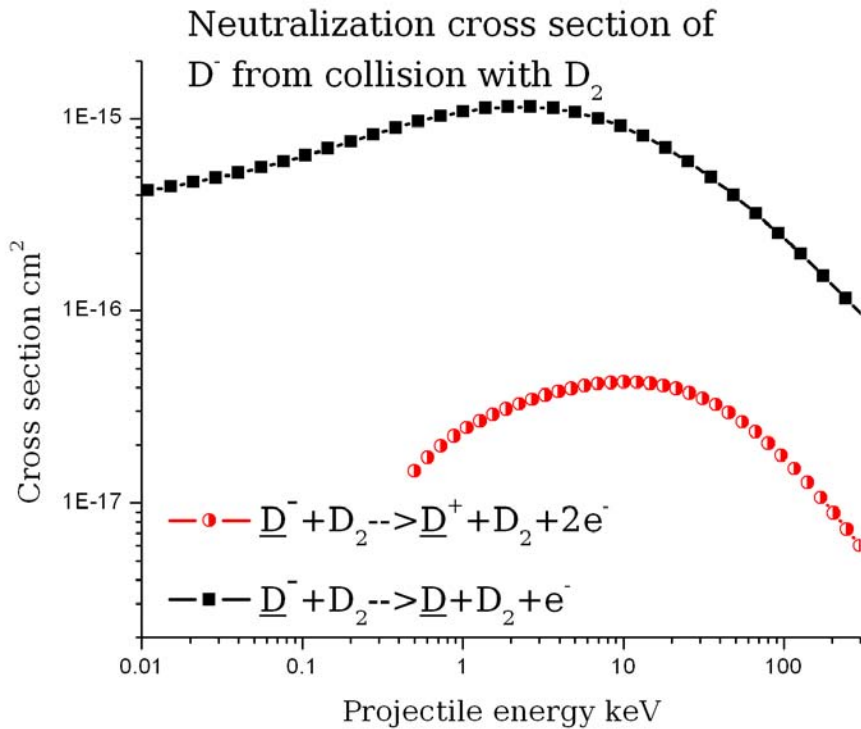


Figure II-5: Cross sections for destruction of deuterium negative ions through collision with molecular background gas [II-31].

A photon of sufficient energy will neutralize a negative ion via the $h\nu + D^- \rightarrow D + e^-$ reaction [II-41]. The cross section for this reaction is dependent on photon energy, as illustrated in fig. II-6.

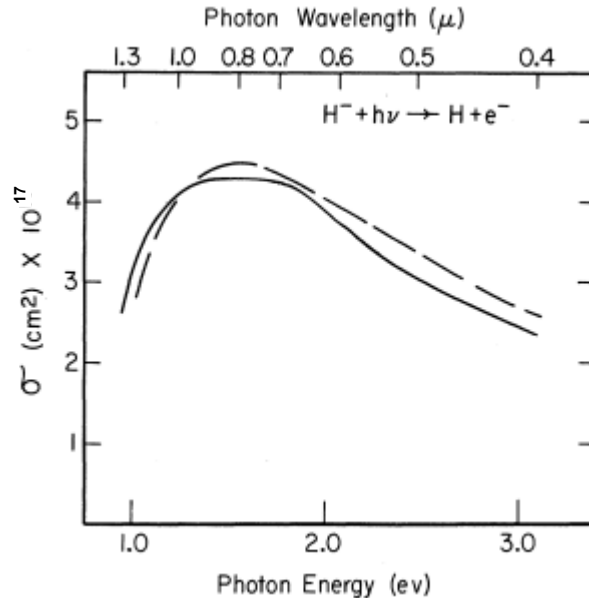


Figure II-6: Cross section of hydrogen negative ion photodetachment as a function of photon energy [II-41].

The fraction of negative ions neutralized by photodetachment is given by the equation:

$$f = 1 - e^{-\sigma F \tau} \quad (\text{II-15})$$

where:

- F is the photon flux
- σ is the cross section for the process,
- τ is the time the negative ions are in the photon flux

While electron impact on neutrals can form negative ions, as described in section II.2.2, electron impact on negative ions can neutralize the negative ion via the $e^- + D^- \rightarrow 2e^- + D$ reaction. The cross section for this reaction is illustrated in fig. II-7 below, along with the negative ion

creation from dissociative electron attachment cross section, for comparison of the competing processes.

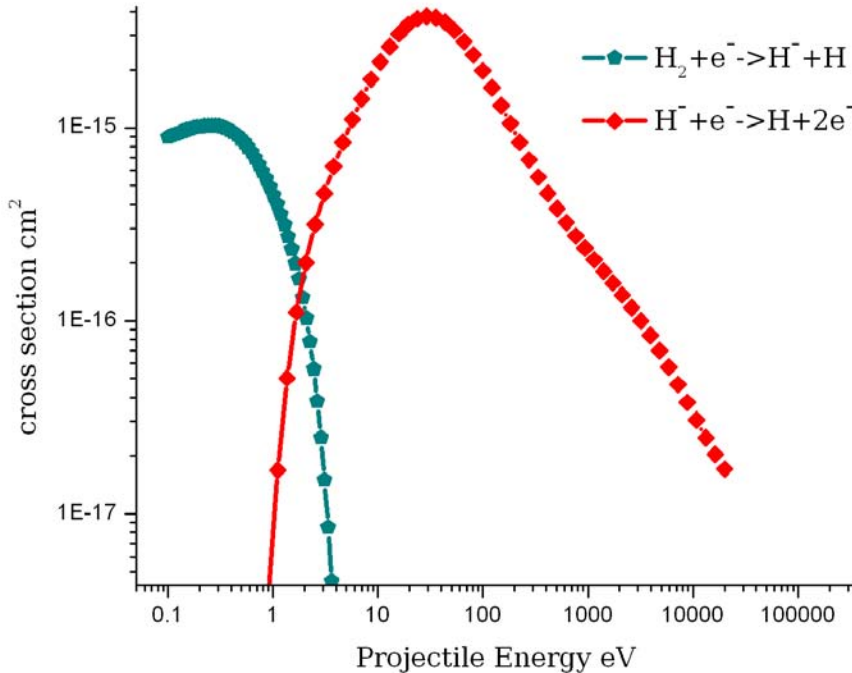


Figure II-7: Electron attachment cross section for hydrogen (teal pentagons) and detachment cross section for negative ion collision with an electron (red diamonds). Assuming the electron is the projectile, the cross section should be unchanged for deuterium [II-31].

Due to the competing processes, to create an environment conducive to negative ion formation by electron attachment the electron population must be at a low temperature, less than 2-3 eV. However, the cross section above assumes an excited H_2 population, which in most systems is formed by energetic electron impact, with the excitation cross section peaking around 40 eV where the detachment from electron impact cross section is high. This presents a difficulty in hydrogenic negative ion sources utilizing

electron attachment that must be carefully overcome.

There are significant neutralization cross sections between hydrogen negative ions and atomic neutral hydrogen as well as hydrogen ions. However the density of these species are significantly reduced from the molecular neutral hydrogen, and are considered negligible in this work.

Neutralization can also occur by impacting a surface. It is assumed in this work any collision of a negative ion with a surface results in a destruction of the negative ion.

II.3: Negative ion measurements in an IEC device

II.3.1: Observations of electrons and fast neutral particles in an IEC device.

Besides negative ions, electrons and fast neutrals can escape the anode-cathode potential well, forming a “jet” of particles. Electrons that escape the region inside the anode are either secondary electrons born from impacts on the IEC device cathode, thermionic electrons, or born by liberation from ion or electron collisions with neutral particles. These particles excite background gas, which produces line radiation that makes the path of the plasma jets emanating radially from the spaces in between the IEC device cathode grid wires visible at sufficiently high pressure. These structures are called plasma jets in much of the IEC device research

community, drawing on terminology used in a variety of plasma studies, including hollow cathode discharges. An example of an IEC discharge with visible jets is given in fig. II-8 [II-42].

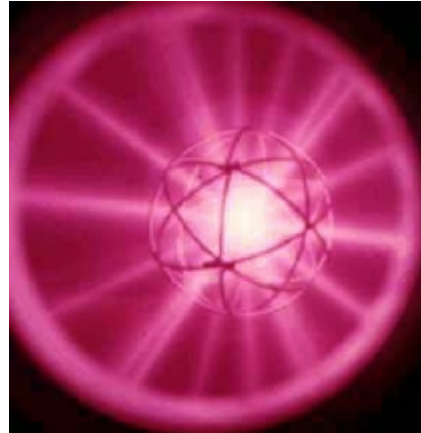


Figure II-8: Photograph of a gridded IEC device at the University of Illinois at Urbana-Champaign, where they typically operate in a regime that clearly exhibits visible plasma jets [II-42]. While this work at UW-Madison is carried out using grids with a latitude-longitude mesh, the same sort of structures are exhibited at high pressure and small radius cathodes.

For these jets to be visible in an IEC device the cathode must be sufficiently small to produce a focused jet and the background pressure must be high enough that sufficient gas is excited to produce visible emission. These jets visibly weaken with distance from the cathode, but appear to extend all the way to the anode. A brief study of the electrons from a hollow cathode that produces a plasma jet analogous to an IEC device jet shows the electrons in the jet are within 85% of the cathode potential energy when between 2 and 10 keV is applied to the cathode, even at 10's of mTorr neutral pressure of hydrogen [IV-43].

The existence of a fusion relevant outward flux of energetic deuterium

(in deuterium fueled runs) in an IEC device has been recognized since the mid 90's [II-44], when fusion diagnostic experiments detected a significant source of fusion reaction products originating in the IEC device anode region, away from the cathode. Here the potential profile is expected to be flatter and no particles are accelerated to fusion relevant energies. IEC device theory matured to take into account fast ions charge exchanging with background gas to produce a fast neutral and cold ion flux. Please refer to Chapter II.2.1 for a full discussion of these reactions. Research by the UW-IEC group indicates that, in a deuterium plasma, fusion outside the cathode, even where a low potential gradient exists, is a significant source of fusion in the IEC device [II-45, 46], and work at Kyoto University confirms this conclusion [II-47].

It has been hypothesized that the source of these energetic neutrals is the plasma jets visually observed in high pressure IEC device operation. Scientists at the University of Illinois Urbana-Champaign (UIUC) have proposed these jets are space-charge neutralized ion beams that they have named microchannels [II-22,48]. They hypothesize that these microchannels increase the effective grid transparency from ~90% to 98-99%, based on jet formation predicted by the SIMION ion optics code [II- 42]. The power of an individual jet has been inferred from calorimetric measurement of a plate placed in the jet path. Researcher at the Universit of Sydney have concluded that the sum of the power in the jets to be

greater than 50% of the power supplied to the IEC device [II-50].

Scientists at the UIUC have also demonstrated that a jet intensity is strongly dependent on the cathode grid hole size [II-43]. If a single grid hole is expanded in size (by removal of a cross wire) the jet at that site becomes the dominant jet, and all other jets are weakened to the point of being invisible, as shown in fig. II-9.

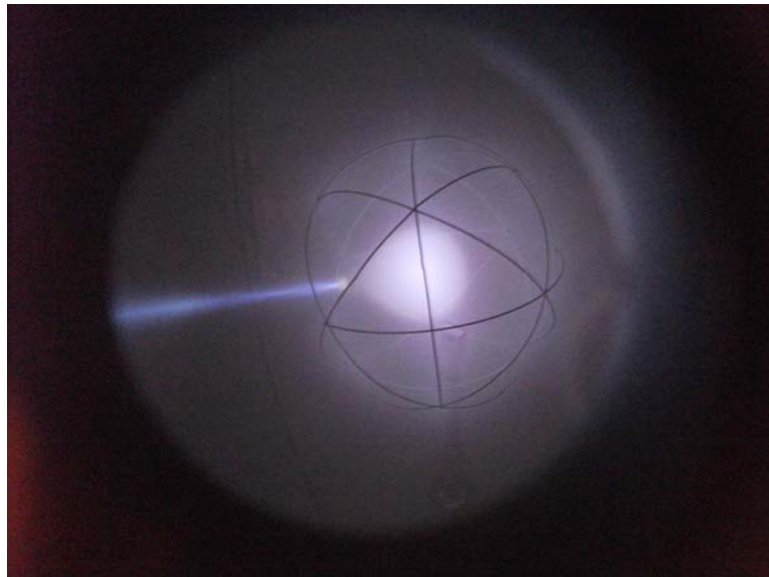


Figure II-9: IEC device cathode with a single enlarged grid hole. The jet emanating from the large hole is dominant, to the point that the other jets are not visible [II-48].

A thorough study of electrostatic plasma jets at the University of Sydney in Australia via Doppler-shift emission spectroscopy in hollow cathodes that produce jets analogous to IEC device jets, has yielded a very detailed characterization of jet energies [II-49]. In these hollow cathode plasma jets, Doppler-shift spectroscopy shows that between the anode and cathode there is a stronger emission detected from outward traveling flux

than inward traveling flux, as illustrated in fig. IV-10. This emission from outward flux is observed to increase in magnitude and energy with radius, i.e. farther from the cathode [II-50].

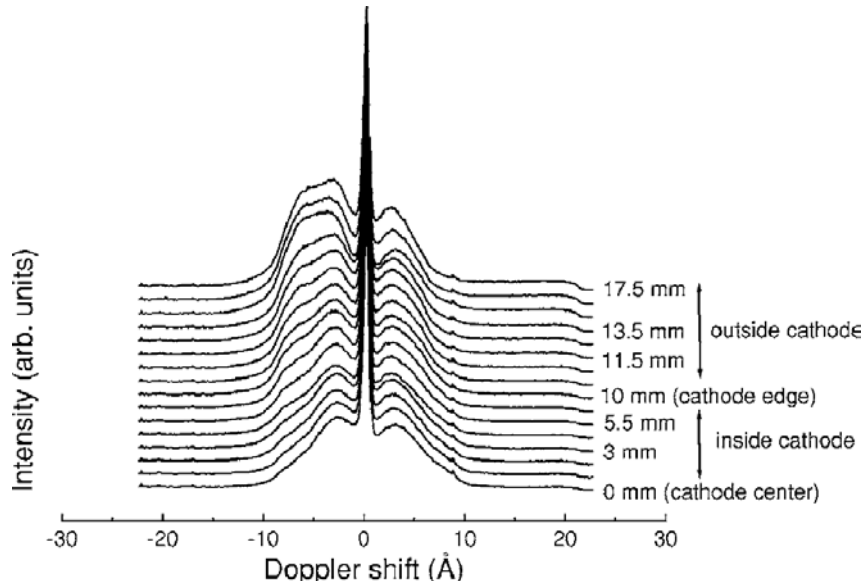


Figure II-10: Spectroscopic Doppler shift results of fast neutral particles in the IEC device, offset by distance from the cathode center [II-50].

The utility of the University of Sydney diagnostic approach is limited by the pressure at which emission spectroscopy is measurable; at pressures less than 5 mTorr the signal becomes too weak to be detected by most visible light spectrometers. Questions have remained regarding the applicability of these conclusions to low pressure operation, and how excited state lifetimes may impact these results. Further, the hollow cathode used at the University of Sydney has two open channels, and is otherwise opaque, which produces two strong jets, but the ratios of charged particles in these jets could be significantly different from typical IEC

device discharges. However, the outward acceleration from the cathode result is surprising for positive ions in any regime of the IEC device operation, and the results have remained the subject of debate. Modeling work by Phelps suggests wall interactions may be responsible for this evolution in spectrum [II-51].

Until 2008, these plasma jets were hypothesized to consist entirely of positive ions, electrons, and fast neutrals; negative ions were not mentioned in the IEC device literature. Despite extensive study on the IEC device produced neutral flux, the neutral current has never been isolated and measured directly [IV-50, 48].

II.3.2: Measurements of negative ions in an IEC device

Negative ions were first measured at the UW-IEC laboratory at the University of Wisconsin – Madison in November 2008, made using the Magnetic Deflection Energy Analyzer (MDEA), diagrammed in fig. II-12 [II-38, 52]. This apparatus uses a magnetic field produced by a GMW Associates electromagnet, model 5403, to bend charged particles out of the field of view of the IEC device chamber in a custom made vacuum elbow, into a charged particle detector.

In the simplistic model the deflection angle is given by the equation:

$$\sin(\theta_d) = \frac{\left(\frac{q}{m} \vec{v} \times \vec{B} \right) t}{v} \quad (\text{II-16})$$

where

- v is the particle velocity
- t is the time in the magnetic field
- θ_d is the angle of deflection
- q is the particle charge
- m is the particle mass
- B is the magnetic field

Equation II-16 can be recast, such that:

$$\sin(\theta_d) = \frac{qlB}{mv} \quad (\text{II-17})$$

where l is the particle path length through the magnetic field.

It was determined from the initial measurements that a small iris was needed to prevent the solid state particle detector from being overwhelmed by negative ion current. Even with two 100 μm diameter irises, the detectors were receiving too much negative ion current to resolve the energy of the particles without pileup. Thus it was decided to use the deflection angle to determine the energy of the current collected by the detector. While the deflection angle calculation of equation II-17 is

straightforward, in practice a physical magnet will not produce a perfectly uniform magnetic field, and it will exhibit “fringe” magnetic fields. As such, a more detailed simulation was carried out using SIMION [II-53] to determine how charged particles would behave in the MDEA to determine the negative ions energy from the applied magnetic field, as shown in fig. II- 11. This method is limited in that it cannot calibrate the energy of the measured particles, but rather, the particle charge to momentum ratio; this can be recast to energy if the species of the current is assumed.

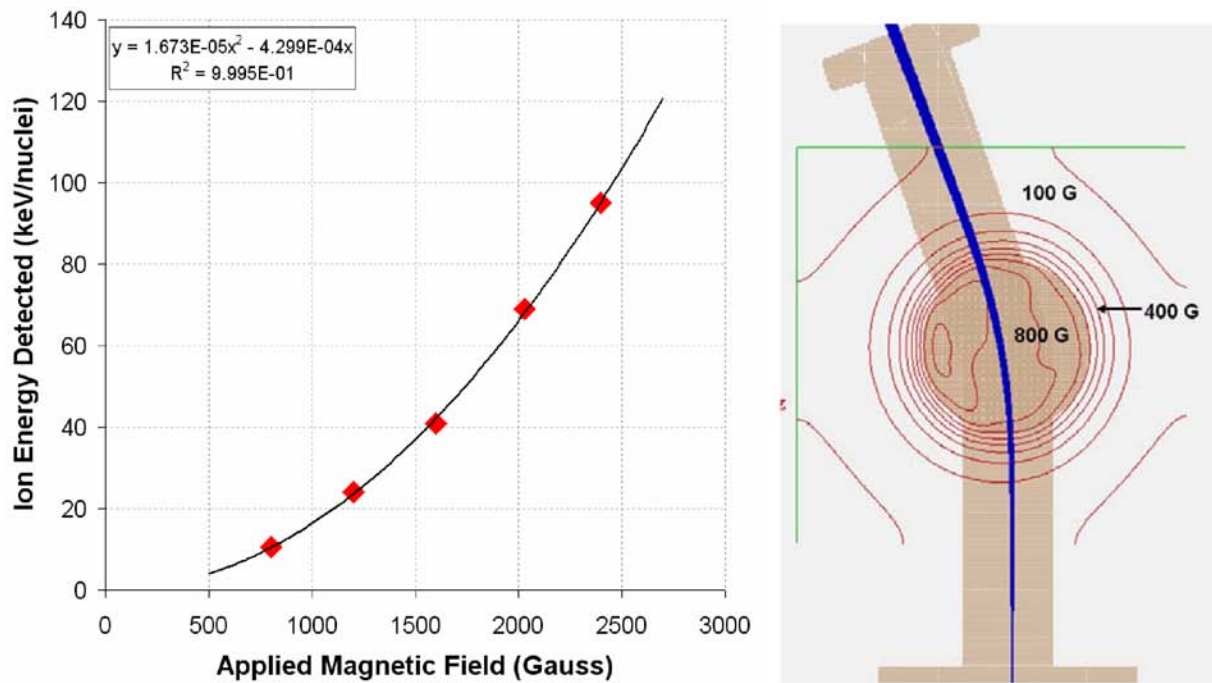


Figure II-11: Method for calibrating the energy of the measured negative ion current with the applied magnetic field in the Magnetic Deflection Energy Analyzer. (Left) curve showing simulation results and equation fitting the curve. (Right) the result of a SIMION simulation used to develop the calibration curve [II-38].

Simulation and refinement led to the final design of the MDEA, shown

in fig. II-12. The results of this simulation show that the calibration is very sensitive to the simulated magnetic field. The inclusion of the fringing fields in the simulation produces a substantial difference in the calibration curve compared to the simulation without the fringing fields, which exposes this calibration method's sensitivity to correctly modeled magnetic field.

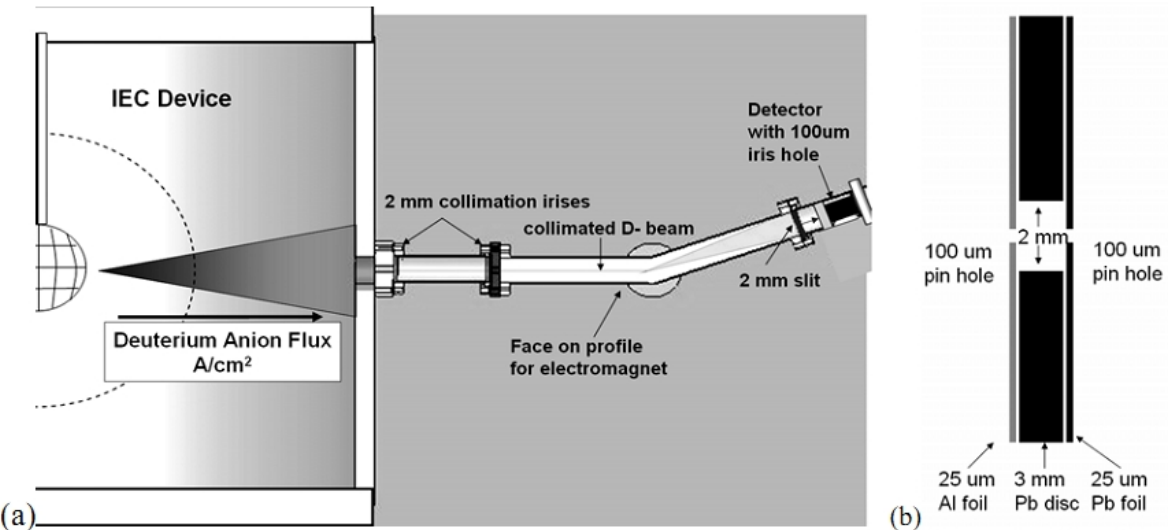


Figure II-12: (a) Illustration of the Magnetic Deflection Energy Analyzer, aligned so the negative ion jet is first reduced by a pair of 2 mm collimation irises, then bent by the field of an electromagnet, (b) then collimated by a pair of 100 μm diameter holes and then detected by a solid state charged particle detector [II-38, 52].

The MDEA results from a voltage parametric scan are shown in fig. II- 13. This parametric scan shows that the negative ion energy spectrum has structure, and that structure evolves with cathode current. To deconvolve the structure of the negative ion current energy spectrum, the 100 kV cathode potential case was examined and decomposed into a sum of

Gaussian peaks. The best fit was achieved as a sum of 5 Gaussians, as shown in fig. II-14.

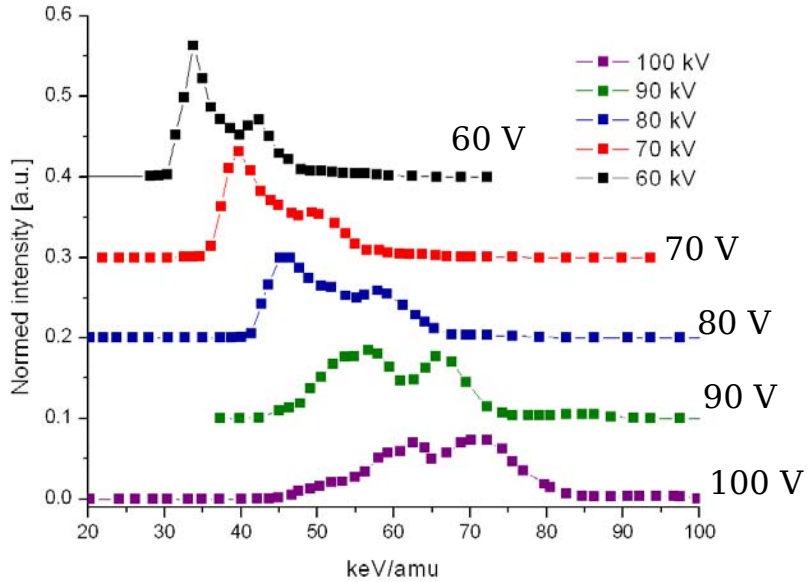


Figure II-13: The results of the Magnetic Deflection Energy Analyzer measurement of the negative ion energy spectrum at a variety of cathode voltages, in a system with a 20 cm cathode and 50 cm anode, at 2 mTorr background pressure, and 30 mA cathode current. Each cathode voltage is offset by 0.1 a.u. [II-38, 52].

Following measurement of negative ions by the MDEA, confirmation of this result was pursued using a simplified Faraday cup detector. The Faraday trap, diagrammed in fig. II-15, consists of a 0.7 cm^2 collection plate and secondary electron suppression grid with a primary electron and cold ion deflection magnet. The secondary electron suppression grid was -50 V with respect to the collection plate, and kept secondary electrons from escaping the collection plate. The energetic primary electrons from the IEC device cathode ($\sim 100 \text{ keV}$) were unable to reach the collection plate due to

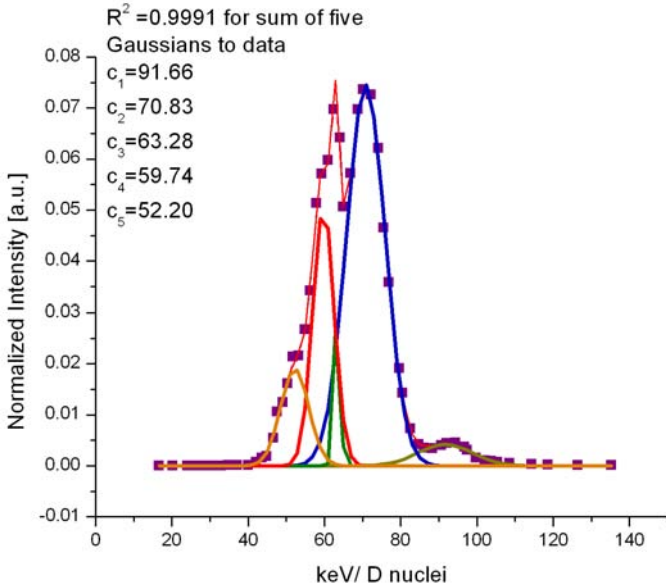


Figure II-14: Negative ion energy spectrum measured by the Magnetic Deflection Energy Analyzer, and decomposed into 5 Gaussians, the centroid of each listed as c_1-c_5 [II-38, 52].

the 100 Gauss field from the deflection magnet, but the massive ions were only slightly perturbed by the weak magnetic field. However, this magnet could be removed to measure the energetic (>50 eV) electrons as well as negative ions. The Faraday trap was recessed in a vacuum port, away from the plasma source region, which was necessary as the collection electrode was otherwise not shielded from charged particles from the environment. While this design choice limited secondary electrons born from glancing strikes on insulating surfaces, it meant the detector was fixed in the vacuum port where it was installed.

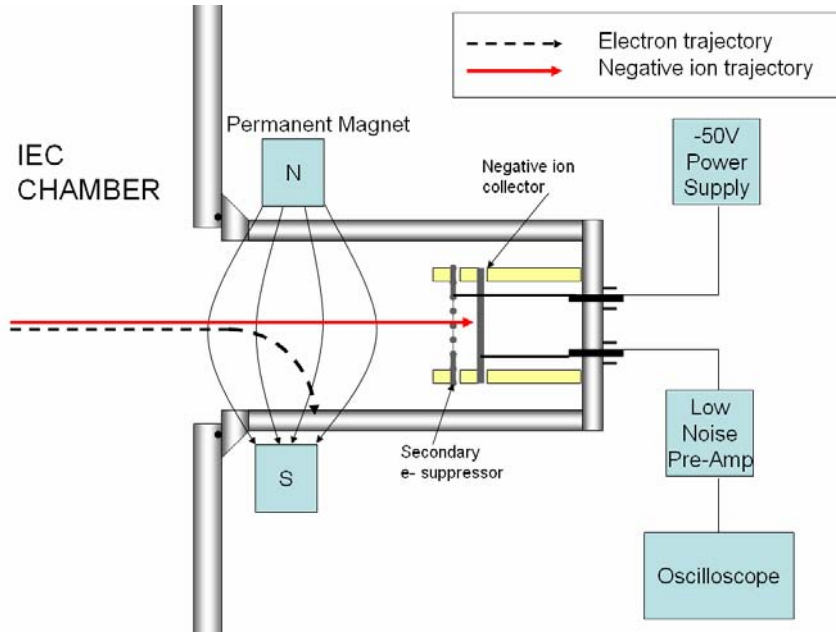


Figure II-15: Diagram of Faraday Trap used to measure negative ion current produced by HOMER IEC device [IV-38, 52].

This collector has a variety of merits. Firstly, the Faraday Trap is a compact diagnostic, making construction and installation easy. It also provides an unambiguous current density measurement, uncomplicated by the effective collection area of the multiple irises and fraction of the spectrum bent into the final iris by the bending magnet. Also, with the primary electron bending magnet removed, this Faraday trap can measure primary electron current as well.

The Faraday Trap showed a factor of 5 reduction in collected current when aligned with a cathode wire. In a jet from an IEC device with a cathode diameter of 20 cm and an anode diameter of 50 cm with a potential of 100 kV on the cathode and 30 mA meter current supplied to the cathode the negative ion peak current at the HOMER device wall (~ 45 from the

center of the cathode) was measured to be roughly 6 μA . Extrapolated to all 250 channels, a total negative ion current for the entire device of ~ 1.5 mA is projected in a gridded IEC device running at these conditions.

The Faraday trap also demonstrated a negative ion current peak and rollover with pressure (peak at ~ 2 mTorr) and cathode voltage (peak at 90 kV), while negative ion current seemed to plateau with cathode current above 30-40 mA. Whether these results indicate behavior in negative ion production, more complicated particle dynamics, or a combination thereof remains to be explored. These results are somewhat speculative, due to the limited observations. The jets must be better characterized before device currents, current production, and jet dynamics can be extrapolated.

As electrons are very mobile, they are rapidly diverted by perturbations in the potential arising from discrete grid wires. The negative (and positive) ions will also respond to these potentials as well as the electron populations, albeit more slowly. How charged particle flux interacts with perturbations in the IEC device potential remains an open question. Understanding this flux requires mapping in the radial, latitudinal, and longitudinal space at multiple pressures, cathode potentials, and cathode currents to examine if these potentials produce a microchannel focusing effect.

- [II-1] W. C. Elmore, J. L. Tuck, and K. M. Watson, "On the inertial-electrostatic confinement of a plasma," *Physics of Fluids*, vol. 2, no. 3, pp. 239-246, May 1959.
- [II-2] P. T. Farnsworth, "electric discharge device for producing interactions between nuclei," U.S. Patent 32584021966.
- [II-3] R.L. Hirsch, "Inertial-electrostatic confinement of ionized fusion gases," *Journal of Applied Physics*, vol. 38, no. 11, pp. 4522-&, 1967.
- [II-4] R. L. Hirsch and G. A. Meeks, "Highly efficient inexpensive medium current ion source," *Review of Scientific Instruments*, vol. 38, no. 5, pp. 621, 1967.
- [II-5] R.L. Hirsch, "Experimental studies of a deep negative electrostatic potential well in spherical geometry," *Physics of Fluids*, vol. 11, no. 11, p. 2486, 1968.
- [II-6] R. W. Bussard, "Method and apparatus for controlling charged particles," Patent no. 4826646, May 1989.
- [II-7] G. L. Kulcinski, "Near term commercial opportunities from long range fusion research," *Fusion Science and Technology*, vol. 30, no. 3, p. 411-420, Dec. 1996.
- [II-8] G.H. Miley, et al, "Inertial-Electrostatic Confinement: An Approach to Burning Advanced Fuels," *Fusion Technology* 19 (1991): 840.
- [II-9] J.F. Santarius et al., "Overview of University of Wisconsin inertial-electrostatic confinement fusion research," *Fusion Science and Technology*, vol. 47, no. 4, pp. 1238-1244, 2005.
- [II-10] C. Dietrich, "Improving particle confinement in inertial electrostatic fusion for spacecraft power and propulsion," Ph.D. Thesis Massachusetts Institute of Technology, 2007.
- [II-11] R.M. Meyer, S.K. Loyalka, and M.A. Prelas, "Potential well structures in spherical inertial electrostatic confinement devices," IEEE Transactions on Plasma Science 33.4 Part 2 p.1377-1394, 2005.
- [II-12] R. A. Anderl, J. K. Hartwell, J. H. Nadler, J. M. DeMora, R. A. Stubbers, and G. H. Miley, "Development of an IEC neutron source for NDE," in *Proceedings of 16th International Symposium on Fusion Engineering*, vol. 2, pp. 1482-1485, 1995.
- [II-13] C. Dobson, "Research Status of IEC Experiments at NASA Marshal", *Presented at 5th US-Japan IEC workshop*, 2002.
- [II-14] J. Park, R. A. Nebel, S. Stange, and S. K. Murali, "Periodically oscillating plasma sphere," *Physics of Plasmas*, vol. 12, no. 5, p. 056315, May 2005.
- [II-15] M. Ohnishi, K. . Sato, Y. Yamamoto, and K. Yoshikawa, "Correlation between potential well structure and neutron production in inertial electrostatic confinement fusion," *Nuclear Fusion*, vol. 37, no. 5, pp. 611-619, May 1997.
- [II-16] H. Matsuura, T. Takaki, K. Funakoshi, Y. Nakao, and K. Kudo, "Ion distribution function and radial profile of neutron production rate in

- spherical inertial electrostatic confinement plasmas," *Nuclear Fusion*, vol. 40, no. 12, pp. 1951-1954, Dec. 2000.
- [II-17] K. Yamauchi and K. Ogasawara, "Neutron production characteristics and emission properties of spherically convergent beam fusion," *Fusion Technology*, vol. 39, pp. 1182-1187, 2001.
- [II-18] J. Khachan and S. Collis, "Measurements of ion energy distributions by Doppler shift spectroscopy in an inertial-electrostatic confinement device," *Physics of Plasmas*, vol. 8, no. 4, p. 1299, Apr. 2001.
- [II-19] K. J. Chung, H. D. Jung, J. Y. Park, and Y. S. Hwang, "Development of a Cylindrical Neutron Generator using RF-driven Plasma," in *2006 International Symposium on Discharges and Electrical Insulation in Vacuum*, 2006, pp. 674-677.
- [II-20] V. Damideh et al., "Experimental Study of the Iranian Inertial Electrostatic Confinement Fusion Device as a Continuous Neutron Generator," *Journal of Fusion Energy*, vol. 31, no. 2, pp. 109-111, Jun. 2011.
- [II-21] Fusior website: <www.Fusior.net> Jul. 23, 2012
- [II-22] G. H. Miley et al., "Inertial-Electrostatic Confinement Neutron/Proton Source," in *AIP Conference Proceedings*, vol. 299, no. 1, pp. 675-689, 1994.
- [II-23] S. DelMedico, "Fusion-related projects at Rockford Technology Associates, Inc.," *Journal of Fusion Energy*, vol. 14, no. 2, pp. 191-200, 1995.
- [II-24] J. Sved, "Commercial IEC portable neutron source," *Transactions of the American Nuclear Society*, vol. 77, pp. 504-505 Dec. 1997.
- [II-25] R.F. Radel, Detection of highly enriched uranium and tungsten surface damage studies using a pulsed inertial electrostatic confinement fusion device, Ph.D. Thesis, Ph.D. Thesis University of Wisconsin-Madison, 2007.
- [II-26] J. H. Sorebo, G. L. Kulcinski, R. F. Radel, and J. F. Santarius, "Special Nuclear Materials Detection Using IEC Fusion Pulsed Neutron Source," *Fusion Science and Technology*, vol. 56, no. 1, pp. 540-544, 2009.
- [II-27] L. Wu, G. H. Miley, H. Momota, and P. J. Shrestha, "An integrated broad area coverage fusion neutron/X-ray interrogation unit," *Fusion Science and Technology*, vol. 52, no. 4, pp. 1096-1100, 2007.
- [II-28] J. W. Weidner et al., "Production of ^{13}N Via Inertial Electrostatic Confinement Fusion," *Fusion Science and Technology*, vol. 44, no. 2, pp. 539-543, Sep. 2003.
- [II-29] G. L. Kulcinski et al., "Near term applications of Inertial Electrostatic Confinement Fusion," *Fusion Science and Technology*, vol. 56, no. July, pp. 493-500, 2009.
- [II-30] C.F. Barnett, "Atomic Data for Fusion Vol. 1" *Controlled Fusion Atomic Data Center*, 1990.
- [II-31] IAEA Cross Section Data Base ALADDIN

- <<http://www-amdis.iaea.org/ALADDIN/>> accessed Jan. 1, 2009.
- [II-32] H. Zhang, *Ion sources* Springer-Verlag, 1999.
- [II-33] Private communication with A. Phelps 12/10/2010
- [II-34] O. Asvany, I. Savić, S. Schlemmer, and D. Gerlich, "Variable temperature ion trap studies of $\text{CH}_4^+ + \text{H}_2$, HD and D_2 : negative temperature dependence and significant isotope effect," *Chemical Physics*, vol. 298, no. 1–3, pp. 97-105, Mar. 2004.
- [II-35] R. Golser et al., "Experimental and Theoretical Evidence for Long-Lived Molecular Hydrogen Anions H_2^- and D_2^- ," *Physical Review Letters*, vol. 94, no. 22, pp. 203003, Jun. 2005.
- [II-36] O. Heber et al., "Lifetimes of the negative molecular hydrogen ions: H_2^- , D_2^- , and HD^- ," *Physical Review A*, vol. 73, no. 6, pp. 060501 Jun. 2006.
- [II-37] M. Čížek, J. Horáček, and W. Domcke, "Long-lived anionic states of H_2 , HD, D_2 , and T_2 ," *Physical Review A*, vol. 75, no. 1, pp. 012507, Jan. 2007.
- [II-38] D.R. Boris, "Novel Diagnostic Approaches to Characterizing the Performance of the Wisconsin Inertial Electrostatic Confinement Plasma," Ph.D. Thesis University of Wisconsin - Madison, 2009.
- [II-39] M. Bacal, "Physics aspects of negative ion sources," *Nuclear Fusion*, vol. 46, pp. s250 2006.
- [II-40] G. M. McCracken, "Back-scattering of keV hydrogen ions in solids," *Journal of Physics B: Atomic and*, vol. 661, pp. 661-668 1969.
- [II-41] S. J. Smith and D. S. Burch, "Photodetachment Cross Section of the Negative Hydrogen Ion," *Physical Review Letters*, vol. 2, no. 4, pp. 165-166, Feb. 1959.
- [II-42] G. H. Miley, J. M. DeMora, R. A. Stubbers, T. A. Hochberg, J. H. Nadler, and R. A. Anderl, "Discharge characteristics of the spherical inertial electrostatic confinement (IEC) device," *IEEE Transactions on Plasma Science*, vol. 25, no. 4, pp. 733-739, 1997.
- [II-43] J. Kipritidis, M. Fitzgerald, and J. Khachan, "Spectroscopic determination of electron energies in a discharge of atomic H produced by a monoenergetic electron beam," *Journal of Physics D: Applied Physics*, vol. 40, no. 17, pp. 5170-5176, Sep. 2007.
- [II-44] T.A. Thorson, "Ion Flow and Fusion Reactivity Characterization of a Spherically Convergent Ion Focus," Ph.D. Thesis University of Wisconsin-Madison, 1996.
- [II-45] B.B. Cipiti, "The Fusion of Advanced Fuels to Produce Medical Isotopes Using Inertial Electrostatic Confinement", Ph.D. Thesis University of Wisconsin-Madison, 2004.
- [II-46] R.P. Ashley, et al, "Steady-State $\text{D}-\text{He}^3$ Proton Production in an IEC Fusion Device," *Fusion Technology* vol. 39 pp.546-51, 2001
- [II-47] K. Masuda, K. Yoshikawa, T. Ohishi, and S. Ogawa, "Spatial Distribution of DD/ $\text{D}-\text{He}^3$ Advanced Fuels Fusion Reactions in an Inertial

- Electrostatic Confinement Device," *Proc. 21st IAEA Fusion Energy Conference*, 2006.
- [II-48] Courtesy of the HII PER Space Propulsion Laboratory, Department of Nuclear, Plasma, and Radiological Engineering, University of Illinois at Urbana-Champaign.
- [II-49] J. Khachan and S. Collis, "Measurements of ion energy distributions by Doppler shift spectroscopy in an inertial-electrostatic confinement device," *Physics of Plasmas*, vol. 8, no. 4, p. 1299, Apr. 2001.
- [II-50] O. Shrier, J. Khachan, S. Bosi, M. Fitzgerald, and N. Evans, "Diverging ion motion in an inertial electrostatic confinement discharge," *Physics of Plasmas*, vol. 13, no. 1, p. 012703, Jan. 2006.
- [II-51] A.V. Phelps, "Collisional kinetics of non-uniform electric field, low-pressure, direct-current discharges in H₂," *Plasma Sources Science and Technology*, vol. 20, no. 4, p. 043001, Aug. 2011.
- [II-52] D. Boris et al., "Deuterium anions in inertial electrostatic confinement devices," *Physical Review E*, vol. 80, no. 3, p. 036408, 2009.
- [II-53] D. Manura, et al., SIMION 8.0 Scientific Instrument Services, INC. 2006.

III: Analytic determination of the mean free path of sequential reactions

As discussed in section II.2.1 analysis is needed to determine if the production of negative ions via the sequence of reactions of postive ion to fast neutral to negative ion is as important as the double electron capture reaction from positive ion to negative ion in a single reaction. The easiest way to compare the significance of reactions is to compare their mean free paths (also known as interaction lengths) both to each other and to the length the reaction of interest can occur in (in this case the diameter of the chamber in which the reaction is occurring). The result of this analysis will impact the reactions modeled in chapter IV.

III.1: Mean free path for a single reaction

As an energetic ion travels through a target population it may undergo a collision resulting in a reaction. The distance the energetic ion travels without collision resulting in a reaction is named the mean free path. The derivation of the mean free path for a single reaction is given in many sources [III-1,2,3,4]. The outcome of this derivation for constant density and cross section is given by:

$$\lambda = \frac{1}{n\sigma} \quad (\text{III-1})$$

where

- λ is the mean free path of a reaction
- n is the target density
- σ is the cross section for the reaction of interest

Comparing the mean free path of competing reactions or comparing mean free path to the device size for single reactions is straightforward. The analog of the mean free path for a sequence of reactions is complicated because the probability of preceding reactions and the probability of attenuation of earlier generations impacts the probability of the ultimate reaction occurring at a given range. For this reason the treatment of the interaction length of a sequence of reactions requires a careful assessment. This chapter summarizes an approach that the author developed and published during his thesis research [III-1].

In order to exploit the conventional terminology, we call the total average distance in which a sequence of reactions occurs the “sequential mean free path.” In the single reaction case the average free distance without a collision is equivalent to the average distance for a collision to occur. For a sequential reaction, the path is not truly “free” because one or more collisions occur in that distance. Nevertheless, this terminology seems like a reasonable extension of the conventional terminology.

Considering negative ion creation in an IEC device, two comparisons need to be made. If the sequential mean free path for the chain of reactions

from ion to fast neutral to negative ion is much longer than the mean free path for creation of negative ions from double electron capture, then the former can be neglected in the modeling or vice versa. If the sequential mean free path for the chain of reactions from ion to fast neutral to negative ion is much longer than the device size, the chain of reactions can be neglected in the modeling. Beyond the negative ion creation context, the sequential reaction or sequential collision is important to microscopic fluid behavior, gas kinetics, radiation transport, and gaseous electronics [III-5].

III.2: Two step sequential mean free path

To generalize the sequential mean free path analysis we will consider generations of currents denoted by a sequence of numbers. The first generation is current I_1 . In the simplest case, which will be used to illustrate the theory, this current impinges on a target medium of infinite dimension and uniform density n . Each component of current I_1 has some probability of colliding with the target medium and undergoing a reaction to produce the second generation of interest in the sequence of reactions, I_2 . The cross section for this reaction is denoted by σ_{12} . The current I_1 can undergo other attenuating reactions that compete with the creation of I_2 as well, which will be summed into the current $I_{1'}$. Like current I_1 , the second generation has some probability of colliding with the target medium and undergoing a reaction to produce the third generation of interest in the sequence of reactions, I_3 . The cross section for this reaction is denoted by

σ_{23} . The current I_2 can undergo other attenuating reactions that compete with the creation of I_3 as well, which will be summed into the current I_2' .

To determine the sequential mean free path we also must consider the attenuating reactions that compete with the reactions of interest to the sequential reaction, characterized by branching ratios. The reactions attenuating current I_1 will be described by the destruction cross section σ_{1d} , and the reactions attenuating current I_2 will be described by the destruction cross section σ_{2d} . The destruction cross section of a current is defined as the sum of all the cross sections that attenuate that current:

$$\sigma_{ad} = \sigma_{ab} + \sigma_{ai} + \sigma_{aj} + \sigma_{ak} + \dots \quad (\text{III-2})$$

where $\{I_b, I_i, I_j, \dots\}$ represents every daughter current from I_a , each with the respective creation cross section $\{\sigma_{ab}, \sigma_{ai}, \sigma_{aj}, \dots\}$. The destruction cross section gives rise to the total attenuation mean free path:

$$\lambda_{ad} = \frac{1}{n \sigma_{ad}} \quad (\text{III-3})$$

This series of reactions is expressed diagrammatically in fig. [III-1].

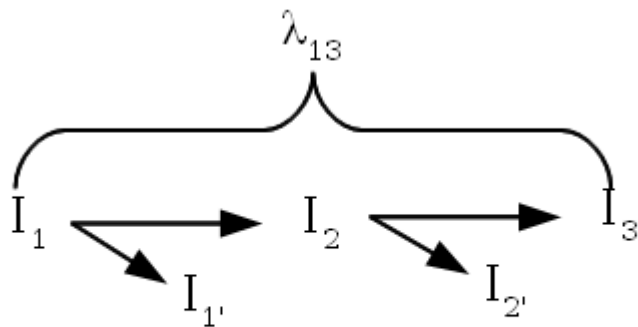


Figure III-1: Diagram of current evolution where I_1 produces I_2 , which produces I_3 . The currents produced by I_1 other than I_2 are summed into the current $I_{1'}$ and the currents produced by I_2 other than I_3 are summed into the current $I_{2'}$. The mean free path for a particle of species 1 to produce a particle of species 3 is denoted by λ_{13} .

In some cases the elements of $I_{1'}$ can undergo a reaction that contributes to the populations in the series of reactions of interest. For the purposes of this analysis, that would be considered a separate series of reactions, and be assessed as such.

Determining the mean free path of sequential reactions requires knowing the probability that the ultimate product is created in an interval dx about x . This probability is determined by the creation cross sections of the reactions leading to the ultimate product, as well as the attenuating reactions competing with the reactions of interest. The sequential mean free path should not be considered without the competing reactions because these reactions attenuate the parent species in the sequence of reactions, reducing the probability that subsequent species are produced.

Our notational convention is to let λ_{ab} represent the mean free path for a particle of species a to produce a particle of species b via a collision or series of collisions. In the general case where each species is numbered, a and b are integers specifying the species such that $b > a$. If a and b are consecutive integers, e.g., λ_{12} , λ_{23} , etc., the reaction is the result of a single collision and λ_{ab} is the conventional mean free path as discussed in the previous section. Thus, $\lambda_{ab}=1/n\sigma_{ab}$ for consecutive species.

To determine the mean free path λ_{13} we first need to find the probability that a particle of species 2 survives to a distance x , and multiply this by the probability that a particle of species 2 becomes a particle of species 3 within an infinitesimal distance dx . The probability that a particle of current I_2 survives to a distance x is given by:

$$P_2(x) = \frac{I_2(x)}{I_0} \quad (\text{III-4})$$

where:

- $I_2(x)$ is the intensity of current I_2 at x
- I_0 is the intensity of the initial current I_1 at $x=0$

This probability times the probability that I_2 becomes I_3 within the interval dx yields the probability of creation of I_3 at x within dx .

The two step sequential reactions are governed by the equations:

$$\frac{dI_1}{dx} = -n \sigma_{1d} I_1 = \frac{-I_1}{\lambda_{1d}} \quad (\text{III-5})$$

$$\frac{dI_2}{dx} = n \sigma_{12} I_1 - n \sigma_{2d} I_2 = \frac{I_1}{\lambda_{12}} - \frac{I_2}{\lambda_{2d}} \quad (\text{III-6})$$

$$\frac{dI_3}{dx} = n \sigma_{23} I_2 = \frac{I_2}{\lambda_{23}} \quad (\text{III-7})$$

Assuming n and the cross sections are constant it is possible to solve for these currents analytically. The solution for $I_2(x)$ is necessary to determine $P_2(x)$:

$$I_2(x) = \frac{I_0}{\lambda_{12}} \left[\frac{\lambda_{1d} \lambda_{2d}}{\lambda_{1d} - \lambda_{2d}} e^{-x/\lambda_{1d}} + \frac{\lambda_{1d} \lambda_{2d}}{\lambda_{2d} - \lambda_{1d}} e^{-x/\lambda_{2d}} \right] \quad (\text{III-8})$$

This is used to determine $P_2(x)$, from eqn. III-4. We can determine the probability of creating I_3 from I_2 within the interval dx from eqn. III-7:

$$Q_{23}(dx) = \frac{dI_3(x)}{I_2(x)} = n \sigma_{23} dx = \frac{dx}{\lambda_{23}} \quad (\text{III-9})$$

Thus, the probability of creating I_3 from I_2 within the interval dx , about x is given by $P_{13}(x, dx) = P_2(x) Q_{23}(dx)$, so the average distance for current I_1 to undergo a series of collisions to produce current I_3 is given by:

$$\lambda_{13} = \int_0^\infty x P_{13}(x, dx) = \int_0^\infty \frac{x I_2(x)}{I_0 \lambda_{23}} dx \quad (\text{III-10})$$

$$\lambda_{13} = \frac{\lambda_{1d} \lambda_{2d}}{\lambda_{12} \lambda_{23}} (\lambda_{1d} + \lambda_{2d}) \quad (\text{III-11})$$

In the case that there are no competing reactions with the creation of I_2 and I_3 equation (III-11) takes on the intuitively satisfying result:

$$\lambda_{13} = \lambda_{12} + \lambda_{23} \quad (\text{III-12})$$

II.3: Sequential mean free path of arbitrarily high number of collisions

Having solved the equivalent mean free path of a sequence of two reactions, we may extend the analysis for a higher number of reactions. Solving the sequential mean free path for a sequence of three reactions can be solved similarly to the two step sequential mean free path, resulting in:

$$\lambda_{14} = \frac{\lambda_{1d} \lambda_{2d} \lambda_{3d}}{\lambda_{12} \lambda_{23} \lambda_{34}} (\lambda_{1d} + \lambda_{2d} + \lambda_{3d}) \quad (\text{III-13})$$

Comparing eqns. III-11 and III-13 a pattern emerges that a general solution to the sequential mean free path may satisfy. Utilizing the argument that gave rise to eqn. III-10, we see the sequential mean free path for the m^{th} generation in a series of generations is given by:

$$\lambda_{1m} = \int_0^\infty \frac{x I_{m-1}(x)}{I_0 \lambda_{(m-1)m}} dx \quad (\text{III-14})$$

This can be solved in the general case, using the properties of the Laplace transform [III-1]. To begin with we recognize the Laplace transform of current $I_{m-1}(x)$ is

$$\widehat{I_{m-1}(s)} = \int_0^\infty I_{m-1}(x) e^{-sx} dx \quad (\text{III-15})$$

This can be differentiated to achieve the result:

$$\frac{d \widehat{I}_{m-1}}{ds} = - \int_0^\infty x I_{m-1}(x) e^{-sx} dx \quad (\text{III-16})$$

When this is evaluated at $s=0$ this becomes:

$$\frac{d \widehat{I}_{m-1}}{ds} \Big|_{s=0} = - \int_0^\infty x I_{m-1}(x) dx \quad (\text{III-17})$$

which can be substituted into eqn. III-14, to produce the expression:

$$\lambda_{1m} = \frac{1}{I_0 \lambda_{(m-1)m}} \frac{d \widehat{I}_{m-1}}{ds} \Big|_{s=0} \quad (\text{III-18})$$

Equation III-18 must be solved using the generalized governing system of equations:

$$\frac{dI_1}{dx} = \frac{-I_1}{\lambda_{1d}} \quad (\text{III-19})$$

$$\frac{dI_2}{dx} = \frac{I_1}{\lambda_{12}} - \frac{I_2}{\lambda_{2d}} \quad (\text{III-20})$$

...

$$\frac{dI_{m-1}}{dx} = \frac{I_{m-2}}{\lambda_{(m-2)(m-1)}} - \frac{I_{(m-1)}}{\lambda_{(m-1)d}} \quad (\text{III-21})$$

$$\frac{dI_m}{dx} = \frac{-I_{m-1}}{\lambda_{(m-1)m}} \quad (\text{III-22})$$

and applying the Laplace transform to each generation of governing equation, with the assumptions that $I_1(x=0)=I_0$ and all other initial currents

are 0. Performing the Laplace transform on eqn. III-19 produces:

$$\begin{aligned} \mathcal{L}\left[\frac{dI_1}{dx} = \frac{-I_1}{\lambda_{1d}}\right] \\ s \widehat{I_1(s)} - I_0 = \frac{-\widehat{I_1(s)}}{\lambda_{1d}} \\ \widehat{I_1(s)} = \frac{I_0}{(s + 1/\lambda_{1d})} \end{aligned} \quad (\text{III-23})$$

This result is substituted into the Laplace transform of eqn. III-20:

$$\begin{aligned} \mathcal{L}\left[\frac{dI_2}{dx} = \frac{I_1}{\lambda_{12}} - \frac{I_2}{\lambda_{2d}}\right] \\ s \widehat{I_2(s)} - I_2(0) = \frac{\widehat{I_1(s)}}{\lambda_{12}} - \frac{\widehat{I_2(s)}}{\lambda_{2d}} \\ \widehat{I_2(s)} = \frac{\frac{1}{\lambda_{12}} I_0}{(s + 1/\lambda_{1d})(s + 1/\lambda_{2d})} \end{aligned} \quad (\text{III-24})$$

where $I_2(x=0)=0$ as assumed above. Similarly, the the Laplace transform is carried out on each succeeding governing equation, drawing upon the previous transform, to produce the Laplace transform of eqn. III-22:

$$\begin{aligned} \widehat{I_{(m-1)}(s)} &= \frac{1}{\lambda_{12}} \frac{1}{\lambda_{23}} \cdots \frac{1}{\lambda_{(m-2)(m-1)}} I_0 \\ \widehat{I_{(m-1)}(s)} &= \left(\prod_{i=1}^{m-2} \frac{1}{\lambda_{i(i+1)}} \right) \left(\prod_{j=1}^{m-1} \frac{1}{(s + 1/\lambda_{jd})} \right) \end{aligned} \quad (\text{III-25})$$

Taking the derivative of eqn. III-25 and evaluating at $s=0$ yields:

$$\frac{d \widehat{I_{(m-1)}}}{ds} \Big|_{s=0} = -I_0 \left(\prod_{i=1}^{m-2} \frac{1}{\lambda_{i(i+1)}} \right) \left(\prod_{j=1}^{m-1} \lambda_{jd} \right) \left(\sum_{k=1}^{m-1} \lambda_{kd} \right) \quad (\text{III-26})$$

which is substituted into eqn. III-18 to produce the general solution to the sequential mean free path of m reactions:

$$\lambda_{1m} = \left(\prod_{i=1}^{m-1} \frac{\lambda_{id}}{\lambda_{i(i+1)}} \right) \left(\sum_{j=1}^{m-1} \lambda_{jd} \right) \quad (\text{III-27})$$

II.4: Sequential mean free path applied to currents in an IEC device

This analysis was motivated by the desire to compare sequential reactions producing negative ions with direct reactions producing negative ions. Of specific interest is determining if sequential reactions produce a significant fraction of the negative ions produced within an IEC device. To determine the individual reaction mean free paths and destruction mean free paths a target population and density must be assumed. This can be inferred from gas species, pressure during operation and gas temperature. The HOMER IEC device typically operates at 2 mTorr of deuterium, which is roughly 6.6×10^{13} D₂ molecules per cm³ at room temperature. This value will be used for the following analyses.

While the sequential mean free path argument as presented here assumes mono-energetic particles (note that ion energy in the IEC device changes with radius), the argument gives a sense of scale of the average path length for the sequence of reactions to occur, as the relevant cross

sections have only modest variation across the energy range of interest. Assessing this sequential mean free path length over the range of ion energies, as shown in fig. II-2, gives a more complete picture.

This result shows that over the full range of ion energies in the IEC device the length of the sequential mean free path is less than the HOMER device size of 91 cm.

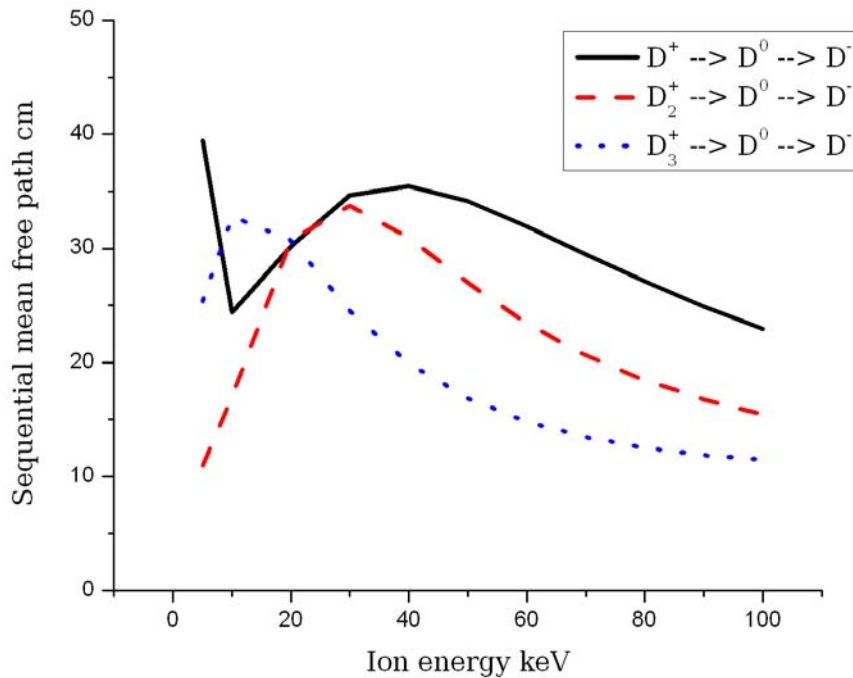


Figure III-2: Sequential mean free path for three species of ions to become atomic fast neutrals and those fast neutrals to become negative ions in a 2 mTorr D_2 gas at room temperature, where the ions start with a kinetic energy between 5 to 100 keV, and undergo no acceleration.

We know that negative ions can be born from fast neutrals and from positive ions. This analysis shows the sequence of reactions from positive

ion to fast neutral to negative ions can occur in the length scale of the HOMER IEC device, and is of the same significance as the single reaction from positive ion to negative ion. For modeling purposes, the negative ion creation reactions from fast neutrals should be included in any modeling of negative ion physics in an IEC device. For comparison, the single reaction from ion species to negative ion species is considered in fig. III-3.

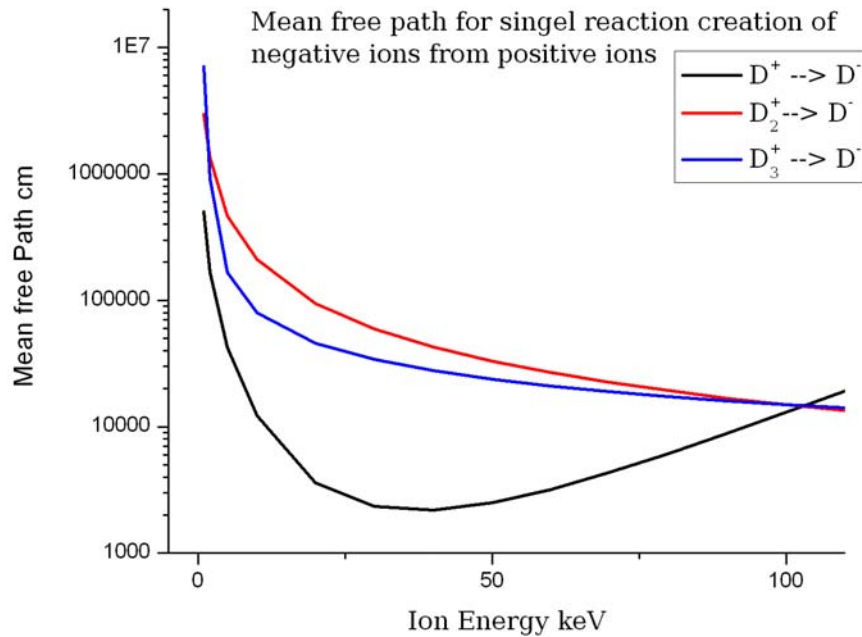


Figure III-3: A plot of the mean free path for the reaction of an ion to collide with neutral D_2 and become a negative ion directly, through a double electron capture in a 2 mTorr D_2 gas at room temperature. The y-axis is in logarithmic scale. This plot shows the mean free path for double electron capture is much longer than the sequential mean free path for an ion to produce a fast neutral, which becomes a negative ion. An ion would have to undergo hundreds of passes before it reached a path length that is a significant fraction of the mean free path for creation of negative ions.

This analysis suggests that the sequential reaction production of negative

ions is the dominant path for negative ion production.

Another question of interest is the ionization of fast neutrals in an IEC device. Energetic particles in an IEC device can undergo a variety of reactions, and neutralization of charged particles is characterized by some of the strongest cross sections. This makes the daughter fast neutral current a dominant constituent of the energetic particles in the IEC device and it is important to know if fast neutral particles are likely to undergo reaction. For our modeling in particular, it is important to know if destruction of the fast neutral population is significant enough to require modeling. The sequential mean free path argument can be used to assess this by comparing the positive ion to fast neutral to positive ion sequence mean free path to the device size. The result of this sequential mean free path analysis is shown as a function of energy in fig. III-4.

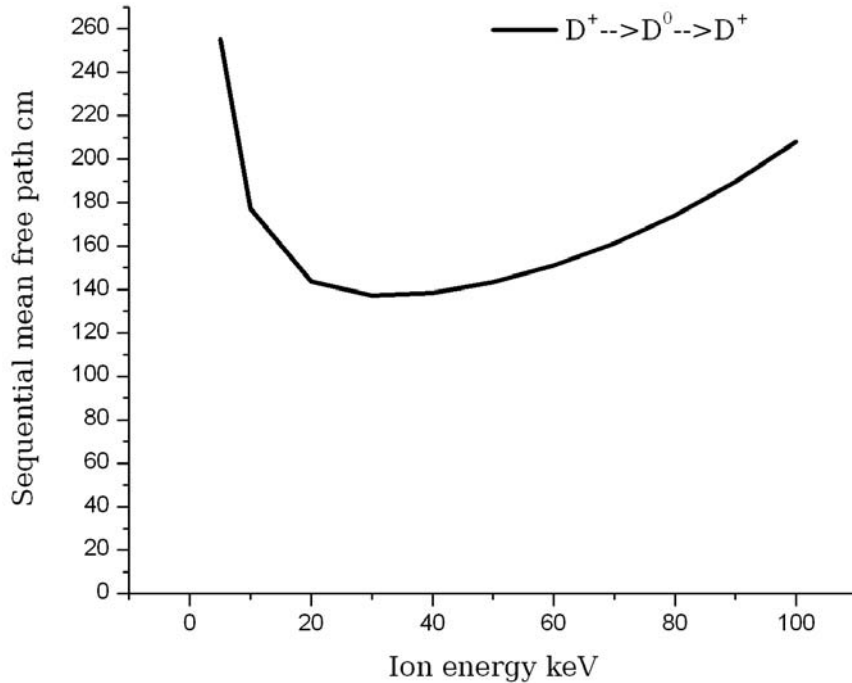


Figure III-4: Sequential mean free path for atomic ions to produce atomic fast neutrals and those fast neutrals to become atomic ions in a 2 mTorr D_2 gas at room temperature, when the particles have between 5 to 100 keV of kinetic energy.

This analysis shows the sequential mean free path length for an ion to produce a fast neutral which then produces an ion is much longer than the HOMER IEC device chamber diameter of 91 cm. For this reason, an effort to model currents in an IEC device can neglect ionization of fast neutrals from collisions with background gas.

- (III-1) E. C. Alderson and J. F. Santarius, "Analytic determination of the mean free path of sequential reactions," *American Journal of Physics*, vol. 80, no. 4, p. 316, Apr. 2012.
- (III-2) R. Clausius, "On the mean length of the paths described by the separate molecules of gaseous bodies on the occurrence of the molecular motion: together with some other remarks upon the mechanical theory of heat," *Philos. Mag.* 17, 81–91 (1858).
- (III-3) J. R. Lamarsh, *Introduction to nuclear engineering*, Third. Upper Saddle River, NJ: Prentice Hall, 2001.
- (III-4) R.P. Feynman, R.B. Leighton, and M. Sands, *Feynman lectures on physics, Vol. 1*, Addison Wesley, Reading MA, 1963.
- (III-5) E. G. D. Cohen, "Kinetic theory: understanding nature through collisions," *Am. J. Phys.* 61, 524–533 (1993)

IV: Negative ion physics in the VICTER code

This section will outline efforts to model currents in an IEC device, first discussing the methodology pursued in the main code, and then how the code is extended to model negative ion currents in an IEC device. A sample of the results of this extension will be reported in Chapter V: Results. Comparisons between VICTER parametric studies and experimental parametric studies will be explored in Chapter VI: Discussion of results.

IV.1 VICTER code background

The Volterra Integral Code for Transport in Electrostatic Reactors (the VICTER code) was developed by Professors Emmert and Santarius [VI-1, 2] for modeling electrostatically accelerated spherically convergent current fluxes and attenuation as the currents react with a background gas. As applied to an IEC device fueled with deuterium or helium-3 the VICTER code can predict fusion rates and the radial distribution of fusion reactions, within the approximation of the one dimensional geometry the code employs. There is an atomic version of the VICTER code, developed for analyzing helium in a reactor of this geometry, [VI-1] and molecular version of the VICTER code, developed for analyzing hydrogen isotopes, primarily deuterium, in a reactor of this geometry[VI-2].

The VICTER code models currents and sources in an IEC device,

attenuating currents as they travel through and collide with background gas particles. These collisions produce a number of reactions, including charge exchange, dissociation, and ionization. These reactions attenuate the incident ion current, giving rise to fast neutral particles and a daughter generation of cold ions and electrons. The fast neutrals exit the device with the energy they were born at, and the ions respond to the electrostatic field of the IEC device. Slow ions born inside the electrostatic potential of the IEC device are accelerated, but do not have the energy needed to leave the potential well inside the anode radius, so they radially oscillate inside the potential well.

These ion currents born inside the cathode can undergo an infinite number of oscillations, but the currents are attenuated as they travel through the background gas. The attenuating reactions produce further generations of ions and fast neutrals that follow the same behavior. Summing these radial passes and generations of ions produces a Volterra integral source function, which is solved to produce the energy spectrum and currents in a self-consistent manner.

The main portion of the VICTER code solves the ion sources as a function of radius. This source function is easiest to explain using the atomic formalism, in which the slow ions are produced by a single species. The main complexity the molecular code introduces is summing the multiple source species and adding reactions that contribute to the source function

at the radius of interest. In the atomic case, the source term is given in Eqn. VI-1:

$$S(r) = A(r) + \int_{r_{anode}}^r K(r, r') S(r') dr \quad (\text{IV-1})$$

In this case $S(r)$ describes the number of cold ions born per unit time per unit volume at position r , and has two contributions. First, the function $A(r)$ describes ions from outside the potential well that react to produce slow ions at r . Ions from the source region enter the potential with some very low energy (from the plasma temperature) and travel through the potential well. The uncollided fraction of the ions from the source region leave the potential well with the energy it entered with. Second, there is a term for the source of ions produced by all generations of ions oscillating inside the potential well that can contribute the source $S(r)$; this is given by the integral in Eqn. VI-1.

The function $A(r)$ is described by:

$$A(r) = n_g \Gamma(r) \sigma_{total}[T(r)] \quad (\text{IV-2})$$

where n_g stands for gas density, $\Gamma(r)$ is the unattenuated flux from the source region, and $\sigma_{total}[T(r)]$ is the total attenuation cross section (only due to charge exchange in the atomic case) which is a function of kinetic energy $T(r)$ of the uncollided flux.

The function $K(r, r')$ is the kernel that relates (propagates) the source

function $S(r)$ at radius r to all the preceding generations born at radius r' through the source function $S(r')$ and oscillating through r , as explained in fig. IV-1:

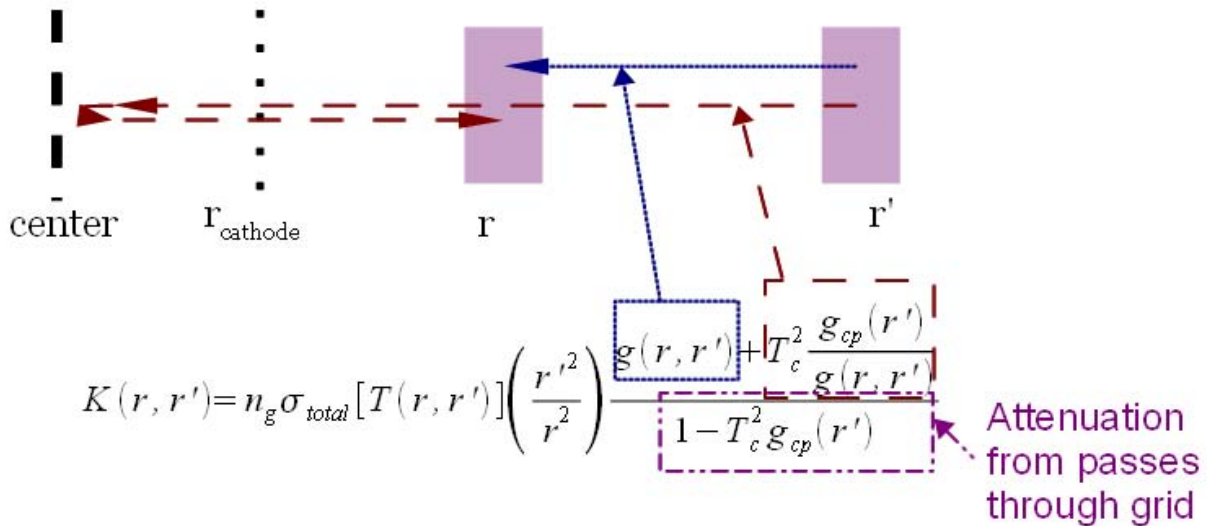


Figure IV-1: Graphical depiction of current sources and how they are described by the kernel used in Eqn. IV-1. The blue arrow (fine dotted line) represents the path of the sum of current sources for currents born inward at radial bin r from currents born at radial bin r' , while the red arrow (dashed line) represents the path of the sum of current sources for the currents born inward at radial bin r from currents born at radial bin r' . The arrows in the diagram omit the oscillations from r' to the center-line before the final pass to react in radial bin r .

In the kernel, $T(r, r')$ is the kinetic energy at radius r of an ion born cold at r' ; it is simply the ion charge times the difference in potential at these two points. T_c is the cathode transparency, which is taken to be the geometric transparency. The function $g(r, r')$ is the attenuation function:

$$g(r, r') = \exp \left(- \int_r^{r'} n_g \sigma_{\text{cx}} [T(r'', r')] dr'' \right) \quad (\text{IV-3})$$

which is the probability of an ion born at radius r reaching radius r' . Here

$\sigma_{cx}[T(r'', r')]$ is the charge exchange cross section at r' , which is a function of the kinetic energy of an ion at r'' , that was born at r' . The term g_{cp} is the complete pass attenuation factor, given by:

$$g_{cp} = g^2(0, r') \quad (\text{IV-4})$$

so that each pass is attenuated by the term $T_c^2 g_{cp}(r')$. Summing over an infinite number of passes produces the factor

$$1 + T_c^2 g_{cp} + (T_c^2 g_{cp})^2 + (T_c^2 g_{cp})^3 + \dots = \frac{1}{1 - T_c^2 g_{cp}(r')} .$$

The negative ion simulation work deals with the molecular version of the VICTER code, as the atomic code is applicable to IEC device operation in helium and the helium negative ion is a short lived metastable state when it does form (from excited states) so will have little impact on an IEC device fueled with helium. In the molecular code there are three species of ions treated: $\{D^+, D_2^+, \text{ and } D_3^+\}$; these three species enter from the source region, and the currents in the IEC device produce currents: $\{D_{\text{fast}}, D^+, D_{2,\text{fast}}, \text{ and } D_2^+\}$, but the only source of D_3^+ is the source plasma. Thus, the source terms for D^+ and D_2^+ are somewhat more complicated than the expression in Eqn. VI-1, that is:

$$S_1(r) = A_1(r) + \int_r^{r_{\text{anode}}} K_{11}(r, r') S_1(r') dr' + \int_r^{r_{\text{anode}}} K_{12}(r, r') S_2(r') dr \quad (\text{IV-5})$$

$$S_2(r) = A_2(r) + \int_r^{r_{anode}} K_{21}(r, r') S_1(r') dr' + \int_r^{r_{anode}} K_{22}(r, r') S_2(r') dr' \quad (\text{IV-6})$$

where, $S_i(r)$ is the source term for species i (1 being D^+ and 2 being D_2^+), A_i represents the ions produced by the current originating outside the anode analogous to Eqn. VI-2, and $K_{ij}(r, r')$ is the kernel, analogous to what is described in fig. IV-1. There are multiple kernel terms in each source term, because the molecular code accounts for the multiple molecular species contributing to the relevant source term $S_i(r)$ so $K_{ij}(r, r')$ relates $S_i(r)$ to the ions from source $S_j(r')$. Due to conservation of energy, $r' > r$ as positive ions cannot be born cold at r' and travel to a higher position in the potential well.

The VICTER code calculates radial and energy profiles of the ion currents based on a number of user provided parameters, including: cathode, anode, and chamber radii; cathode and anode transparencies; cathode voltage; supplied cathode current; background gas density; the fractions of ion species in the source region (D^+ , D_2^+ , D_3^+); and ion temperature outside the anode. An example of the input file is shown in fig. IV-2. From the input cathode current and transparency, and utilizing an energy dependent secondary electron coefficient for the cathode (and assuming perpendicular incidence), the code determines the ion current leaving the source region by imposing a current balance on the cathode. The ion species mix is determined by a separate code that was validated by

an ion acoustic wave diagnostic [VI-3].

Since the discovery of substantial negative ion currents in an IEC device, adding negative ion current modeling capabilities to the VICTER code has been a priority. Modeling negative ion physics is both useful for understanding the significance of negative ion currents in an IEC device and is used to compare against measurements of negative ion currents to validate the VICTER code. Adding negative ion modeling to the VICTER code allows for rapid parametric studies on device parameters with the goal of production optimization. It also provides a way to examine which reactions are primarily responsible for producing negative ions in an IEC device and exploring the physics that gives rise to the spectrum profile. Further, similar to how measurements of fusion reactions are used to test the accuracy of the VICTER code predictions, negative ion current measurements in energy and total current can also be used to further validate the VICTER code predictions.

```
[ input data for IEC multi-species source model, version Dec. 29, 2011]
  [switches]
    field=0          [ potential model, 0=vacuum, 1=Child-Langmuir ]
    coldionswitch=0 [ cold ion switch, 0=don't include cold ions in cathode,
1=include them]
    negativeions=1  [ negative ion switch, 0=skip, 1=compute ]

  [physical parameters]
    a=0.10          [ cathode radius (m) ]
    b=0.25          [ anode radius (m) ]
    c=0.45          [ spherical equivalent wall radius (m) ]
    V0=70.          [ cathode potential (kV) ]
    h1=0.06          [ D+ source fraction ]
    h2=0.23          [ D2+ source fraction ]
    h3=0.71          [ D3+ source fraction ]
    cathodecurrent=30. [ desired total cathode current (ma) ]
    pressure=1.25    [ gas pressure (mTorr) ]
    E0=.01           [ ion energy at anode (keV) ]
    TC=0.92          [ cathode transparency ]
    TA=1.0           [ anode transparency ]

  [radial and energy grid mesh sizes]
    n=100            [ number of zones in the intergrid region, max=100]
    nc=30            [ number of zones in the cathode region, max=50]
    ns=30            [ number of zones in the source region, max=50]
    ng=30            [ number of energy groups for the energy spectra, max =40]
```

Figure IV-2: Example input file for the molecular version of the VICTER code; after defining each parameter, that parameter is described by the following bracketed statement. The switches control how the system is modeled and what optional results are calculated. The physical parameters define the physical system modeled. The grid mesh defines the energy and radial resolution the code uses to model the system.

IV.2 Negative ion physics implementation in the VICTER code

The VICTER code negative ion subroutine follows a series of steps to ultimately calculate the negative ion flux as a function of radius and energy. First, the negative ion source densities (inward and outward directed) are tabulated in matrices from the ion and fast neutral fluxes calculated in the

main code. Next, the negative ion stripping cross sections are used to calculate the survival probability of the negative ions from their birth positions to every position along their path. The negative ion fluxes are then obtained by integrating over the sources coupled with the survival probabilities. The attenuated negative ion flux produces inward and outward fast neutrals from negative ion source matrices, which are integrated to calculate the flux of fast neutrals generated from negative ions. Finally, fusion from these negative ions and fast neutrals is calculated.

The VICTER code is currently equipped to only handle atomic and molecular collisions. It does not model electron currents or collisions. Electron collisions play small role in IEC devices that are primarily sourced with ions from outside the anode, because the electrostatic gradient is strong and the electrons are mobile with a long mean free path. At high pressures an IEC device enters a glow discharge state where the electron collisions are integral to the IEC device operation, and for this reason the VICTER code cannot currently model an IEC device in the glow discharge state. Further, the VICTER code neglects the creation of negative ions from electron attachment inside the cathode of the IEC device as well as neutralization of negative ions from electron impact. However, it is expected that the charge exchange and dissociative reactions are the dominant channel for creation and neutralization (i.e. stripping) of negative ions when the IEC device operates in the single millitorr range of

background pressure. This is due to the low densities of electrons and is supported by the results of the Magnetic Deflection Energy Analyzer.

We model five negative ion creation reactions:



and one neutralization cross section, the electron stripping cross section:



Each fast daughter product is born with the same velocity that its parent had when the reaction that created or destroyed the negative ion occurred, conserving energy and momentum. These reactions' cross sections are plotted in fig. (IV-3).

To model these reactions in an IEC device, it was necessary to have suitable fitting functions for the cross sections of these reactions. Reactions VI-7, 9, and 12 are available in the Oak Ridge National Laboratory Red Book [IV-4], with Chebyshev polynomial of the first kind fitting functions that are within 10% of the data. The cross sections and fitting functions for reactions VI-8, 10, and 11 were obtained from private correspondence and

used with the permission of Arthur Phelps [VI-5].

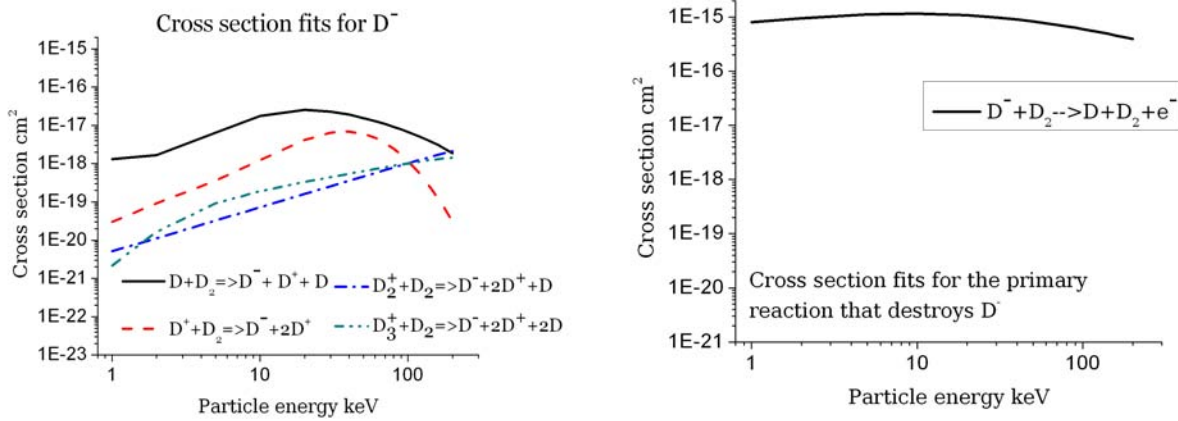


Figure IV-3: Cross section for creation of negative deuterium ions by charge exchange from each parent species (left) and electron stripping of deuterium negative ions (right)

While the main part of the code calculates the ion and fast neutral currents in a self-consistent manner, the cross sections for creation and destruction of negative ions are small enough that attenuation of positive ions and fast neutrals due to the creation of negative ions can be treated as perturbation of the currents calculated by the main code. Even if the negative ion subroutine is not self-consistent in treating the attenuation of parent current, the number of confined particles is consistent: due to conservation of charge when negative ions are born positive ions are born as well.

The ion and fast neutral currents predicted by the main code are used to predict the negative ion source distribution in radius and energy:

$$S_{\pm}^N(r, E) = \sum_i n_g \sigma_i(T) F_{\pm}^i(r, T) \quad (\text{IV-13})$$

The S^N term is the negative ion source density, integrated over a spherical shell at radius r , where the subscripts denote the outward (+) and inward currents (-) currents; the source density from each parent species is tabulated in an inward or outward matrix dependent on radius and total energy. The 'i' subscript or superscript denotes the parent species of negative ion, (D_{fast} , $D_{2,\text{fast}}$, D^+ , D_2^+ , D_3^+), σ_i is the cross section for the creation of negative ions from species 'i', and F^i is the parent flux of species 'i' previously calculated by the VICTER code. The cross section is dependent on the parent species kinetic energy (T), but the source currents are computed using the total energy (E), which is the sum of the kinetic energy and the potential energy from the cathode potential at r .

Motion of negative ions in IEC device

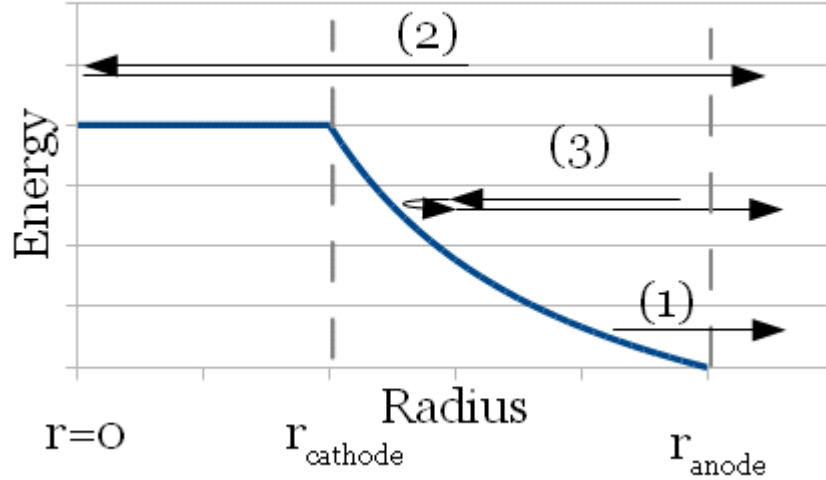


Figure IV-4: The three types of negative ion trajectories, as dependent on total energy and direction. Cathode potential energy is outlined in blue. Negative ions of type (1) are born traveling outward, and are accelerated outward as the the electrostatic potential increases. Negative ions of type (2) are born traveling inward with enough energy to reach the cathode, decelerating as they approach the cathode, pass through the cathode and accelerate outward. Negative ions of type (3) do not have enough energy to reach the cathode, decelerating until they reach a turning point of zero kinetic energy and then accelerate out. The energy of the outward portion of the inward born currents are the same as the inward portion of these currents, but are offset for clarity.

Once the negative ion sources are calculated, their attenuation, dependent on motion, must be calculated. There are three categories of motion, depending on the negative ion total energy, as outlined in fig. IV-4. Negative ions born traveling outwards, class (1), are accelerated outward, responding to the potential between the anode and cathode, until they leave the anode region (where the potential is assumed to be zero) and the currents continue at constant energy. Negative ions born traveling inward produce two categories of motion. Negative ions born inward with total energy greater than the negative ion's charge times the cathode potential,

class (2), decelerate as they travel inward until they reach the cathode, travel through the cathode at constant kinetic energy (where the potential is assumed flat) to the center point, where they become outward traveling negative ions, following the behavior of class (1) negative ions. Inward born negative ions with total energy less than the cathode potential, class (3), have insufficient energy to reach the cathode and decelerate until their kinetic energy reaches zero, where they become outward traveling negative ions, following behavior of class (1) negative ions.

The survival probability of a negative ion in class (1), outward traveling from outward born negative ions, is given by Eqn. VI-14:

$$p_{++}(r, r', E) = \exp \left[- \int_{r'}^r n_g \sigma_s(r'') dr'' \right] \quad (\text{IV-14})$$

where $p_{++}(r, r', E)$ is the survival probability of a negative ion at r , born traveling outward at r' and with total energy E . Because outward born negative ions only travel outward this integral can only be applied for $r > r'$. The stripping cross section σ_s is dependent on the kinetic energy of the particle, and is the difference between total energy of the negative ion and the potential energy at r'' .

Inward traveling negative ions can only come from inward born positive ions. The survival probability of inward traveling negative ions is the same for class (2) and class (3) negative ions:

$$p_{--}(r, r', E) = \exp \left[- \int_r^{r'} n_g \sigma_s(r'') dr'' \right] \quad (\text{IV-15})$$

where $p_{-}(r, r', E)$ is the survival probability of an inward traveling negative ion at r , born moving inward at r' and with total energy E . As this is the survival probability for negative ions traveling inward, $r < r'$. Also, the total energy must be greater than or equal to the negative ion's charge times the potential at r , or the negative ion does not have enough kinetic energy to reach r .

The outward traveling phase of negative ions that were born traveling inward must be considered according to their class. For class (2) negative ions the survival probability of outward traveling from inward born negative ions is given by:

$$p_{-+}(r, r', E) = \exp \left[- \int_0^{r'} n_g \sigma_s(r'') dr'' - \int_0^r n_g \sigma_s(r'') dr'' \right] \quad (\text{IV-16})$$

where $p_{+}(r, r', E)$ is the survival probability of an outward traveling negative ion at r , born inward at r' and with total energy E . The first integral in the exponent covers the attenuation inward from birth position r' to the center of the device, and the second covers the attenuation outward from the center of the device to r .

For class (3) negative ions the survival probability of outward traveling from inward born negative ions is given by:

$$p_{-+}(r, r', E) = \exp \left[- \int_{r'}^{r_t} n_g \sigma_s(r'') dr'' - \int_{r_t}^r n_g \sigma_s(r'') dr'' \right] \quad (\text{IV-17})$$

where r_t is the turning point radius at which the negative ion's kinetic energy reaches zero, and the negative ion becomes an outward traveling negative ion. Thus the first integral in the exponential covers the attenuation inward from the birth position r' to the turning point and the second integral covers the attenuation outward from the turning point to r .

Based on these quantities, the negative ion current density matrices can be calculated. For inward traveling negative ions the current density is calculated from:

$$F_-^N(r, E) = \int_{r_{anode}}^r S_-^N(r', E) p_{--}(r, r', E) dr' \quad (\text{IV-18})$$

Physically, this integral represents integrating from each birth position to each r position the current can reach with total energy E , starting at the anode and continuing inward.

The outward traveling negative ion current density has two components. For negative ions of total energy E greater than the cathode potential there is a contribution from class (1) and class (2) negative ions:

$$\begin{aligned}
F_+^N(r, E) &= \int_0^r S_+^N(r', E) p_{++}(r, r', E) dr' \\
&+ \int_0^{r_{anode}} S_-^N(r', E) p_{-+}(r, r', E) dr'
\end{aligned} \tag{IV-19}$$

For negative ions of total energy E less than the cathode potential there is a contribution from class (1) and class (3) negative ions:

$$\begin{aligned}
F_+^N(r, E) &= \int_{r_t}^r S_+^N(r', E) p_{++}(r, r', E) dr' \\
&+ \int_{r_t}^{r_{anode}} S_-^N(r', E) p_{-+}(r, r', E) dr'
\end{aligned} \tag{IV-20}$$

where r_t is the turning point for inward traveling negative ions; there can be no current with total energy less than the potential energy, so the integral for outward traveling current begins at the previously defined turning point as well.

As the negative ions are attenuated, they produce fast neutral fluxes, which are calculated in a similar series of steps as above. Inward and outward source density matrices for fast neutrals from negative ions are calculated from the negative ion fluxes, and the fluxes of fast neutrals from negative ions are calculated from these sources. As in the main code, attenuation of fast neutrals is neglected. The source of fast neutrals from negative ions is given by:

$$S_\pm^a(r, E) = n_g \sigma_s F_\pm^N(r, E) \tag{IV-21}$$

This is used to produce the fast neutral flux from negative ion fluxes, similar to how it is calculated in the main code. For the inward fast neutral fluxes the total flux is the source density integrated from the anode to r:

$$F_{-}^a(r, E) = \int_r^{r_{anode}} S_{-}^a(r', E) dr' \quad (\text{IV-22})$$

For the outward fast neutral fluxes the total flux is the sum of the inward source densities integrated from the anode to the center of the device and passed through the center of the device, and the outward flux from 0 to r:

$$F_{+}^a(r, E) = \int_0^{r_{anode}} S_{-}^a(r', E) dr' + \int_0^r S_{+}^a(r', E) dr' \quad (\text{IV-23})$$

Using the negative ion and fast neutrals from negative ions fluxes a fusion radial profile and fusion rate are calculated and added to the appropriate tallies.

As the negative ion fluxes are calculated in terms of the total energy E, a post processing routine is applied to display the output in terms of the kinetic energy T. Also, to compare with the total measured negative current density, the negative ion current can be integrated with respect to energy at the measured radius and divided by the area of a sphere of that radius to produce the total negative ion current density in assuming spherical symmetry. This approximates the discrete jet formation that is

experimentally observed, and provides a point of comparison between experiment and simulation.

This formalism is complete; the negative ion fluxes at any radius and total energy in the IEC device can be calculated from the parent flux at any birth radius. However, when calculating the total flux and energy spectrum across all of the radial space in the IEC device it is possible to improve on the algorithmic above for reasons of computational efficiency.

As outlined above, the survival probability is recalculated for every position r and r' , for every total energy. It is more efficient to recognize that the survival probability at $p(r+\Delta r, r', E)$, when the integral is evaluated using the trapezoidal rule approximation, is the evaluation of the integral from r to $r+\Delta r$ added to the integral from r' to r . Thus, a single trapezoidal element is added to the integral evaluated for $p(r, r', E)$ to calculate $p(r+\Delta r, r', E)$, saving calculations. Using this framework, the code starts with each birth position and energy, calculates the flux from that source to every radial bin the source current reaches in the IEC device, and then proceeds to the next energy bin until the current density across the energy spectrum from that source position is complete. The code then proceeds to the next birth position.

This formulation has been successfully added to the VICTER code, predicting results that can be bench marked against experimental results.

- (IV-1)G. A. Emmert and J. F. Santarius, "Atomic and molecular effects on spherically convergent ion flow. I. Single atomic species," *Physics of Plasmas*, vol. 17, pp. 013502, 2010.
- (IV-2)G. A. Emmert and J. F. Santarius, "Atomic and molecular effects on spherically convergent ion flow. II. Multiple molecular species," *Physics of Plasmas*, vol. 17, pp. 013503, 2010.
- (IV-3)D. R. Boris and G. A. Emmert, "Composition of the source region plasma in inertial electrostatic confinement devices," *Physics of Plasmas*, vol. 15, no. 8, pp. 083502, Aug. 2008.
- (IV-4)C.F. Barnett, "Atomic Data for Fusion Vol. 1" *Controlled Fusion Atomic Data Center*, 1990.
- (IV-5)A. V. Phelps, "Collisional kinetics of non-uniform electric field, low-pressure, direct-current discharges in H₂," *Plasma Sources Science and Technology*, vol. 20, no. 4, pp. 43001, 2011.

V. Experimental approach

V.1 Laboratory facility

The UW-IEC Advanced Fusion Fuels Laboratory is a facility that supports three IEC fusion devices (HOMER, HELIOS, and SIGFE) and a fusion materials testing experiment (MITE-E). These devices are depicted in fig. V-1.

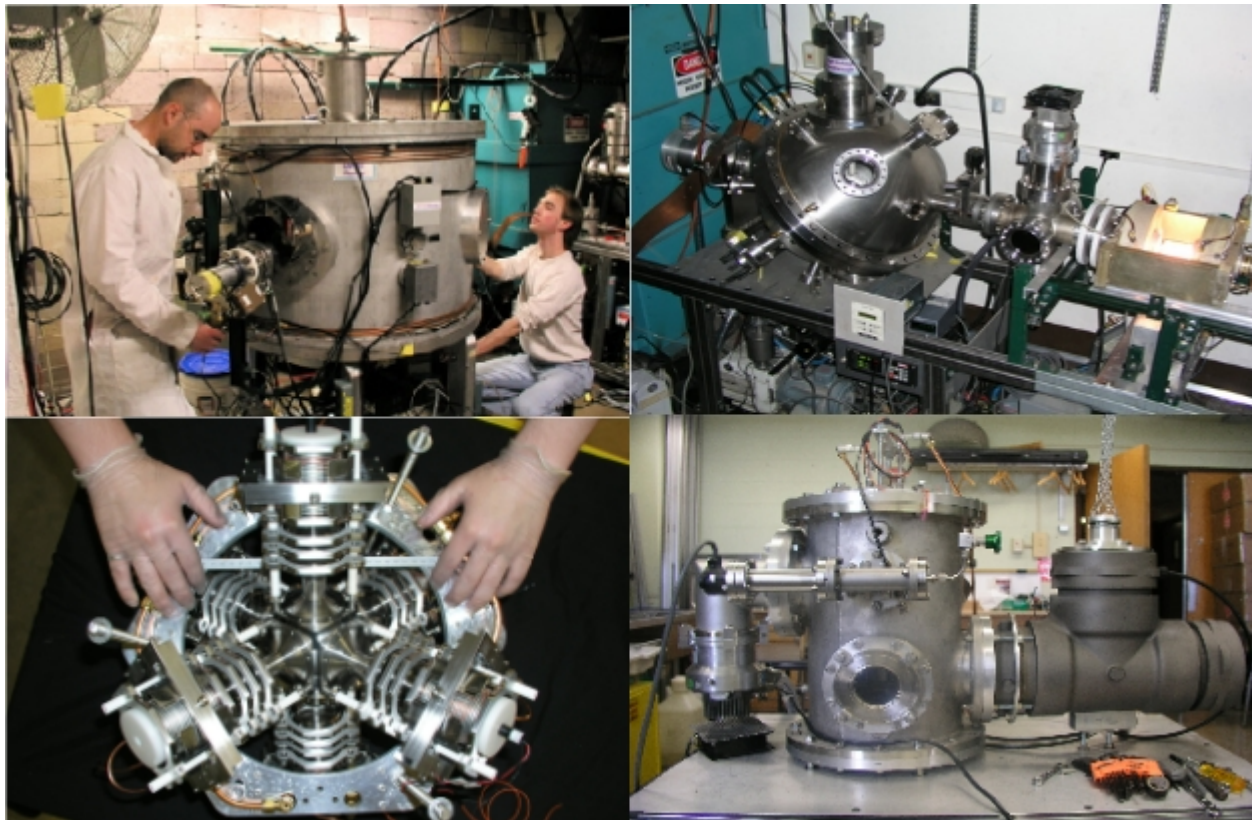


Figure V-1: The four experimental devices in the UW-IEC laboratory clockwise from the top left: HOMER, HELIOS, MITE-E, and SIGFE.

As these devices all produce radiation of varying degrees, including

neutrons in the case of HOMER and SIGFE, the UW-IEC laboratory has a radiation vault that is sufficient to shield the operators and surroundings from the radiation produced by the housed experiments, utilizing a 1.3 m thick concrete and brick walls and a lead door. The UW-IEC laboratory is outfitted with cold water hookups for cooling, a gas manifold able to deliver a variety of species of gas to the experiments, and a high voltage power supply able to provide between 1 and 300 kV negative voltage, at up to 150 mA of current. There is also a biasing DC power supply for supplying between 0-100 volts negative biasing and heating power to filaments for the creation of filament assisted plasma discharges, which act as source plasmas in HOMER, MITE-E, and SIGFE. Grounding loops are mitigated by the use of a universal grounding strap that runs the perimeter of the UW-IEC laboratory radiation vault. Each experiment has its own suite of diagnostics, and all experiments utilize a common neutron detector mounted on the vault wall.

The controls for the high voltage power supply and the filament power supply are located in the control room. Computers for data collection are located in the control room, outside the radiation vault. Most data is collected by a data acquisition system automated by LabView® control; a hand entered record is also added to a logbook database. Controls for gas flow controllers in the gas manifold are in the control room, but the the gas manifold and gas tanks are in the radiation vault so the associated valves

must be opened and closed manually when the IEC devices are not in operation.

V.2 HOMER IEC Device

The HOMER IEC device has been utilized in this negative ion experimental research. A basic schematic of HOMER is in figure V-2.

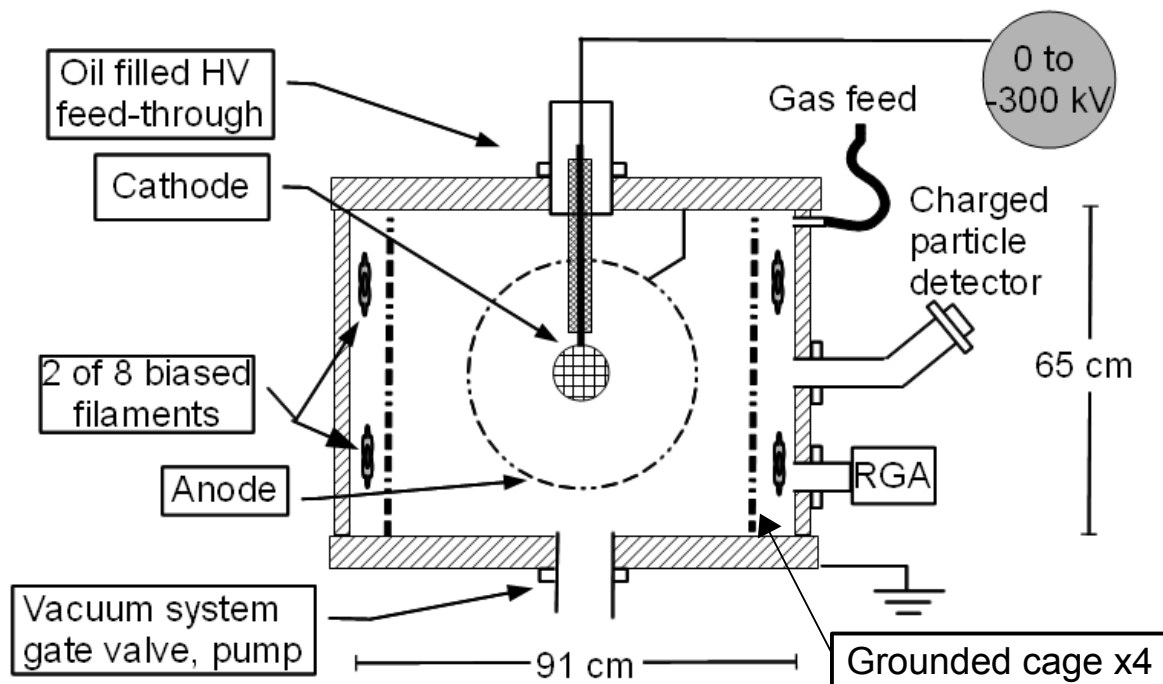


Figure V-2: Diagram of the HOMER Inertial Electrostatic Confinement device.

HOMER can broadly be described as having three regions separated by a spherical cathode and a spherical anode. The innermost region is the cathode region. Surrounding that region is the anode region. Surrounding

these two is the plasma source region.

The cathode in HOMER is suspended by a high voltage stalk. This stalk and high voltage vacuum feed-through assembly is able to deliver between 0 to -200 kV negative voltage to the cathode when in operation. The anode is suspended from the vacuum chamber cover, in electrical contact with the grounded chamber. As discussed in section II.1, an electrostatic well is formed between the anode and cathode, to the depth of the cathode voltage.

The filaments that emit electrons throughout the source region in the HOMER IEC device are situated in four columns spaced 90 degrees apart on the wall of the HOMER chamber, with two biased filaments in each column to produce electrons that ionize gas outside the anode, which acts as a source plasma. Electrostatic potential from the cathode does leak past the anode mesh to the wall; when the cathode voltage is high enough the potential in the source region overwhelms the bias on the filaments, repressing electron emission, effectively eliminating the source plasma. To prevent this, the columns of filaments are shielded by grounded cages. A \sim 3-5 eV temperature plasma with a density of \sim 10⁶ cm⁻³ is present when the cathode is at operating voltage [V-1].

The vacuum electrostatic potential profile is calculated and scales with the inverse of the radius between the anode and cathode. As the

current in HOMER is 10's of mA in a potential well 10's of kV deep the space-charge effects are small, so the potential profile is somewhat less steep than the Child-Langmuir potential and is essentially the vacuum potential. The potential profile is expected to be somewhat peaked inside the cathode and relatively flat outside the anode, as discussed in Chapter II, and shown in fig. II-1.

V.3 High voltage switch

For an IEC device cathode to reach a desired voltage the cathode must be electrically connected to a power supply capable of providing that voltage, and the electrical connection must be engineered to deliver that voltage without failure. While the current power supply in the UW-IEC laboratory can provide -300 kV, the electrical connections were engineered to withstand a -200 kV voltage, as that was the limit of the UW-IEC laboratory's previous power supply. Improving the high voltage system in the IEC laboratory has been a extended campaign that all members of the IEC laboratory staff have contributed to. While this work does not directly contribute to the effort to study negative ion profiles in an IEC device, this novel and useful work has not been published elsewhere.

The high voltage system in the UW-IEC laboratory consists of the power supply, cabling rated above a 300 kV capacity, an oil filled barrel housing an inline resistor chain to limit the current (and thereby the power)

in arcs, the high voltage vacuum feed-through and the stalk that connects to the cathode. A high voltage vacuum feed-through designed to accommodate 300 kV has been designed and outlined in previous work [V-2], and is expected to be fully implemented in 2012.

Power cables rated above 300 kV are commercially available, but utilizing them add complexity to the operation of the UW-IEC laboratory. The cables rated to 300 kV are not as robust to flexing as the cables rated to 200 kV that the UW-IEC laboratory used previously. In the previous high voltage system the barrel housing the inline resistor system is used as the terminal that cables are plugged into, connecting the power supply and resistors to the experiments in the UW-IEC laboratory. The flexing to plug and unplug cables from the resistor system would stress the high voltage cable rated to 300 kV, potentially causing degradation and failure. Utilizing the cable rated to 300 kV requires a high voltage switching system that allows changing the connections between the high voltage power supply and experiments without moving the cabling. Further, a resistor system able to accommodate a 300 kV capacity must also be implemented.

Finally, the UW-IEC laboratory is interested in continuing experiments that operate in a pulsed mode. In the previous system a barrel housing high voltage capacitors and resistors was connected inline between the resistors and power supply to provide capacitance in parallel with the power supply, so the voltage does not drop when current in the cathode is pulsed [V-3]. To

minimize stress to the cabling, minimize disruption of laboratory operations when engaging the pulsing system, and minimize the floor space required, it was decided that the high voltage switch will also house the pulsing capacitor system and be able to switch it into operation.

To design a system that can deliver these goals, a prodigious amount of modeling was done. The design criteria are to produce a system that keeps the peak field below ~ 6 MV/m with 300 kV applied to the electrodes, has more than 15.24 cm of dielectric oil filled distance between the high voltage electrodes and ground, and the surface length along non-conducting surfaces between the high voltage electrodes and ground (i.e. supports) greater than 40.64 cm [V-4]. Modeling was performed with Maxwell-3D™ [V-5]; using these criteria it was determined that the high voltage electrodes had to have a diameter greater than 10.16 cm while keeping the nearest grounded surface more than 15.24 cm away, minimizing the size of the switch. The dielectric properties for modeling purposes were taken from the oil specifications data sheet of the Diala® A X oil provided by the manufacturer, Shell Oil company. Specifically, the data sheet provided the relative permittivity range of 2.2-2.3 and a resistivity of 2×10^{15} $\Omega \cdot \text{cm}$ at 25°C. The modeling showed cylindrical electrodes with hemispherical ends are most successful in reducing field concentration.

The resistors that were used have very small features, namely a fin profile to maximize cooling. However, these small features are also sites for

field concentration, so it was decided to surround the resistors in a conductive shield that would also serve as an electrode. This resistor shield reaches the same potential that is delivered to the IEC device. This means the voltage difference inside the shield is no more than the voltage drop from the top of the resistor system to the end. This shield also gives flexibility to install multiple strings of resistors in parallel, which can be engaged selectively to vary the amount of inline resistance and resistive heat load on the resistors. The resistors are installed on strings of printed circuit boards, providing robustness and surety of connection, as illustrated in fig. V-3.

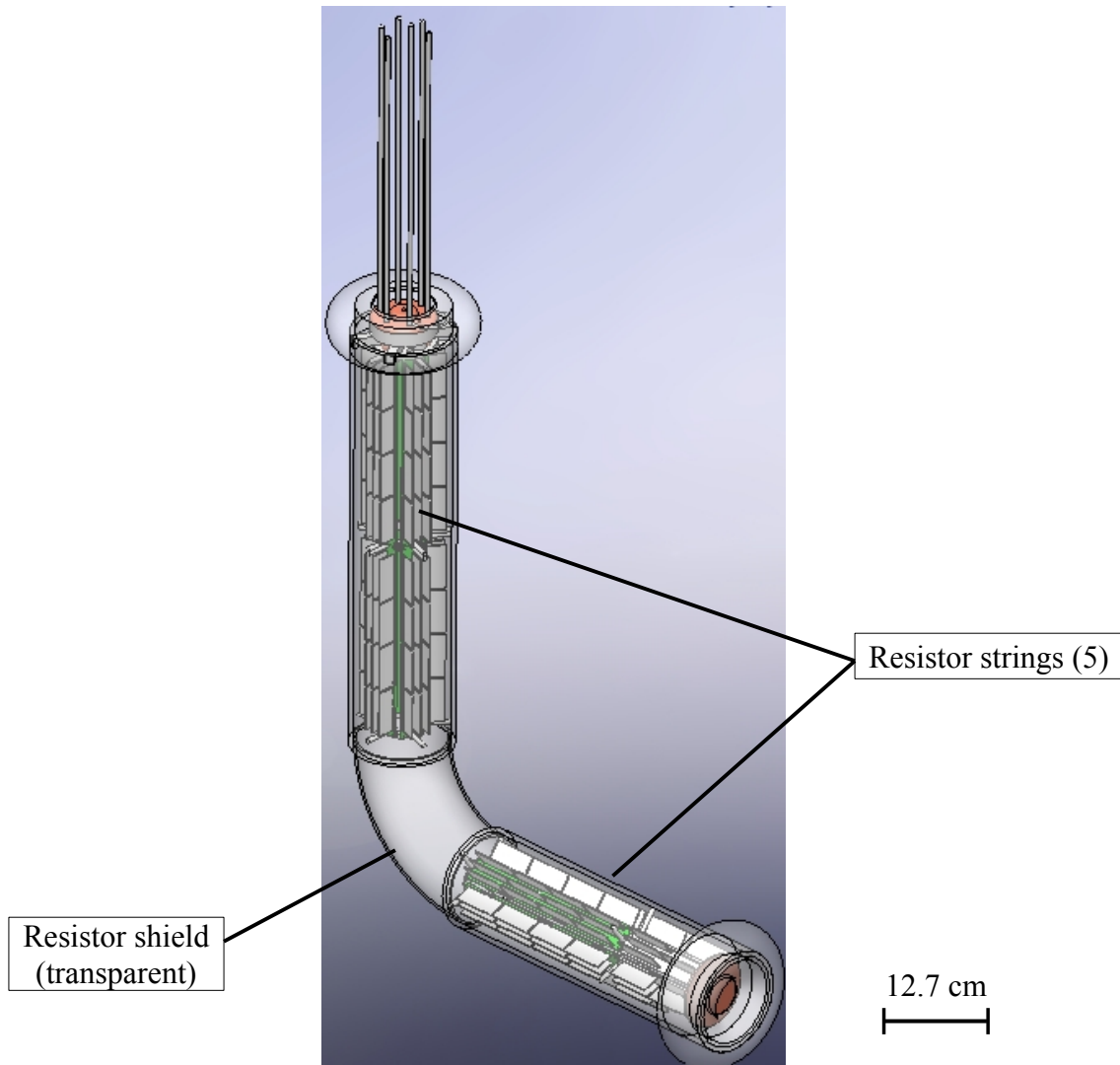


Figure V-3: Diagram of resistor system, with shield made transparent. The printed circuit boards are green and the resistors are the white 'fins'. The strings of resistors are arranged in a pentagon, each face a continuous string. At the top is a switch assembly to engage or disengage the strings from the power supply to the shield which is connected to an experiment. One of the switch pins controls a short that bypasses the resistors altogether.

A series of moving electrodes is used to connect the high voltage power supply and resistors to the experiments. Power flows through the resistors to the shield, which acts as an electrode, and is connected by cable to a selection electrode that rotates into position to connect to an

experiment. The selection electrode and the electrode connected to each chamber are engaged by a bridge electrode that is raised into position. This double action to create a connection between the power supply and experiment ensures that a connection cannot be inadvertently made, creating a reliably safe system. The layout of connecting electrodes and the resistor shield electrodes was modeled in Maxwell-3D™ [V-5], the result of many iterations is illustrated in fig. V-4.

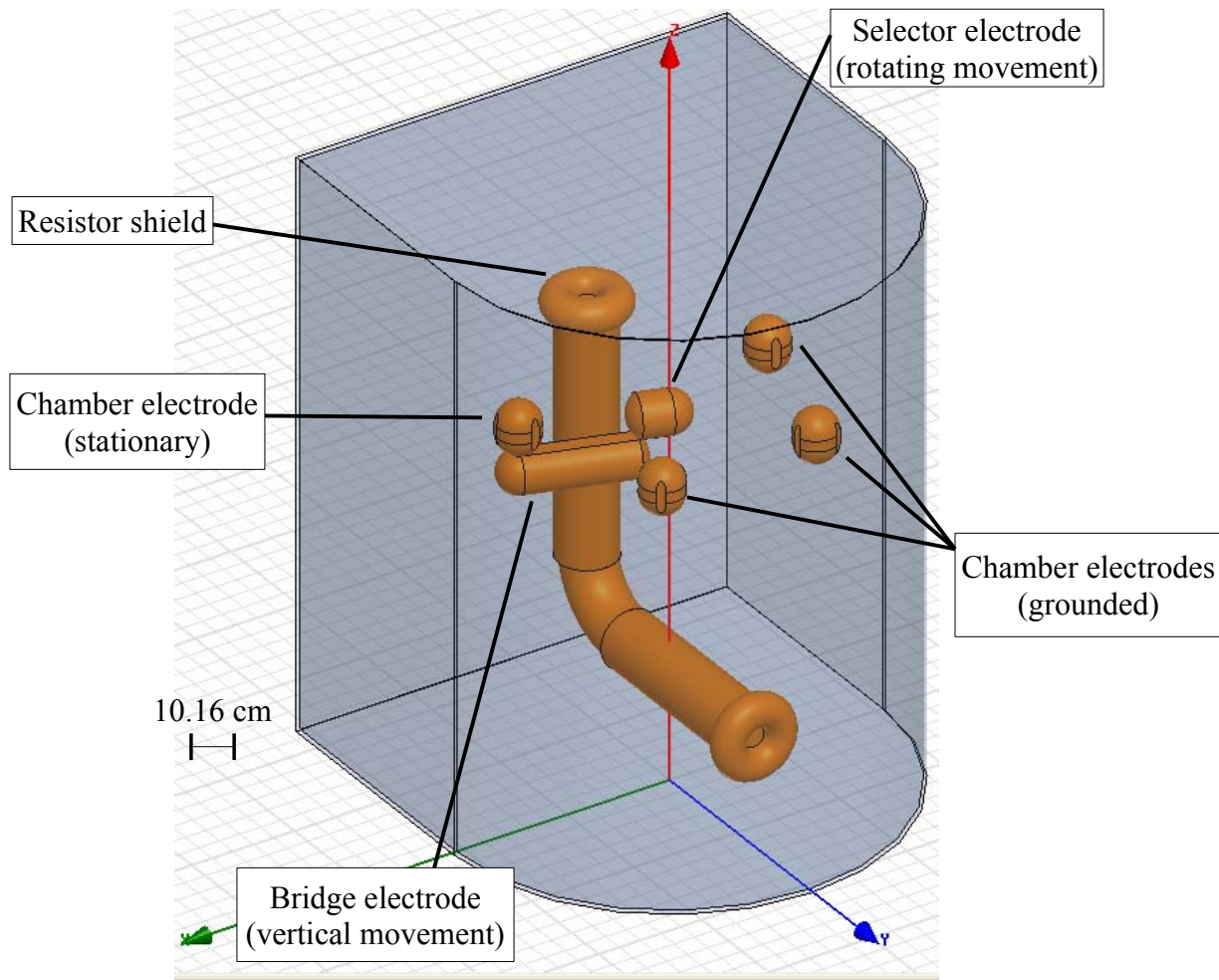


Figure V-4: Electrode arrangement and grounded tank laid out in Maxwell-3D™. The large L-shaped assembly holds the resistor strings within, the top of which is connected by high voltage cable to the power supply. This electrode is connected by a high voltage cable that runs along the z-axis to the selector electrode, which is connected by the shown bridge electrode (the other three bridge electrodes are not shown) to the chamber electrode which is connected by cable to an experiment by a high voltage cable. Only the connected chamber electrode is at voltage, the others are grounded.

The tank that houses the switch is held at ground. In modeling the resistor shield, the selector electrode, the bridge electrode and the engaged chamber electrode are held at 300 kV. The chamber electrodes that are not engaged are held at ground; the bridge electrodes that are not connected

may float in potential and are not modeled. The results of this simulation are shown in fig. V-5.

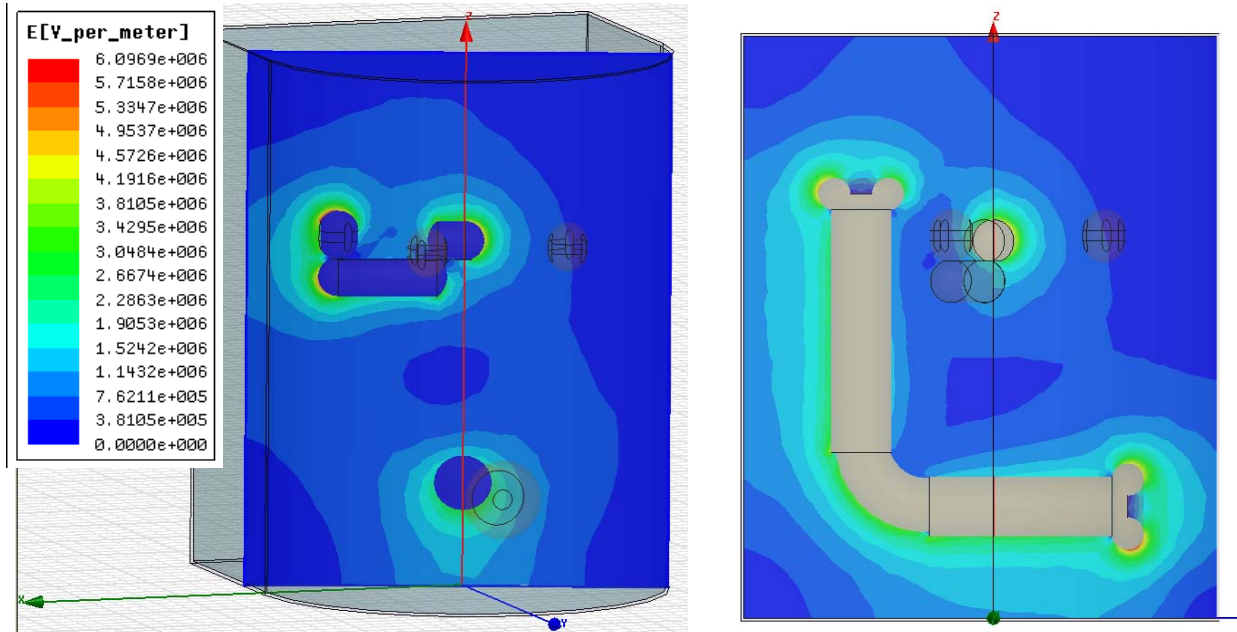


Figure V-5: Electrostatic fields in switch as modeled in Maxwell-3D™ with 300 kV applied to the electrodes. Left shows fields in the plane of the bridge electrode axis, right shows the field in the YZ-plane.

Once satisfied that the fields would be within specifications a more detailed design was made in SolidWorks®. The electrodes at voltage in the model pictured in fig. V-5 are shown with support structure in fig. V-6.

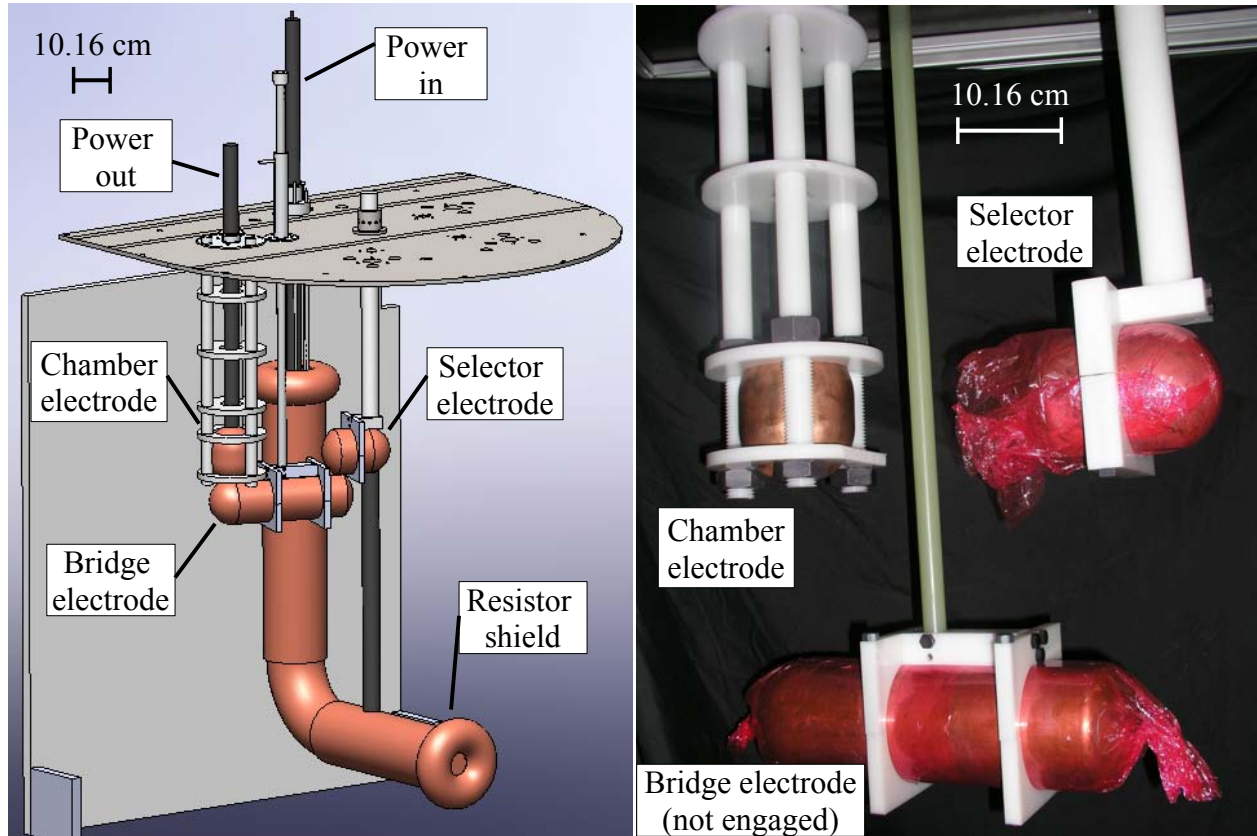


Figure V-6: Left: SolidWorks design of a set of connected electrodes with support structure. Right: the constructed electrodes, hanging with support structure from the lid of the switch as they are installed in the switch. The selector electrode and bridge electrode are covered in a plastic wrap to protect the copper plating on the aluminum electrode bodies during assembly.

The assembly of the entire switch, as designed and constructed, is shown in fig. V-7.

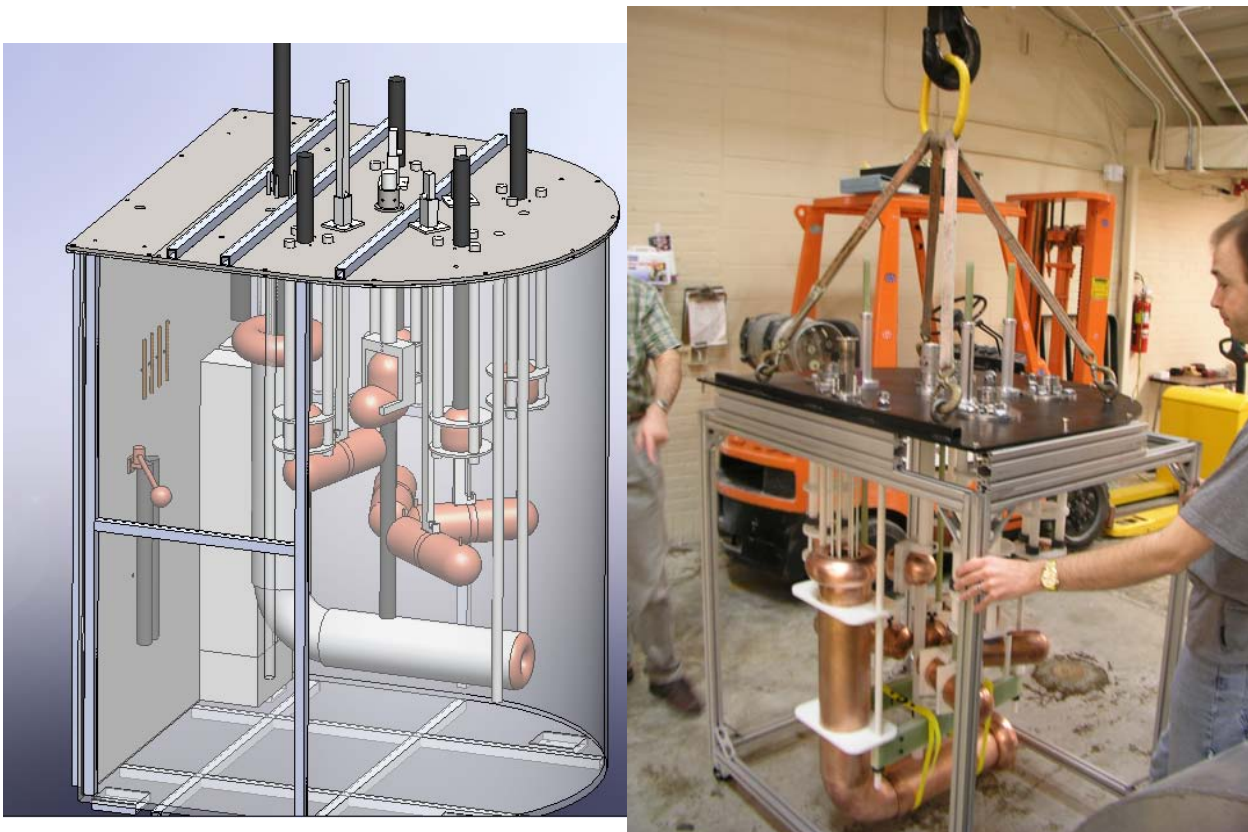


Figure V-7: (Left) Full SolidWorks assembly of the high voltage switch design; on the rear wall of the tank is the pulsing system, which is engaged by rotating the rod and ball into contact with the resistor shield electrode. (Right) Constructed switch elements before installation in the switch tank for initial testing. The tank and the pulsing system are not shown here.

Testing of the high voltage switch at 100 kV while the switch is filled with air indicates operational capability at 300 kV when the switch is eventually filled with high voltage oil. The air filled switch has passed a high pot test to 100 kV when not connected to anything. Unfortunately, the air filled switch connected to an IEC device (at vacuum) has demonstrated previously unobserved arcs of microsecond scale that draw enough current to cause the power supply overload sensor to fault and shut down. Further modeling suggests that the problem is capacitance between the resistor

shield and the ground tank storing enough energy between the resistors and IEC device that small arcs can draw a great deal of current. Filtering out high speed signal to the power supply controller has not made an appreciable difference in operation. A $85\ \Omega$ resistor in the high voltage feed-through has allowed the HOMER IEC device to reach 100 kV, but not stably. It is expected a higher value resistance ($1\ k\Omega$) will produce the desired performance when the high voltage switch is fully integrated in to UW-IEC laboratory operation.

V.4: Design of a movable Faraday cup for use in the HOMER IEC device

V.4.1: Motivation

While the underlying physics that governs the creation, destruction, and acceleration of negative ion current is reasonably well understood, an IEC device has inherent complexities requiring experimental measurement to underpin our understanding of this current in an IEC device. Previous work has shown that the negative ion current varies with azimuthal angle [V-6,7] and a similar response to elevation angle is expected. Variation of negative ion current with radius is fully expected from theory and modeling. The negative ion current profile must be measured to produce a complete picture of the shape of variation of the currents in an IEC device.

The negative ion current changes with radius due to reactions with the background gas that both create and attenuate the negative ion current. The kinetic energy of the reacting species also depends on the birth position of the parent and is thus a function of radius from the center of the cathode, which adds further complexity to modeling these reactions, as outlined in Chapter IV.

As the cathode and anode are highly transparent grids with discrete wires, the equipotential contours produced by this system are not spherically symmetric; they are strongest at the wires and weakest at the center of the holes between the wires, as illustrated in fig. V-8. This results in a rippled potential structure, causing negatively charged particles to channel where the negative potential is at a minimum in the holes between the cathode wires. This phenomenon gives rise to the IEC device jets visually observed in IEC devices with cathodes of small radius operated at high background pressure[V-8,9].

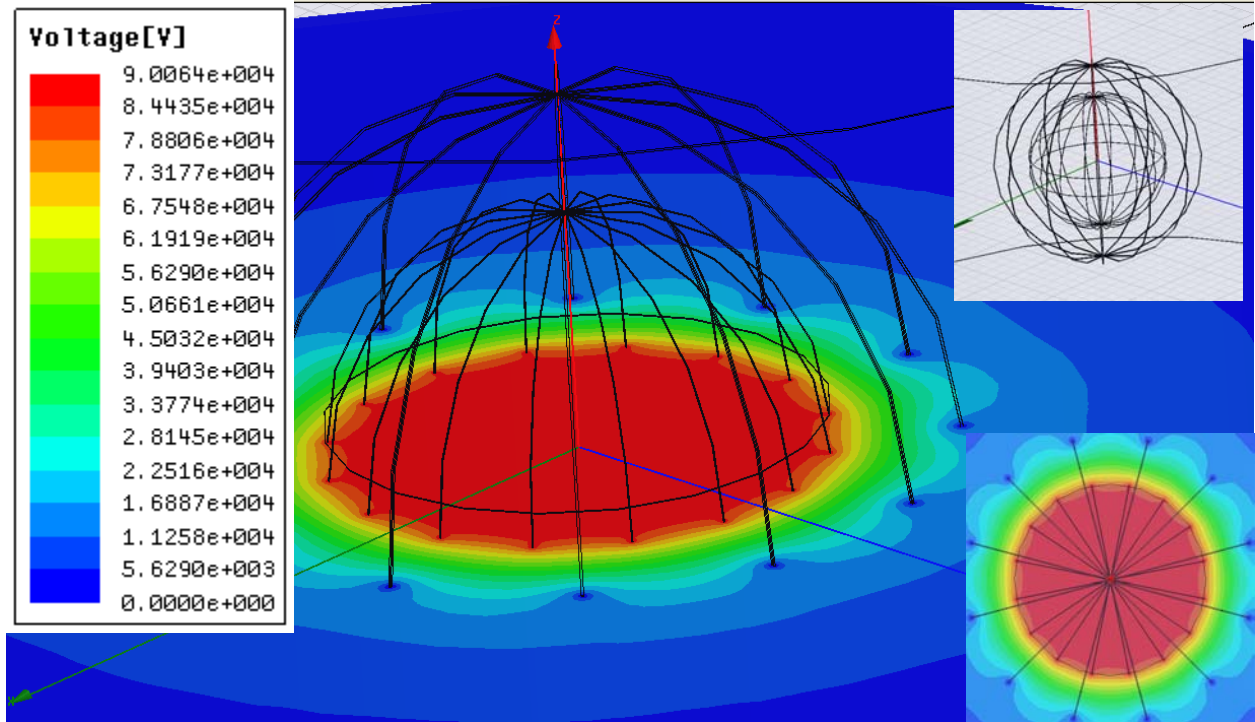


Figure V-8: Results of a Maxwell-3D™ simulation of the potential at the equator of an IEC device with a cathode of 20 cm diameter at applied potential of 90 kV and anode of 30 cm diameter at ground potential. This simulation shows a nearly 30% dip in potential between the cathode wires. Inset top is an isometric view of the simulated anode and cathode grids and inset bottom is a top down view of the simulation. Note, only two latitude lines are included in the simulation to reduce complexity of the simulation. It is expected the latitude lines far from the equator have less influence on the potential at the equator.

Measuring the spatial profiles of the negative ion currents is important, both for understanding the negative ion physics in the IEC device as well as providing a means to further understanding of the IEC device.

Because the negative ion current varies with the azimuthal and elevation angles, it is impossible to estimate the total negative ion current at a given radius and operating condition without an understanding of the

negative ion current spatial profile. In a cathode where the spaces between grid wires are of equal area the jets leaving each grid hole are believed to be roughly equal. Making this assumption, in a latitude-longitude cathode grid, an azimuthal scan of the negative ion current leaving the anode in a jet can be used to make a reasonable extrapolation of the total negative ion current at a given radius in an IEC device. This, coupled with the energy spectrum, informs an estimate of the negative ion current contribution to the IEC device's total fusion rate.

Not only can a profile measurement tell us about the negative ions themselves, but it can also tell us about the physics inside the IEC device anode, which is not easily probed due to the high potentials in the IEC device at fusion relevant operating conditions. The negative ions are a constituent of the IEC device jets, so measuring the width of the jets can tell us about how the jets respond to system parameters both in magnitude and dimension.

V.4.2: Requirements for measuring the negative ion spatial profiles

To measure the negative ion profiles the detector must be mobile enough to sweep the desired profiles, able to isolate the negative ions from other charged particles, and insensitive to x-rays. While it would in principle be possible to move the IEC device cathode relative to a stationary detector, doing this would not be a trivial task, so a mobile detector is

preferred [V-10]. This detector must not produce spurious readings from energetic electrons or the thermal plasma outside the anode. As stated above, secondary electrons due to energetic particles impacting the cathode get accelerated outward, striking the wall and producing a considerable x-ray flux that the detector must contend with.

Solid-state charged particle detectors can be used to measure negative ions, however they are overwhelmed by x-ray noise when used in the line of sight of the IEC device chamber, and shielding against this while still measuring negative ion current is not possible. The UW-IEC group has had success isolating the negative ion current from all other charged particles and x-ray flux using the Magnetic Deflection Energy Analyzer (MDEA), described in Chapter II. The MDEA utilizes a magnetic field to bend the negative ions out of the field of view of the IEC device cathode into a solid-state detector [V-6, 7]. While the MDEA has been successful in measuring negative ions, it is not mobile, and therefore not suitable for measuring negative ion spatial profiles.

A Faraday cup is, at its most basic, an arrangement of electrodes engineered to collect and measure a charged particle current while minimizing spurious signals, such as secondary electron emission [V-11]. So long as an amplifier can create a measurable signal from the collected current, a Faraday cup can be nearly arbitrary in size. Finally, a Faraday cup is insensitive to x-ray flux. If the Faraday cup isolates negative ion flux

from other charged particles it represents a suitable detector technology for measuring negative ion spatial profiles.

V.4.3: UW-IEC Faraday Cup Design

Many Faraday cups use electrostatic potentials to filter the energy of the incident charged particles, but in an IEC device fast electrons leaving the cathode are of equivalent energy to the negative ions, so this option is not suitable. However, at equivalent energy, the momentum of the fast electrons is much lower than that of the negative ions. Since the gyroradius of two charged particles in a magnetic field is equivalent when they have the same momentum per charge ratio, a magnetic field can be used to bend the low momentum electrons and cold ions away from the collection electrode of a Faraday cup. This allows the collection of the high momentum negative ions with much larger bending radius in the same magnetic field.

To design a Faraday cup that successfully filters all other charged particles except energetic negative ions, the desired magnetic fields must first be calculated, and arrangements of magnets must be modeled to determine how to achieve the desired field. A 1.5 cm long deflection region in front of the collection electrode can be used to effectively deflect 100 keV electrons away from the collection electrode with 7 Gauss or greater, according to eqn. (1):

$$\frac{v m}{q r_b} = B \quad (\text{V-1})$$

where

- v is the particle velocity
- m is the particle mass
- q is the charge of the particle
- r_b is the bending radius
- B is the magnetic field strength

Over the same 1.5 cm bending region, a 5 eV thermal ion population from the source plasma will be deflected away from the collection electrode with 300 Gauss or greater, according to eqn. (2):

$$\frac{1.02 \times 10^2 \sqrt{(\mu T_i)}}{Z r_b} = B \quad (\text{V-2})$$

where

- μ is the ratio of ion mass to proton mass
- T_i is the ion temperature in eV
- Z is the charge state of the ion

If the field is too strong the lower energy negative ions will also be deflected away from the collection electrode. Using eqn. V-1 again shows

that so long as the field is below 4300 Gauss negative ions will have a bending radius that exceeds the 1.5 cm bending region and therefore will impact the collection aperture. With a defined solution space it is possible to design a magnetic system to provide a magnetic field in the desired range. It is possible to produce this field using electromagnets, but permanent magnets are more compact and less technically complicated. The main drawback to permanent magnets is their demagnetization if they get too hot.

The relatively strong magnetic field requires the use of rare earth magnets, such as those supplied by K&J Magnetics. Using their N42SH high temperature neodymium magnets with the dimensions 2.54 x 1.27 x 0.3175 cm, with a surface field of 2186 Gauss magnetized through the 0.3175 cm thickness, we can model the field these magnets would produce in pairs using Maxwell-3D™'s magnetostatics modeling capabilities [V-6]. By truncating the scale of the results above 300 Gauss it is shown that the magnetic field is strong enough to deflect the thermal ions and fast electrons, as shown in fig. V-9. By truncating the scale of the results above 4300 Gauss we can show that the field strength is not enough to deflect the negative ions, as shown in fig. V-10. In this simulation the magnets are held 3.3 cm apart.

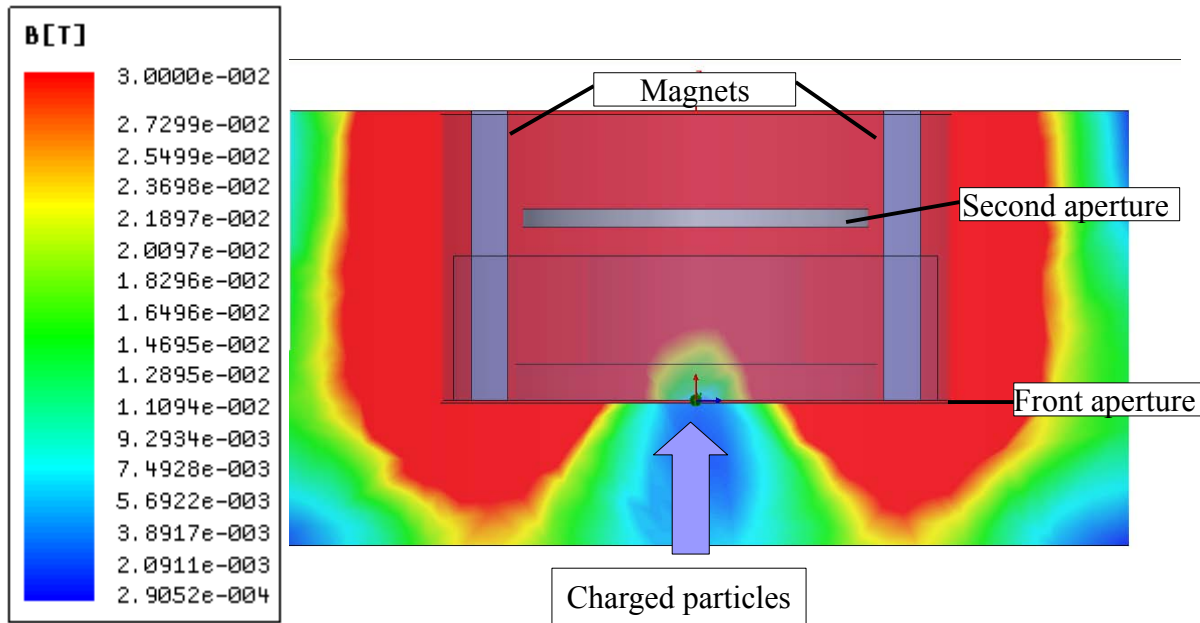


Figure V-9: Maxwell-3D™ magnetostatics model of two K&J Magnetics BX082SH magnets held 3.3 cm apart, with the magnetic scale truncated above 300 Gauss to show that thermal ions will not penetrate to the collection aperture.

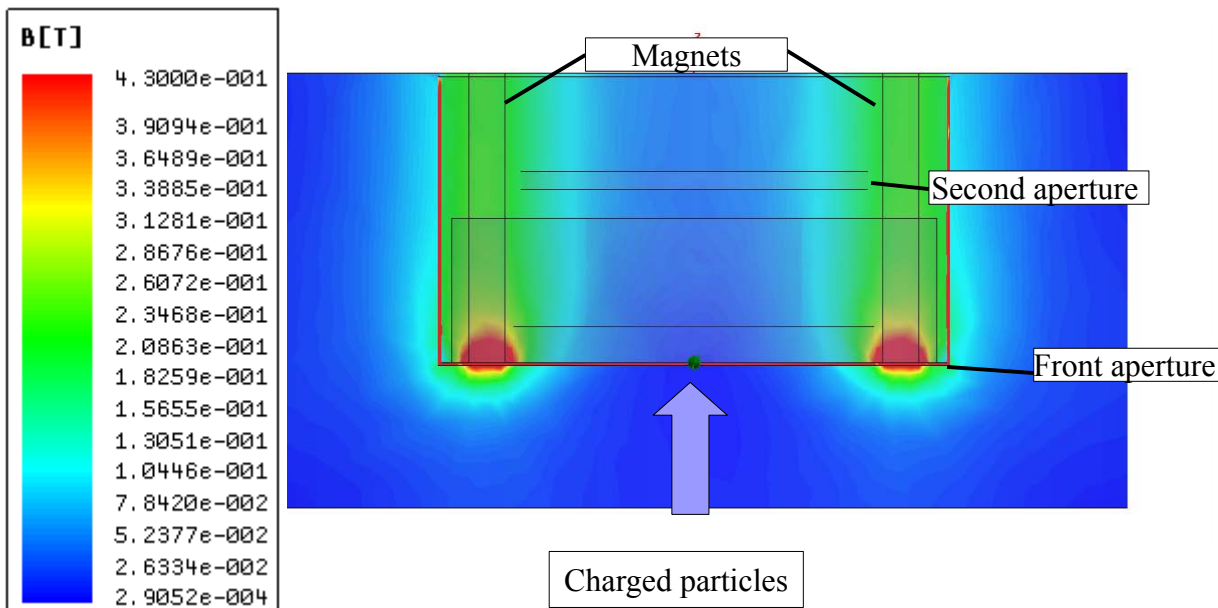


Figure V-10: Maxwell-3D™ magnetostatics model of two K&J Magnetics BX082SH magnets held 3.3 cm apart with the magnetic scale truncated above 3400 Gauss to show that energetic negative ions will penetrate to the collection aperture.

The UW-IEC Faraday cup was designed using the Maxwell-3D™ simulations as a starting point, constraining the location of the magnets and the distance for the deflection region, and requiring the relevant elements to fit between the magnets. The system also had to be optimized for ease of construction and cost. The Faraday cup components had to be constructed on the available facilities at the UW COE Student Shop, and it was determined that a cylindrical form would be easiest to construct, utilizing an engine lathe in machining. The collection electrode had to be shrouded from currents in the source plasma, and this shroud could also be used to hold the magnets in place.

The front aperture defines the collection area; a second electrode in front of the collection electrode defines the 1.5 cm bending region. If the second aperture is electrically isolated it can be biased negative to act as a secondary electron suppression electrode. A secondary electron suppression electrode is superfluous in the presence of the strong magnetic field. If the magnets were to be removed and the case were to be biased more positive than the plasma potential, the Faraday cup would collect negative ions and fast electrons. The difference in collected current with and without the magnets will yield a measurement of the energetic electron profile.

The metal elements are constructed out of aluminum for its ease of machining and low cost. The diagram of the Faraday cup design is shown in

fig. V-11 All parts were machined on a lathe and mill from a 4.445 cm diameter piece of aluminum stock. These are the front case, rear case, secondary electron suppression electrode, and the collection electrode. The collection electrode has a 1.9 cm interior diameter and is over 1.9 cm deep. The secondary suppression electrode has an aperture roughly 1.27 cm diameter. The front shroud has a 1.5 cm passage as part of the bending region. The front aperture controls the area the Faraday cup collects; it was produced out of a 0.005 cm thick piece of Mu-metal, with an aperture of 1.128 cm diameter, so the measurement is the sum of a 1 cm^2 area. The conducting components are isolated by three insulating elements constructed from a ceramic tube with a 3.175 cm outer diameter and a 2.54 cm inner diameter, cut into 0.635 cm long sections using a diamond saw. The outside of the Faraday cup is wrapped in a Mu-metal shield to reduce stray magnetic fields around the Faraday cup and this is clamped down to hold the magnets in place. The elements within the Faraday cup are sandwiched together in a stack between the front and rear case, which are held by three nuts and bolts 120° apart. The overall length of the Faraday cup is roughly 7 cm. The assembled Faraday cup is shown in fig. V-12.

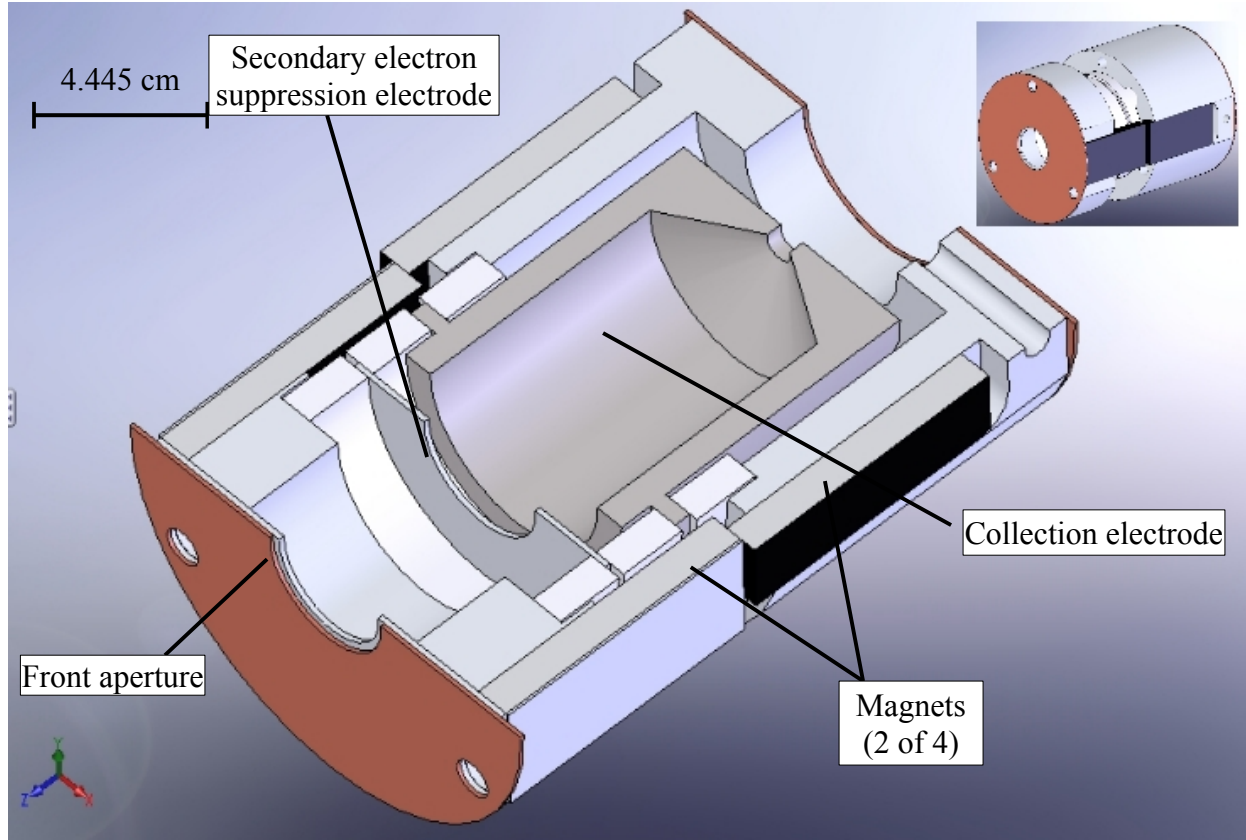


Figure V-11: Isometric through-cut diagram of the Faraday cup showing magnets (black), front aperture, front case, ceramic spacer, secondary electron suppression electrode, ceramic spacer, collection electrode, ceramic spacer; and rear case. The rear hole is for mounting, with a set screw hole shown. Inset is a diagram of the assembled Faraday cup, without the shroud.



Figure V-12: Assembled Faraday cup, without magnets or shroud.

The charged particle current collected by the Faraday cup collection electrode is connected by co-axial cable to a SRS-570 low noise current amplifier. This amplifier produces the least noise when running on battery. The amplifier has variable amplification, and selectable low and high pass filtering. The low pass filtering was used to reduce the noise in the Faraday cup signal. The output of the amplifier was fed into an Tektronix®-TDS 2014 oscilloscope, which was able to provide the average signal, which was used as the negative ion current reading. This does not lend itself to the collection of statistics necessary to calculate significant error, but the variation in the average measurement can be given as a proxy for this value.

V.4.4 Faraday Cup Mounting in an IEC Device

The measurement of the negative ion current profiles in the IEC device requires mounting the Faraday cup on motion feed-throughs. Two

profiles were pursued: radial (requiring linear motion) and azimuthal (requiring rotational motion).

The radial profile was obtained using a linear motion vacuum feed-through, pictured in fig. V-13, that provided a sliding seal to a 2.54 cm (1 inch) tube via three o-rings. The atmosphere end of the feed-through tube was sealed by a Swagelok® fitting sealing to the 2.54 cm tube and a ceramic electrical feed-through that connected the collection electrode to the amplifier and biasing power supplies to the secondary electron suppression aperture and the case of the Faraday cup. The case was electrically shielded from the 2.54 cm tube by a ceramic break that was glued into place with Torr Seal® vacuum epoxy. The radial feed-through system could retract the front aperture of the Faraday cup as far as 11 cm from the wall of the chamber (34 cm from the center of the chamber), and could protrude 19 cm into the HOMER chamber (26 cm from the center of the chamber). The design could accommodate a radial feed-through with a larger range of motion, but the feed-through sliding tube length was constrained due to proximity to other experiments in the UW-IEC laboratory.



The azimuthal profile requires rotational motion that pivots about the center of the HOMER chamber. At the center of the top plate of the HOMER chamber is the high voltage feed-through that supplies power to the IEC device cathode through a stalk. The center bottom of the HOMER chamber is the port where a turbo vacuum pump is connected. This port is shielded from debris by a plate roughly 2 cm off the bottom of the chamber; it was decided to mount the central rotational pivot to this plate via a bearing and drive the rotational motion with a rotational feed-through installed on another port on the bottom of the HOMER chamber. After some experimentation the azimuthal scan was carried out by connecting the rotational feed-through and the central rotational pivot via a chain and

gears, as pictured in fig. V-14. The Faraday cup supports had to be cantilevered and counterbalanced for the bearing of the central rotational pivot to travel smoothly.

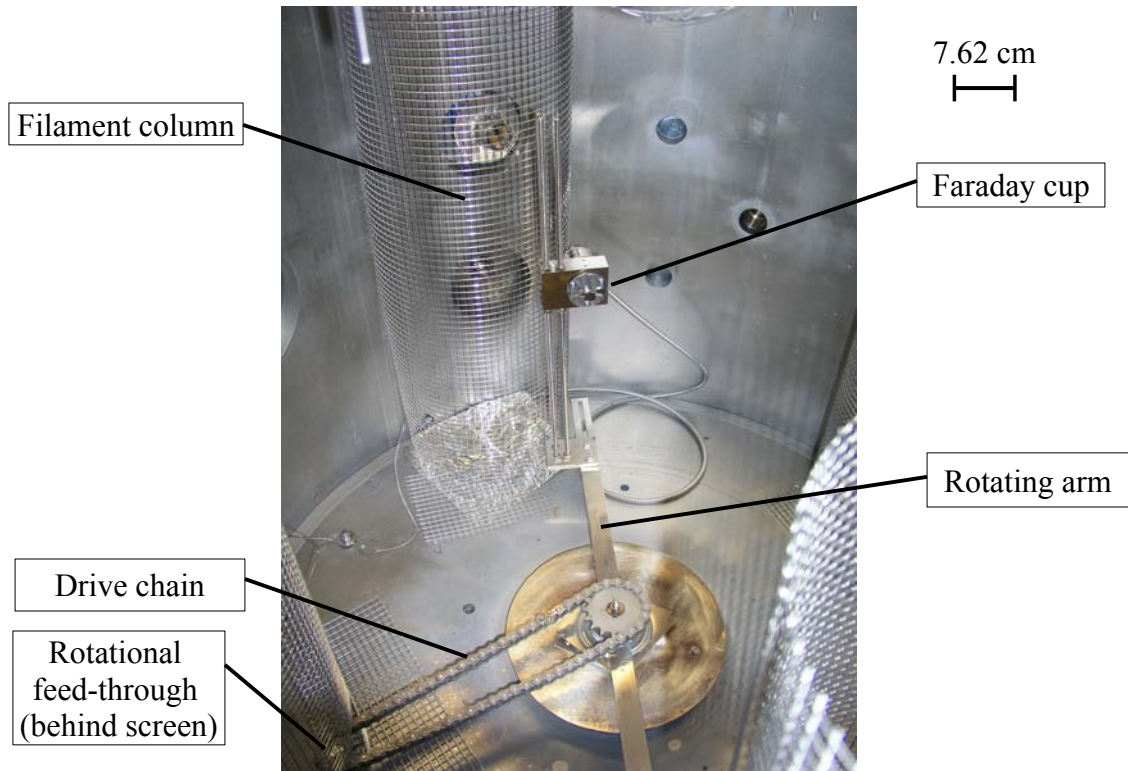


Figure V-14: Picture of azimuthal scan system. The Faraday cup mounting pivots on a bearing in the center of the chamber. This bearing is connected by chain to a rotational feed-through (behind the mesh on the bottom left hand corner of the picture). The Faraday cup and mounting is counterbalanced by stainless steel weights (off frame on the bottom of the picture). The range of motion of the azimuthal scanning system is limited by the grids that shield the filaments.

Reliability of positioning required some system of verification. The initial concept relied only on the degree indicator on the rotational feed-through to determine the movement of the Faraday cup, however backlash in the chain and slippage in one of the set pins that secured the rotating arm to the central gear introduced significant uncertainty in positioning.

The set pin slippage was particularly difficult, as this slippage was not present initially and all early data, where the position was unverified, had to be discarded due to the uncertainty in position of the Faraday cup.

Measurement indicates that the Faraday cup has roughly 52.5 degrees of motion between the two filament shield cages. This was verified by the degree indicator of the rotational feed-through once the set pin slippage was redressed. A diagram of the Faraday cup field of view is shown in fig. V-15:

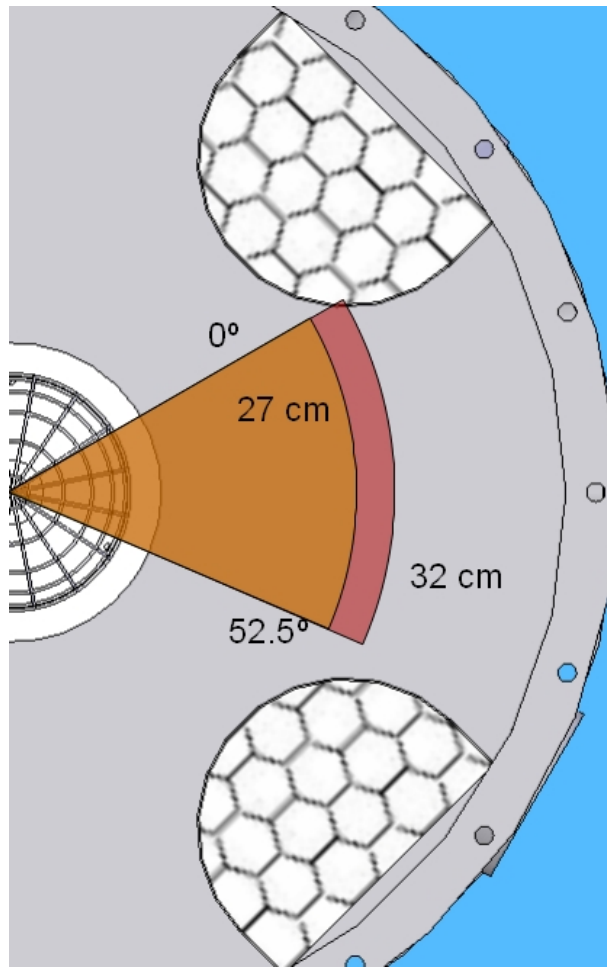


Figure V-15: Illustration of field of view of azimuthal Faraday cup scanning mount. Shown is 20 cm diameter cathode grid to illustrate that two jets and part of a third are in the azimuthal mount's field of view.

To eliminate the positioning uncertainty from backlash in the chain and slippage in the set screw, a series of reference photos was taken in 5 degree increments, using the camera that provides a live visual monitor of the interior of the IEC device while under operation. These images were cropped to show the position of the Faraday cup and a variety of reference points so the image could be overlaid with the live image to show that the Faraday cup was reliably in the desired position. These cropped images

have also been assembled in a collage to show the Faraday cup positioning is largely evenly spaced by showing when the pictures are aligned the positions of the Faraday cup fall along a straight line, as in fig. V-16:

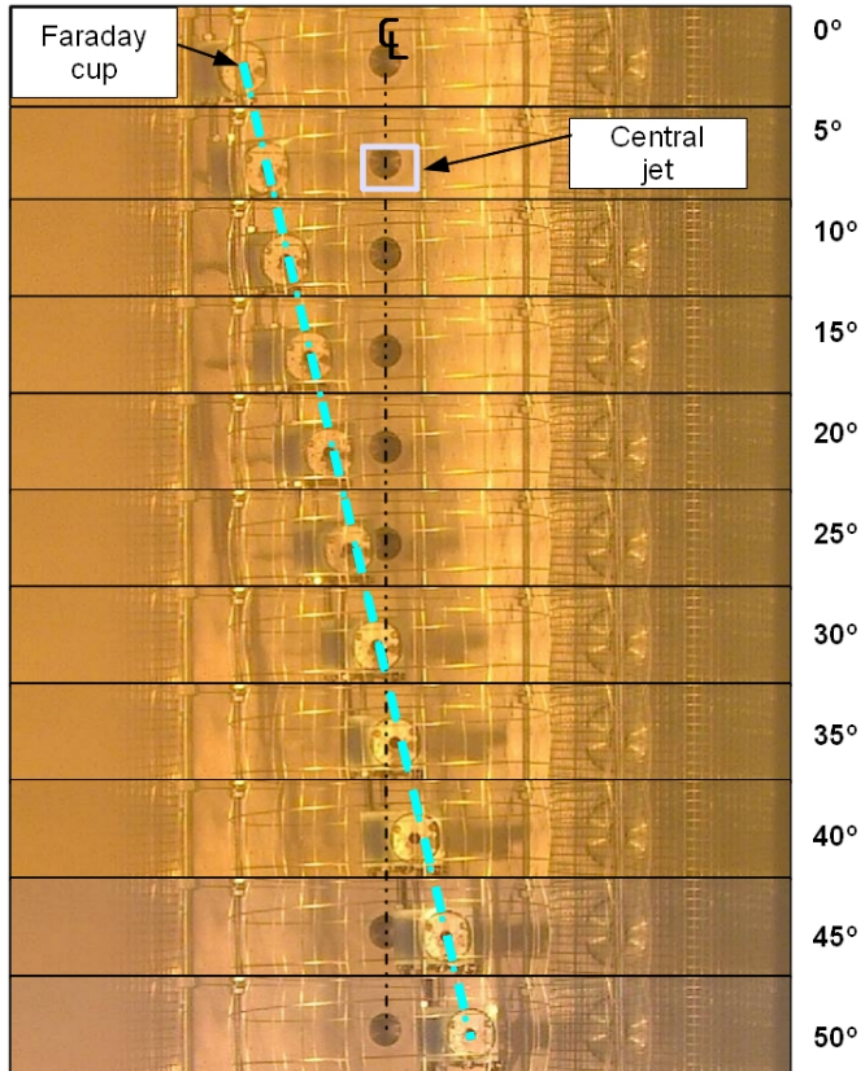


Figure V-16: Collage of Faraday cup positioning reference pictures. The vertical black line shows the center of the central jet in the field of view of the Faraday cup. The blue line shows the positioning of the Faraday cup is evenly spaced, as the apertures mostly conform to a straight line.

- [V-1]D.R. Boris and G.A. Emmert, "Composition of the source region plasma in inertial electrostatic confinement devices,"*Physics of Plasmas* 15 pp. 083502 (2008).
- [V-2]D. C. Donovan, "Spatial Profiling Using a Time of Flight Diagnostic and Applications of Deuterium-Deuterium Fusion in Inertial Electrostatic Confinement Fusion Devices," Ph.D. Thesis, University of Wisconsin - Madison, 2011.
- [V-3] R. F. Radel, "Detection of highly enriched uranium and tungsten surface damage studies using a pulsed inertial electrostatic confinement fusion device," Ph.D. Thesis, University of Wisconsin - Madison, 2007.
- [V-4]Private communication with Dr. G. R. Piefer, March 2010
- [V-5]ANYSIS Maxwell, ANSYS, INC. 2011 www.ansys.com Jun. 2012
- [V-6] D. Boris, "Novel Diagnostic Approaches to Characterizing the Performance of the Wisconsin Intertial Electrostatic Confinement Plasma," Ph.D. Thesis, University of Wisconsin - Madison, 2009.
- [V-7] D. Boris et al., "Deuterium anions in inertial electrostatic confinement devices," *Physical Review E*, vol. 80, no. 3, p. 036408, 2009.
- [V-8] G. H. Miley, H. Momota, and R. A. Stubbers, "A Novel Electric Thruster Based on IEC Plasma Jet Technology," in *ICAPP'04: 2004 international congress on advances in nuclear power plants*, 2004.
- [V-9] J. Khachan and S. Collis, "Measurements of ion energy distributions by Doppler shift spectroscopy in an inertial-electrostatic confinement device," *Physics of Plasmas*, vol. 8, no. 4, pp. 1299-1304, Apr. 2001.
- [V-10]S. K. Murali, J. F. Santarius, and G. L. Kulcinski, "Effects of the Cathode Grid Wires on Fusion Proton Measurements in Inertial-Electrostatic Confinement Devices," *IEEE Transactions on Plasma Science*, vol. 39, no. 2, pp. 749-755, Feb. 2011.
- [V-11]H. Zhang, *Ion Sources*. Springer-Verlag, 1999.

VI: Results

This Chapter begins with an example of results from the VICTER negative ion subroutine and some predictions of negative ion physics in an IEC device. Next, results from the Faraday cup will be discussed, beginning with radial profiles and concluding with azimuthal profiles. Chapter VII will compare computational and experimental results, and draw conclusions from these results.

VI.1: VICTER negative ion results

The output of the VICTER negative ion subroutine is a matrix of current densities, binned by total energy and radius. A post-processing routine is used to convert total energy into kinetic energy, moving the energy bins the requisite amount to subtract the specified radial potential energy energy from the output. An example of the post-processed results for the outward traveling negative ions is shown in fig. VI-1. The energy spectrum predicted by VICTER evolves with radius, but it is easiest to make sense of the energy spectrum at a single radius. The outermost radial bin is closest to what has been measured by the Magnetic Deflection Energy Analyzer (MDEA) and is shown in fig. VI-2:

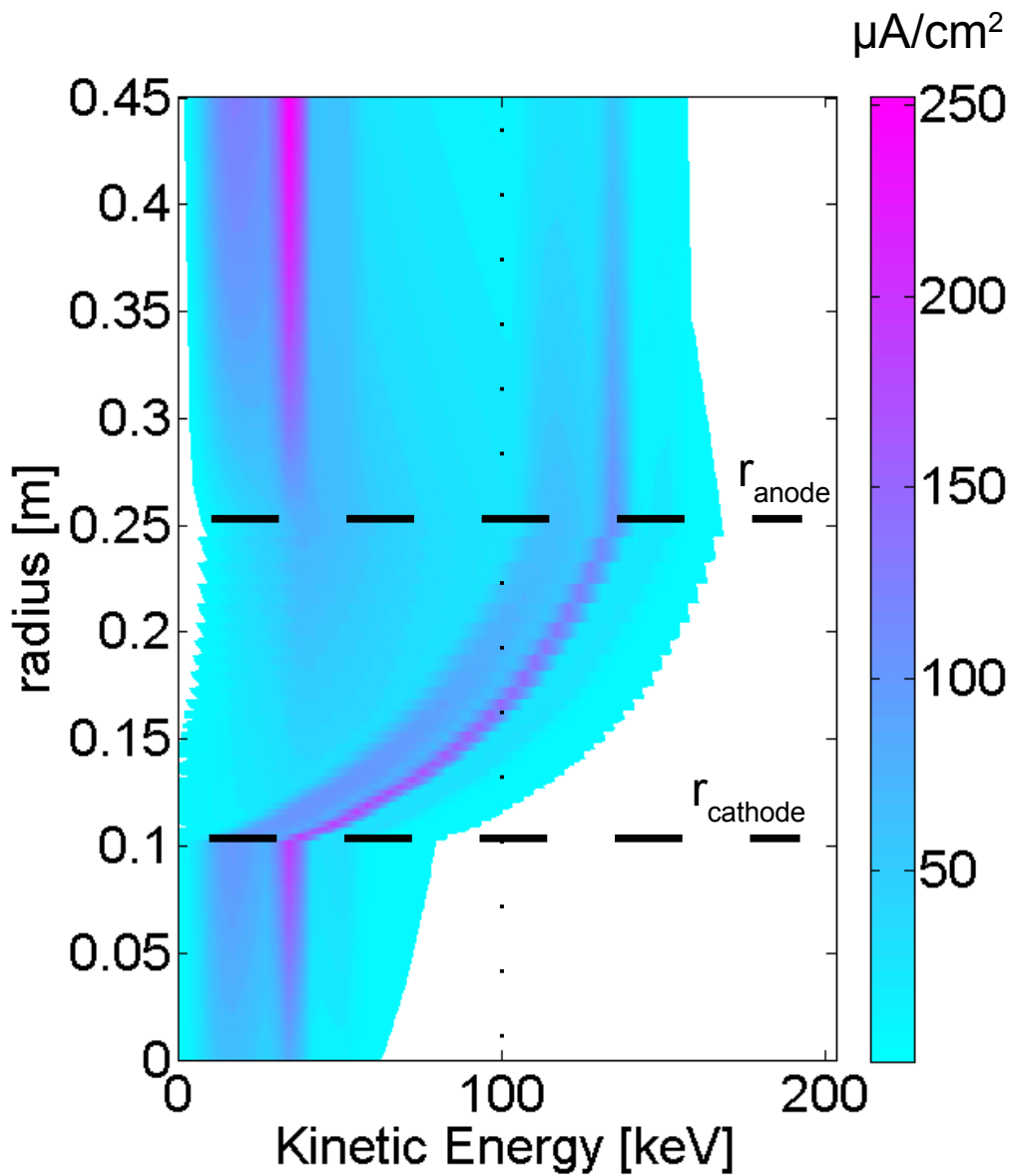


Figure VI-1: Typical negative ion results from the VICTER negative ion subroutine. This example is for a 20 cm diameter cathode and a 50 cm diameter anode with -100 kV potential applied to the cathode and 30 mA meter current supplied to the cathode, with a 2 mTorr background gas pressure. The vertical dotted line shows the cathode potential, and the horizontal dashed lines show the radii of the electrodes.

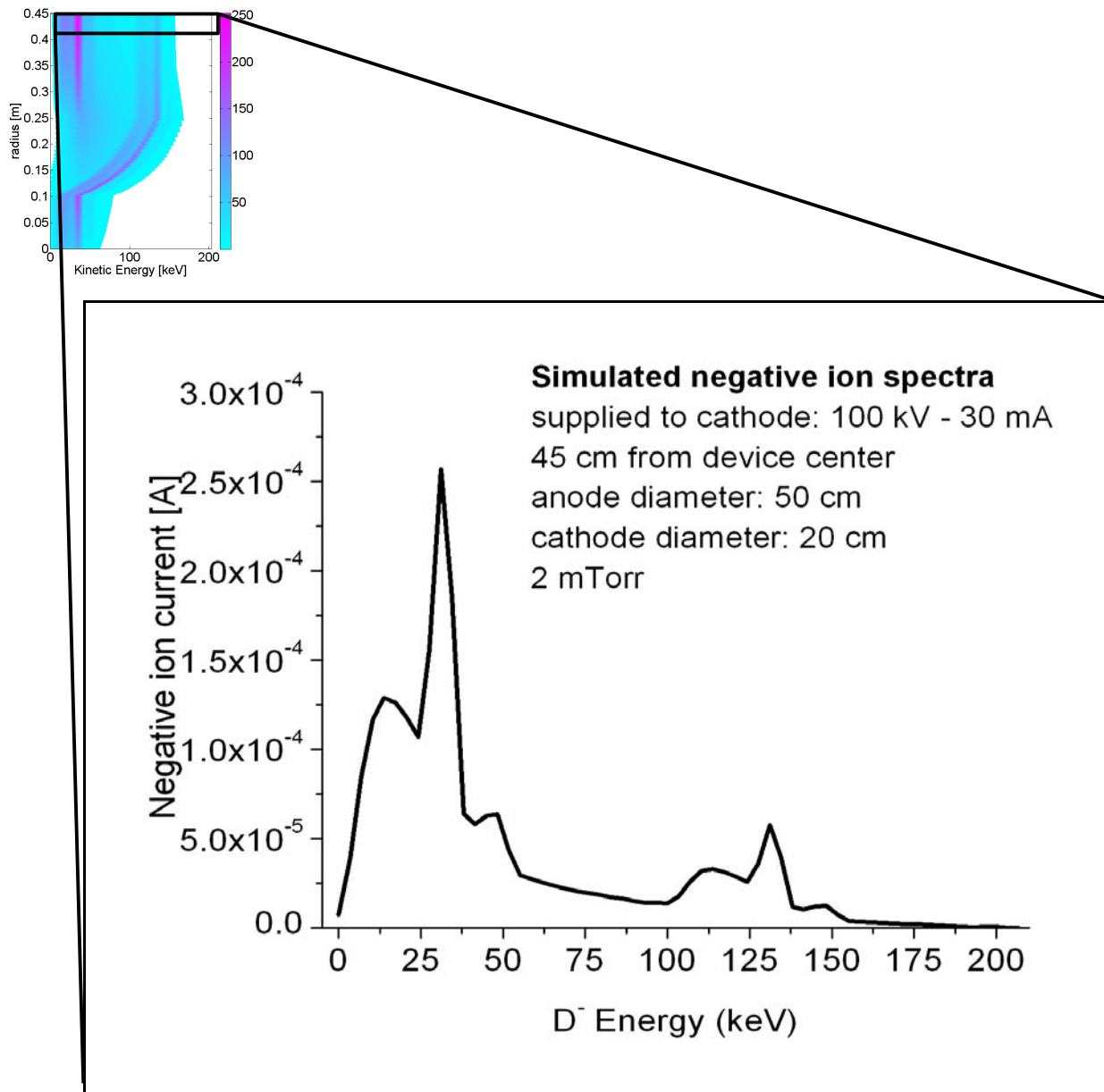


Figure VI-2: VICTER simulation of the negative ion energy spectrum at 45 cm from center of an IEC device with a 20 cm diameter cathode, 50 cm diameter anode with a -100 kV potential applied to the cathode and 30 mA of meter current supplied to the cathode, with a 2 mTorr background pressure.

VICTER predicts some negative ions have a kinetic energy larger than the potential of the cathode. This is possible because negative ions can undergo a tandem accelerator like effect, where a fast neutral is created traveling inward, this passes through the cathode, and produces a negative ion traveling outward. The negative ion then gains the energy from the potential it was born at plus the kinetic energy it was born with. This is why some fraction of the negative ion population is the most energetic population in the IEC device.

Comparing this predicted negative ion spectrum to the spectrum measured at the same conditions by the MDEA in fig. II-14 shows the VICTER simulation predi negative ions of a higher energy than the MDEA diagnostic measured. This is because at the time the MDEA measurements were taken this tandem accelerator like effect on the negative ions was not recognized and the magnetic field was not raised to a high enough level to observe negative ions beyond 100 keV. That said, we can compare the simulated spectrum below 100 kV with the MDEA results. This comparison will be carried out in Chapter VII.

It has been hypothesized [VI-1,2] that the structure of the energy spectrum, which fits a sum of 5 Gaussian curves as illustrated in fig. II-14, yields information about the negative ion origins. When a negative ion is born from charge exchange it carries its mass fraction of its parent's momentum, so it is inferred that three of the Gaussian peaks correlate to

the mass of the charge exchange parent species (i.e. D^+ and fast D , D_2^+ and fast D_2 , and D_3^+); one Gaussian correlates to negative ions born from electron attachment inside the cathode; one Gaussian correlates to metastable molecular negative ions created inside the cathode. While VICTER presently does not simulate molecular negative ions or electron attachment, it can be used to isolate each parent species of the negative ions from charge exchange to determine how theory compares to this hypothesis; the results of this VICTER simulation are shown in fig. VI-3.

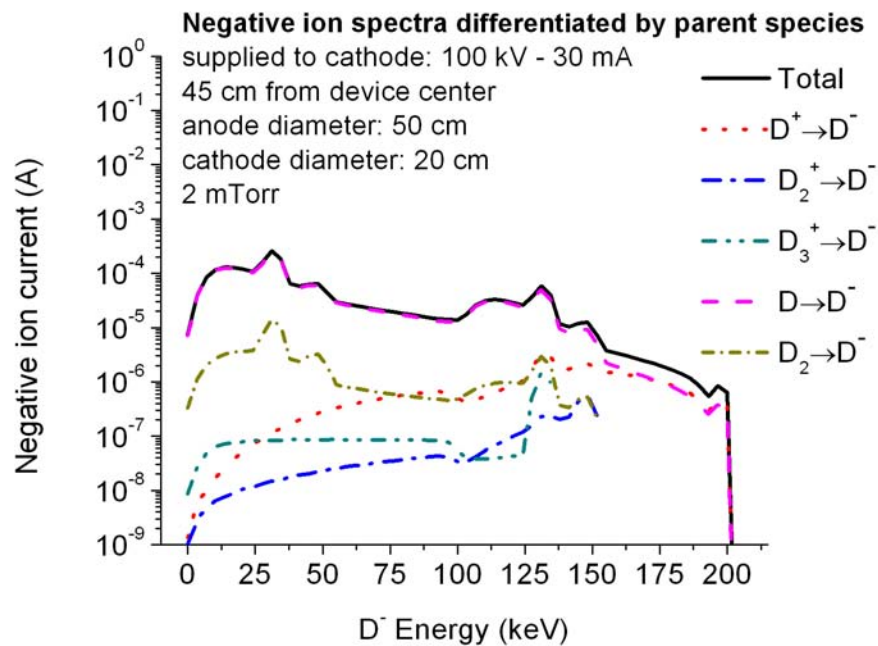


Figure VI-3: VICTER simulation with the same parameters as fig. VI-2, but with each parent isolated. The y-axis is shown in log scale so the parent species curves are distinguishable. This analysis predicts that nearly all negative ions produced in the IEC device from charge exchange and disassociation reactions are produced by reactions of fast neutrals.

Isolating the negative ions by parent species clearly shows the majority of negative ions are produced from an atomic fast neutral parent. This does not necessarily conflict with the hypothesis that the spectrum yields information about the negative ion's derivation. Because the fast neutrals are not accelerated by the electric potential preserving energy information of the fast neutral's parent, it may be that the Gaussian curves of the negative ion spectra correlate to the parent of the fast neutrals that produce the vast majority of negative ions. This hypothesis can also be tested by the VICTER code, the results of which are shown in fig. VI- 4.

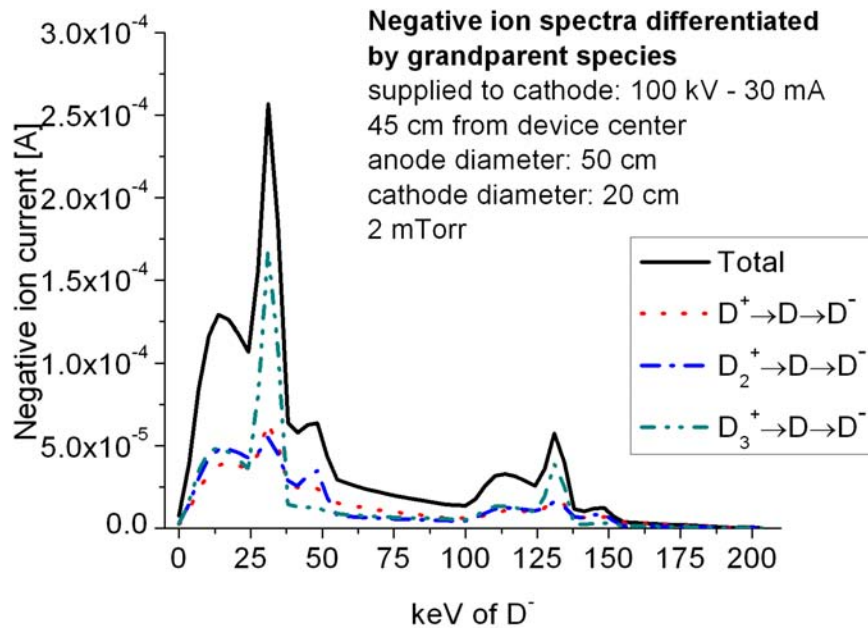


Figure VI-4: VICTER simulation of negative ion spectra under the same conditions as in fig. VI-3. The total spectrum is shown and divided into spectra of negative ions segregated by grandparent ion species that produce a fast neutral that produces the final negative ion.

This simulation indicates that the negative ion spectrum arises from physics more complicated than a simple correlation between Gaussian curves and parent or even grandparent species.

The VICTER negative ion subroutine results can be used to produce plots of radial change in negative ion current. The VICTER negative ion subroutine can also predict the negative ion current response to potential on the cathode, current supplied to the cathode, and background pressure. The results of VICTER negative ion subroutine parametric studies and how they compare to Faraday cup parametric studies will be explored in Chapter VII.

VI.2: Faraday cup measurements

Faraday cup measurements of the negative ions in the HOMER IEC device are grouped into two separate types of profile: radial and azimuthal. Each yields different information about physics in HOMER.

VI.2.1: Faraday cup radial measurements

Radial profile measurements were taken in two different anode-cathode configurations: 20 cm diameter cathode – 50 cm diameter anode and 20 cm diameter cathode – 30 cm diameter anode. These radial measurements were taken aligned with a cathode jet or aligned (as accurately as visual inspection allows) with a cathode wire. All radial

measurements were taken at 2 mTorr.

Rigorously determining the significant error in the Faraday cup measurement will require an improved data acquisition system, as discussed in section V.4.3. As a proxy for error, the range of variation in the average negative ion current measurement will be reported. For the radial measurements in this section the variation was $\pm 0.4 \mu\text{A}$ from the reported negative ion current.

Parametric scans of voltage and current were carried out for radial Faraday cup profile measurements, the results of which are shown below. The 50 cm diameter anode – 20 cm diameter cathode parametric measurements aligned with a cathode jet are shown in fig VI-5. This data can be recast to show more explicitly the change in negative ion current with radius, comparing constant voltage or constant current, as shown in figures VI-6-11.

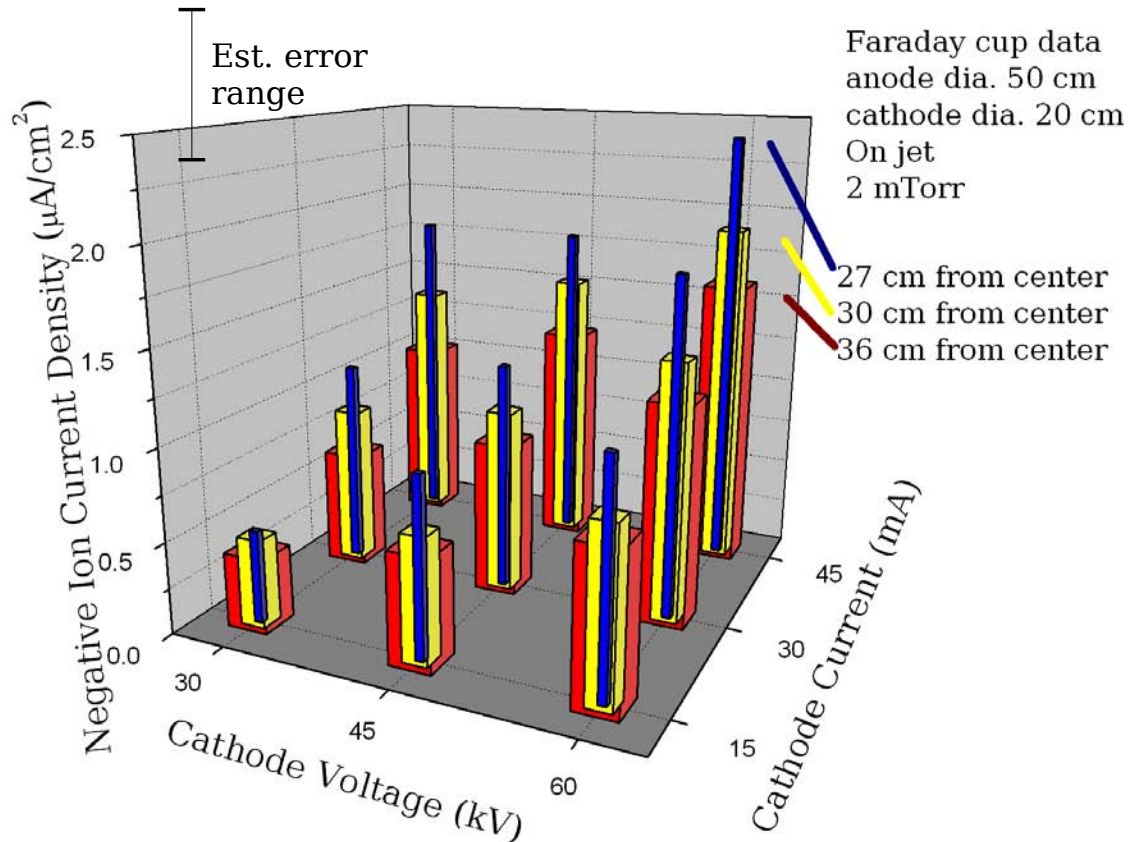


Figure VI-5: Cathode voltage, current, and negative ion measurement radius parametric scan in an IEC device aligned with an IEC plasma jet produced by a 50 cm diameter anode and 20 cm diameter cathode at 2 mTorr operating pressure. All measurements were taken from a 1 cm^2 collection area in the diagnostic.

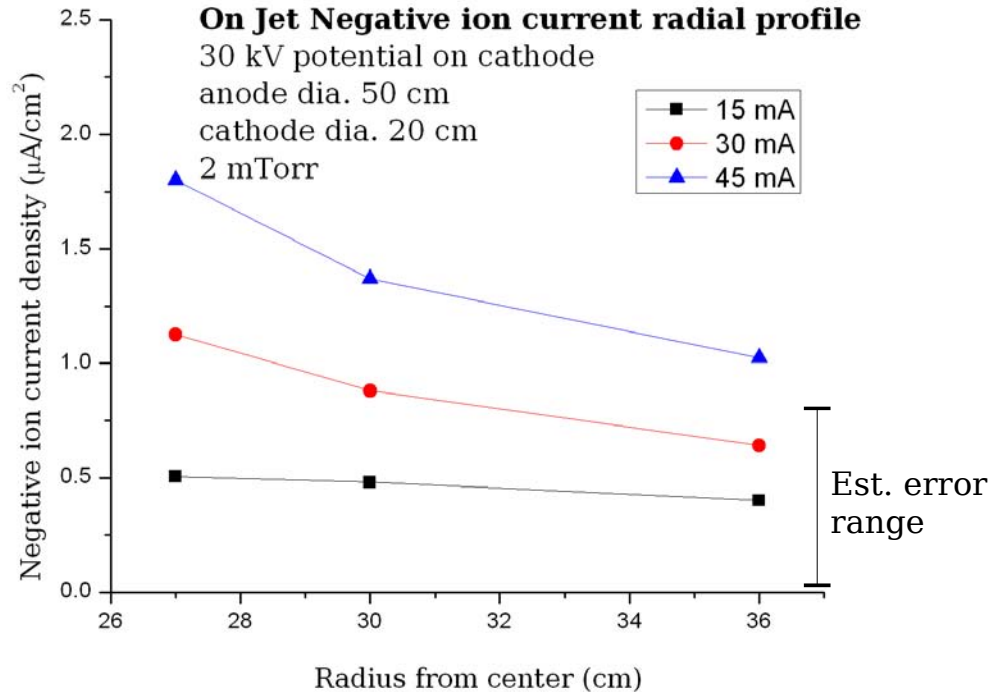


Figure VI-6: Comparison of how Faraday cup measurements of negative ion current changes with radius in an IEC device with a 50 cm diameter anode and 20 cm diameter cathode, aligned with a plasma jet. This plot shows three different negative ion currents, with 30 kV of potential applied to the cathode. This is the same data is shown in fig. VI-5.

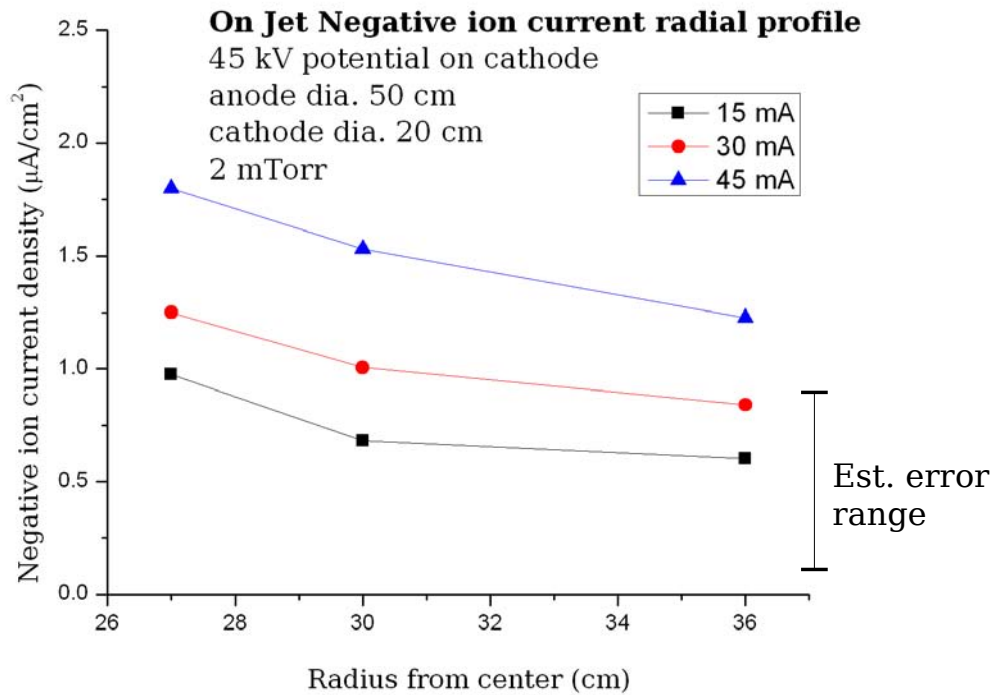


Figure VI-7: Comparison of how Faraday cup measurements of negative ion current changes with radius in an IEC device with a 50 cm diameter anode and 20 cm diameter cathode, aligned with a plasma jet. This plot shows three different negative ion currents, with 45 kV of potential applied to the cathode. This is the same data is shown in fig. VI-5.

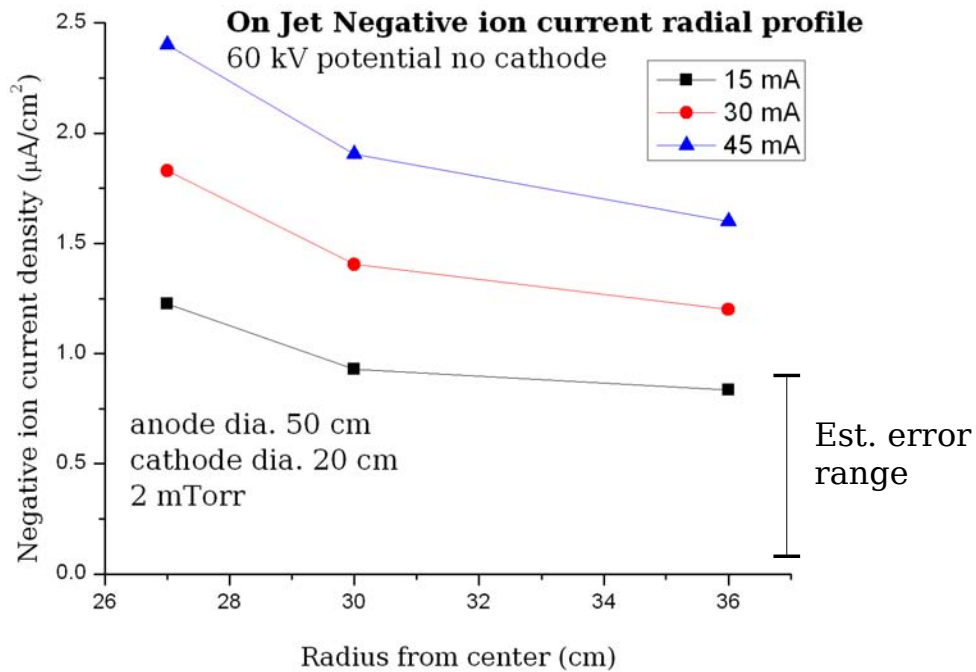


Figure VI-8: Comparison of how Faraday cup measurements of negative ion current changes with radius in an IEC device with a 50 cm diameter anode and 20 cm diameter cathode, aligned with a plasma jet. This plot shows three different negative ion currents, with 60 kV of potential applied to the cathode. This is the same data is shown in fig. VI-5.

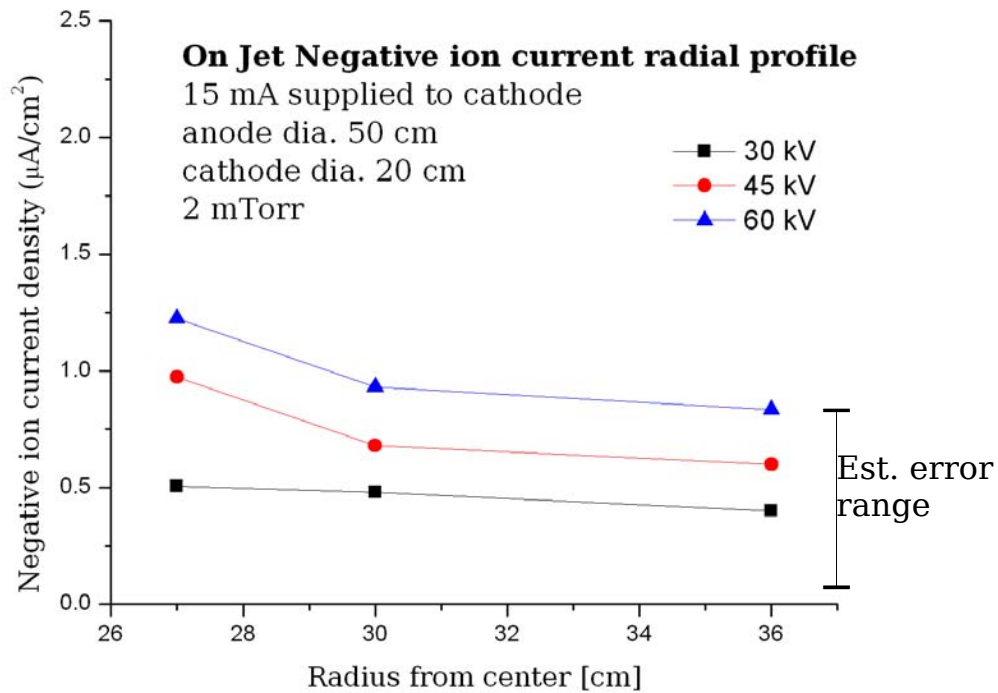


Figure VI-9: Comparison of how Faraday cup measurements of negative ion current changes with radius in an IEC device with a 50 cm diameter anode and 20 cm diameter cathode, aligned with a plasma jet. This plot shows three different negative ion currents, with 15 mA of meter current supplied to the cathode. This is the same data is shown in fig. VI-5.

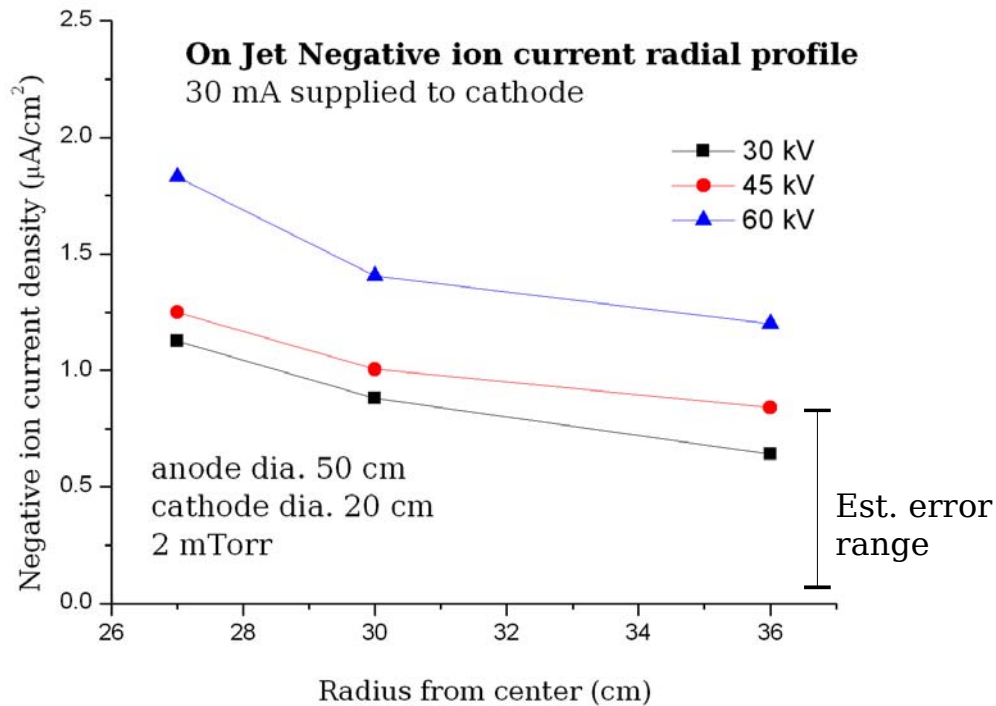


Figure VI-10: Comparison of how Faraday cup measurements of negative ion current changes with radius in an IEC device with a 50 cm diameter anode and 20 cm diameter cathode, aligned with a plasma jet. This plot shows three different negative ion currents, with 30 mA of meter current supplied to the cathode. This is the same data is shown in fig. VI-5.

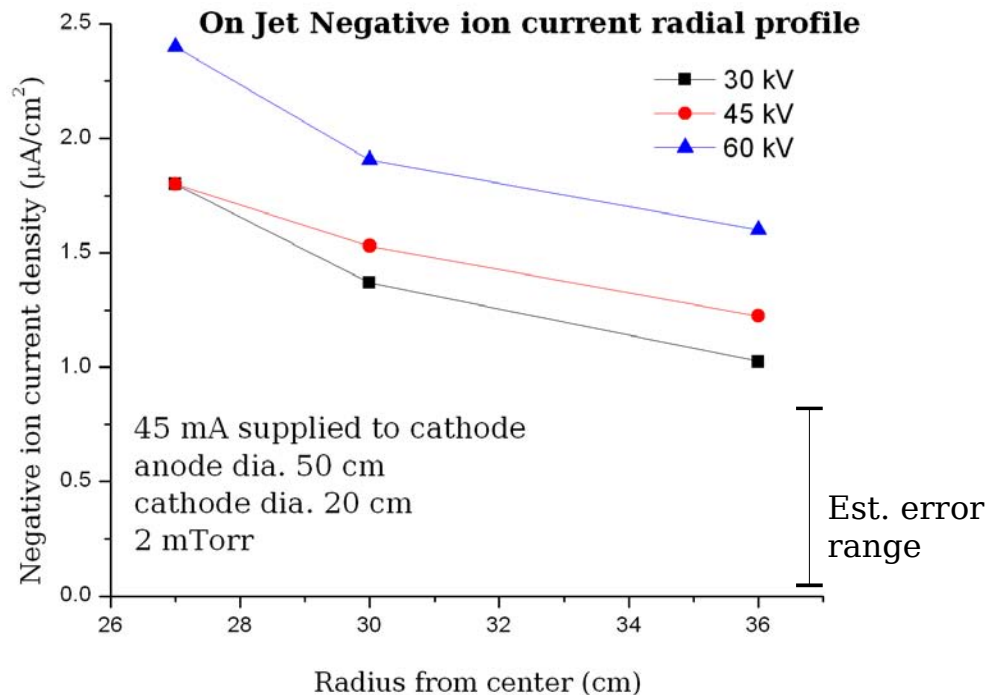


Figure VI-11: Comparison of how Faraday cup measurements of negative ion current changes with radius in an IEC device with a 50 cm diameter anode and 20 cm diameter cathode, aligned with a plasma jet. This plot shows three different negative ion currents, with 45 mA of meter current supplied to the cathode. This is the same data is shown in fig. VI-5.

Similarly, measurements were made in an IEC device with a 50 cm diameter anode and 20 cm diameter cathode, but with the Faraday cup aligned with a cathode grid wire. The results of these measurements are shown in fig. VI-12. This data can be recast to show explicitly the response of negative ion current to radius, comparing constant voltage or constant current, as shown in figures VI-13-18

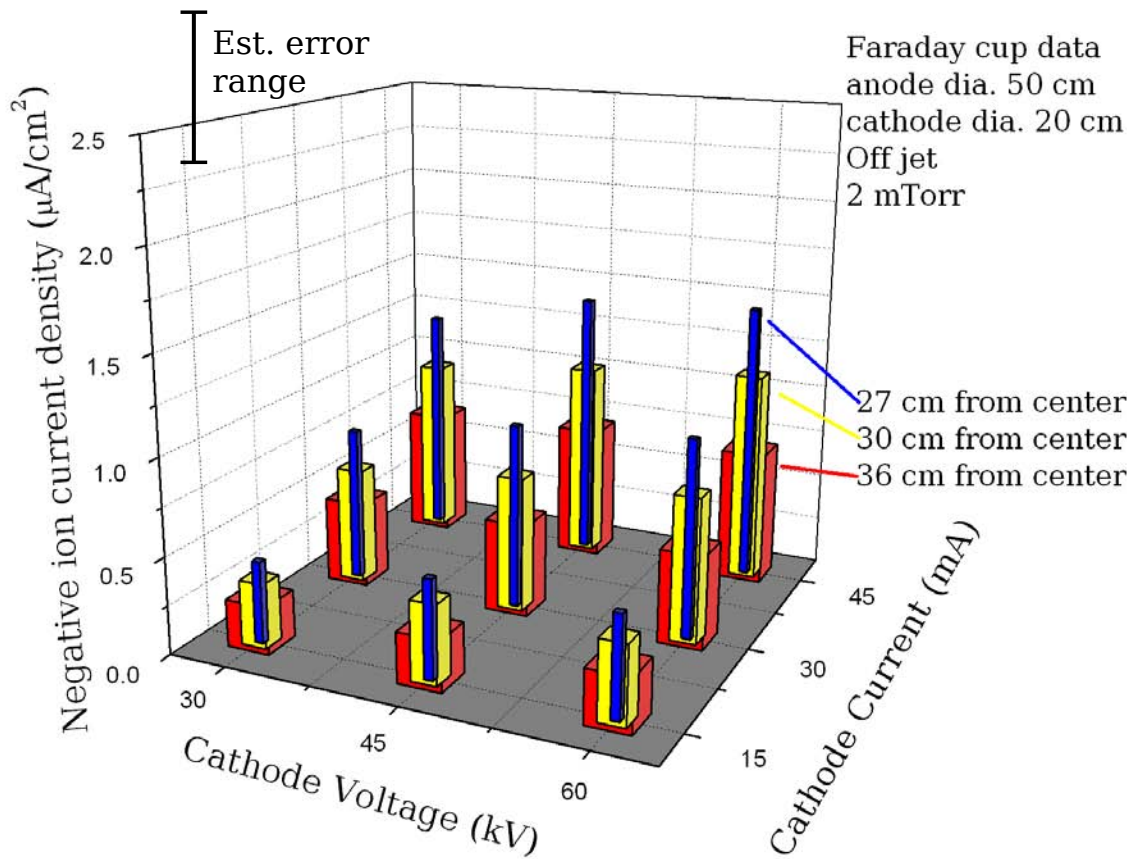


Figure VI-12: Cathode voltage, current, and negative ion measurement radius parametric scan aligned with a cathode grid wire in an IEC device with a 50 cm diameter anode and 20 cm diameter cathode at 2 mTorr operating pressure. All measurements were taken from a 1 cm^2 collection area in the diagnostic.

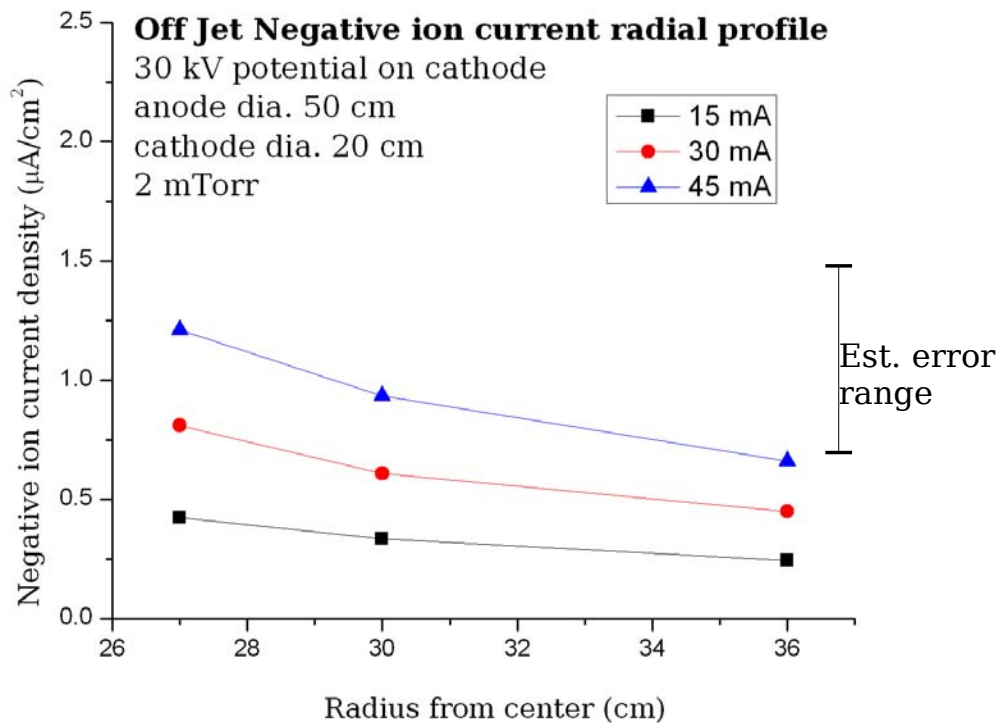


Figure VI-13: Comparison of how Faraday cup measurements of negative ion current changes with radius in an IEC device with a 50 cm diameter anode and 20 cm diameter cathode, aligned with a cathode wire. This plot shows three different negative ion currents, with 30 kV of potential applied to the cathode. This is the same data is shown in fig. VI-12.

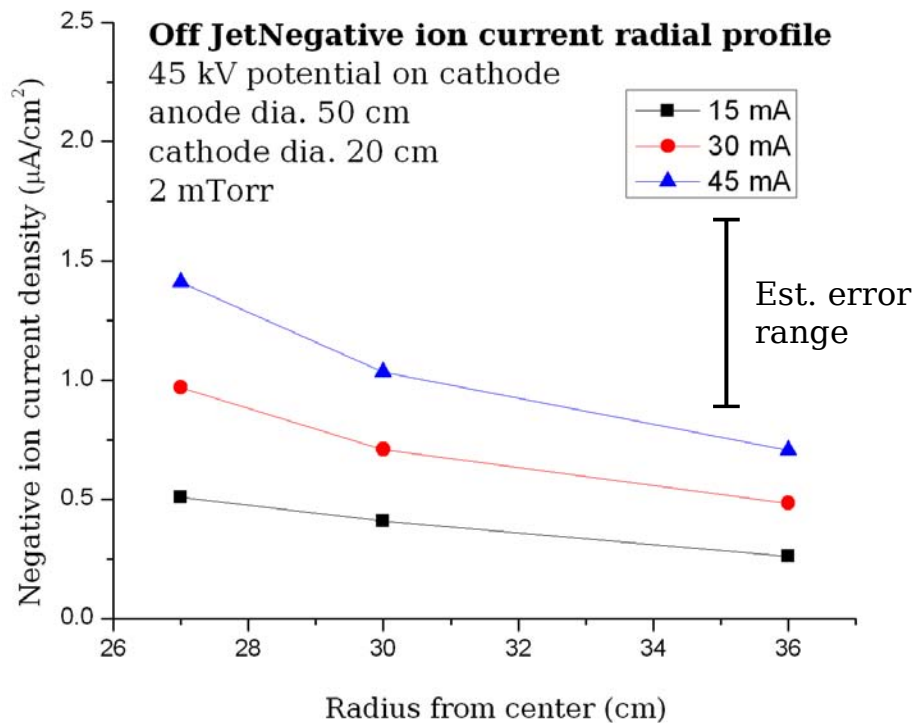


Figure VI-14: Comparison of how Faraday cup measurements of negative ion current changes with radius in an IEC device with a 50 cm diameter anode and 20 cm diameter cathode, aligned with a cathode wire. This plot shows three different negative ion currents, with 45 kV of potential applied to the cathode. This is the same data is shown in fig. VI-12.

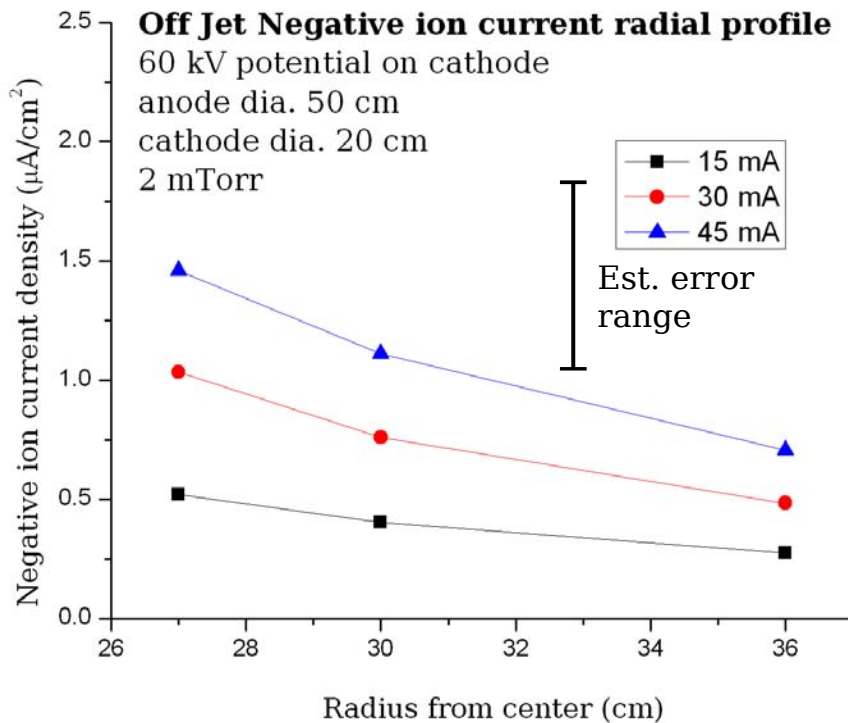


Figure VI-15: Comparison of how Faraday cup measurements of negative ion current changes with radius in an IEC device with a 50 cm diameter anode and 20 cm diameter cathode, aligned with a cathode wire. This plot shows three different negative ion currents, with 60 kV of potential applied to the cathode. This is the same data is shown in fig. VI-12.

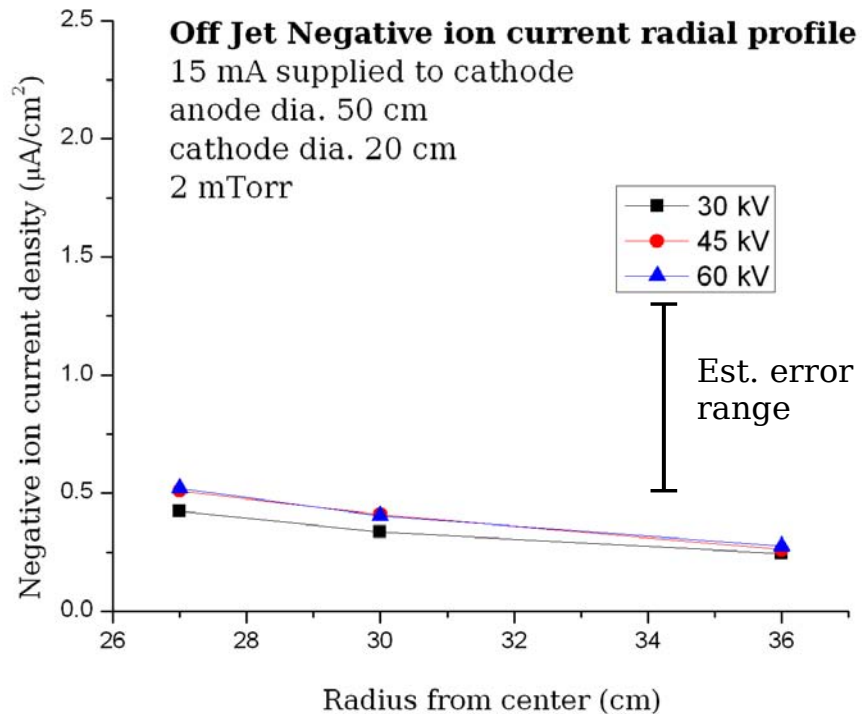


Figure VI-16: Comparison of how Faraday cup measurements of negative ion current changes with radius in an IEC device with a 50 cm diameter anode and 20 cm diameter cathode, aligned with a cathode wire. This plot shows three different negative ion currents, with 15 mA of meter current supplied to the cathode. This is the same data is shown in fig. VI-12.

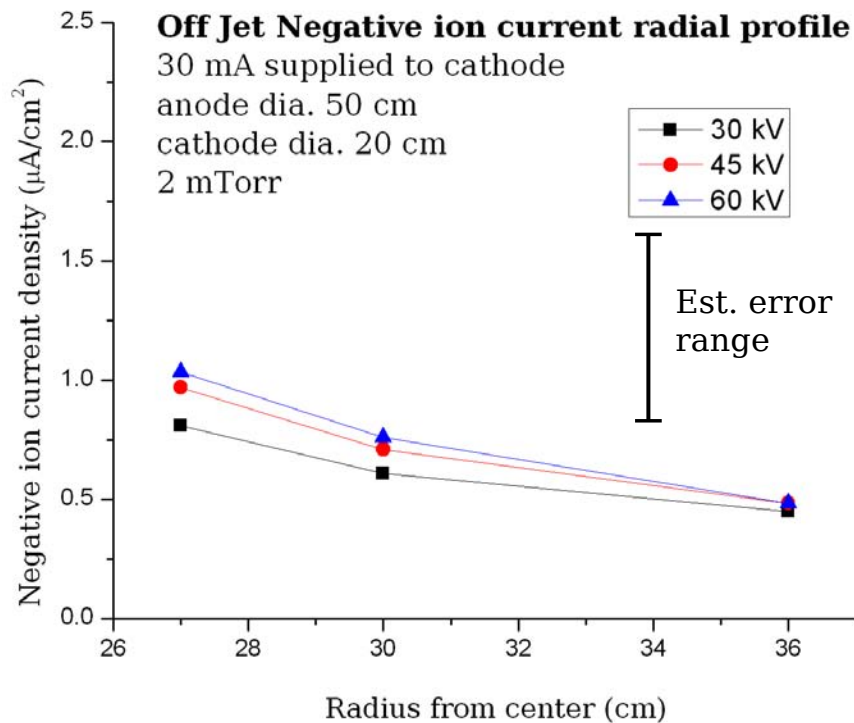


Figure VI-17: Comparison of how Faraday cup measurements of negative ion current changes with radius in an IEC device with a 50 cm diameter anode and 20 cm diameter cathode, aligned with a cathode wire. This plot shows three different negative ion currents, with 30 mA of meter current supplied to the cathode. This is the same data is shown in fig. VI-12.

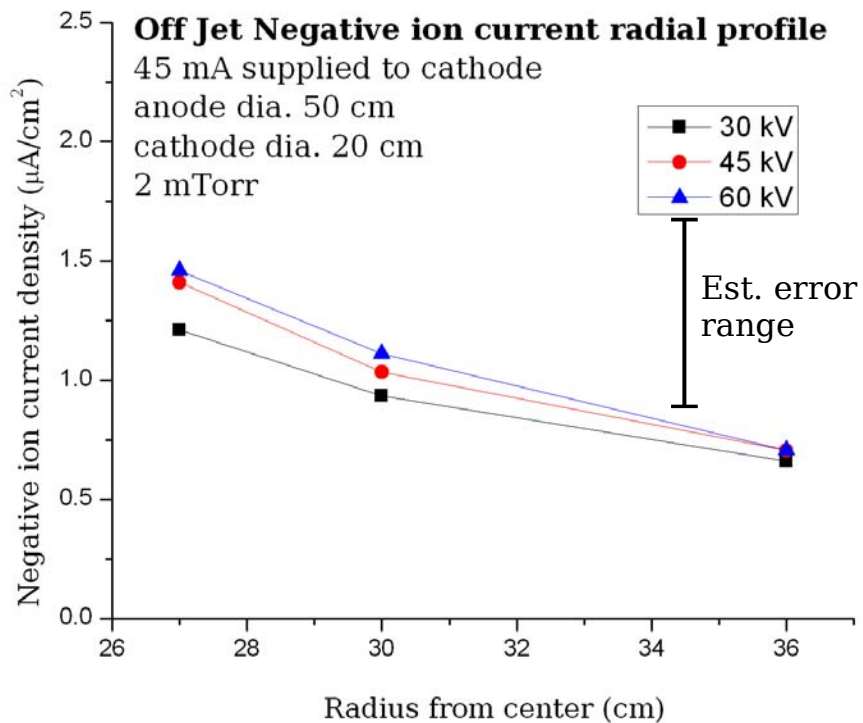


Figure VI-18: Comparison of how Faraday cup measurements of negative ion current changes with radius in an IEC device with a 50 cm diameter anode and 20 cm diameter cathode, aligned with a cathode wire. This plot shows three different negative ion currents, with 45 mA of meter current supplied to the cathode. This is the same data is shown in fig. VI-12.

The last radial parametric scan performed here was using the 30 cm diameter anode and 20 cm diameter cathode, aligned with a cathode jet, as shown in fig. VI-19. This data can be recast to more explicitly show the change in negative ion current with radius, contrasting constant voltage or constant current, as shown in figures VI-20-25

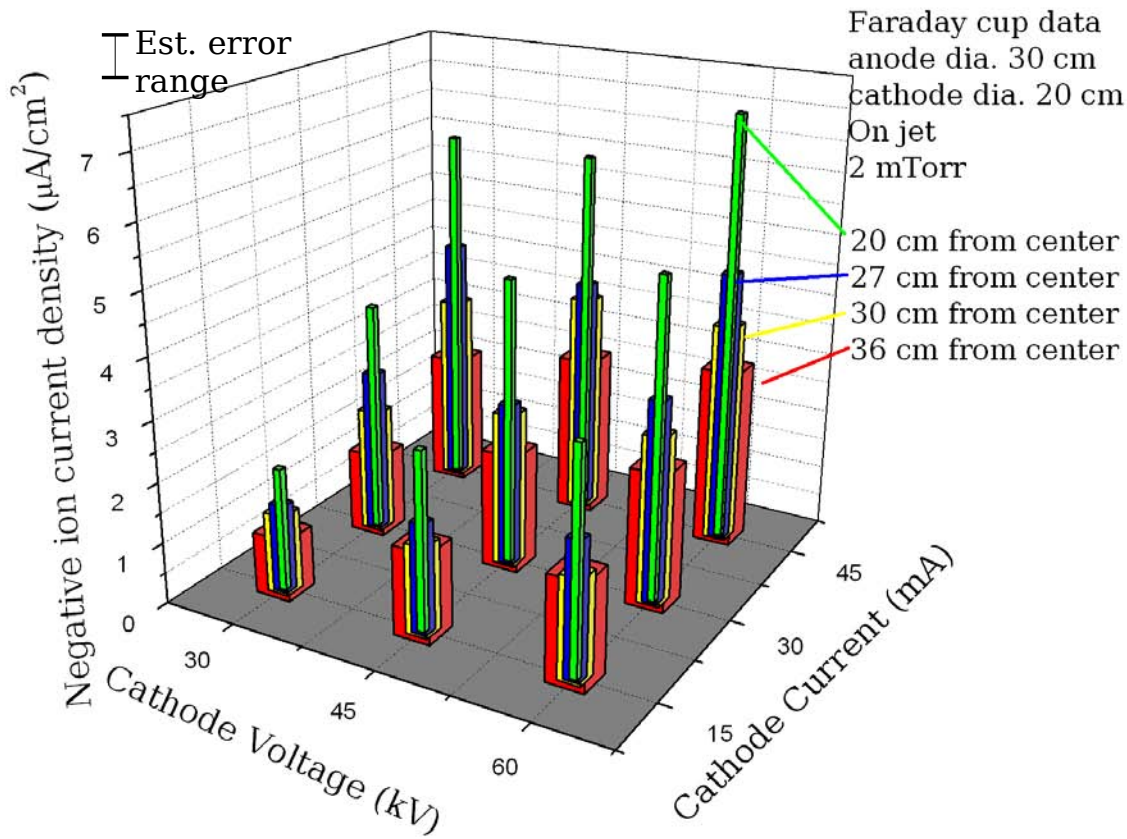


Figure VI-19: Cathode voltage, current, and negative ion measurement radius parametric scan aligned with a plasma jet in an IEC device with a 30 cm diameter anode and 20 cm diameter cathode at 2 mTorr operating pressure. All measurements were taken from a 1 cm^2 collection area in the diagnostic.

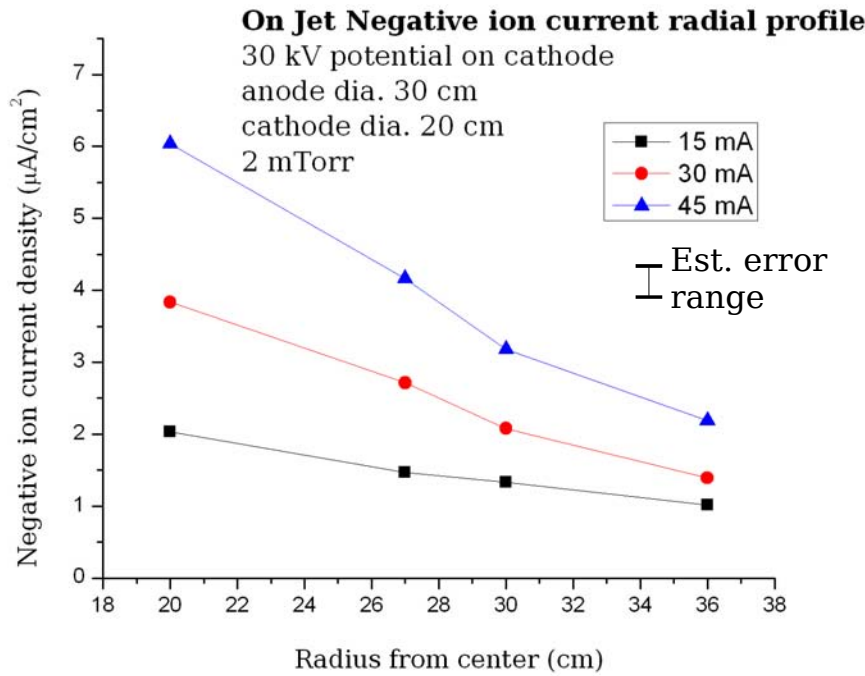


Figure VI-20: Comparison of how Faraday cup measurements of negative ion current changes with radius in an IEC device with a 30 cm diameter anode and 20 cm diameter cathode, aligned with a plasma jet. This plot shows three different negative ion currents, with 30 kV of potential applied to the cathode. This is the same data is shown in fig. VI-19.

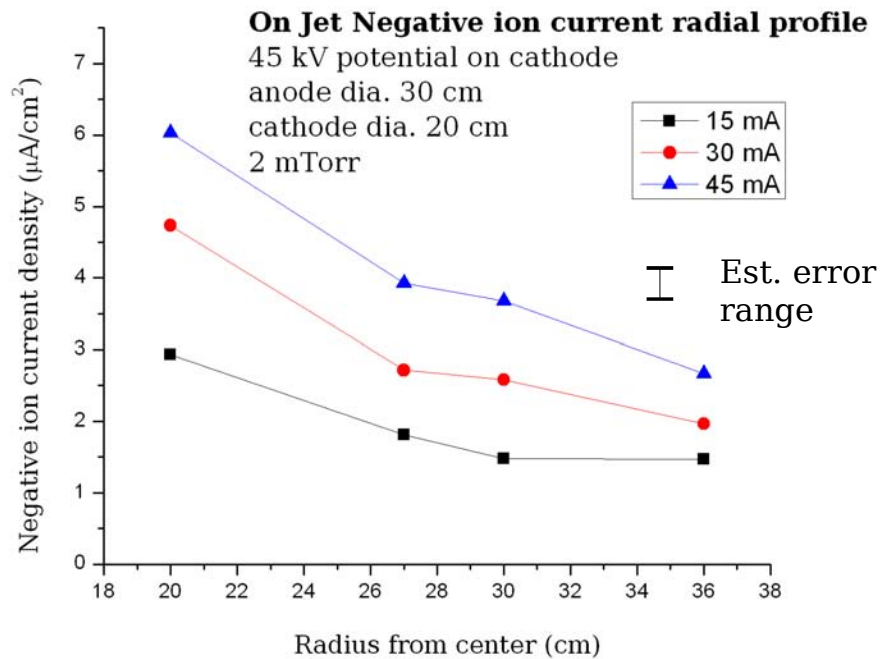


Figure VI-21: Comparison of how Faraday cup measurements of negative ion current changes with radius in an IEC device with a 30 cm diameter anode and 20 cm diameter cathode, aligned with a plasma jet. This plot shows three different negative ion currents, with 45 kV of potential applied to the cathode. This is the same data is shown in fig. VI-19.

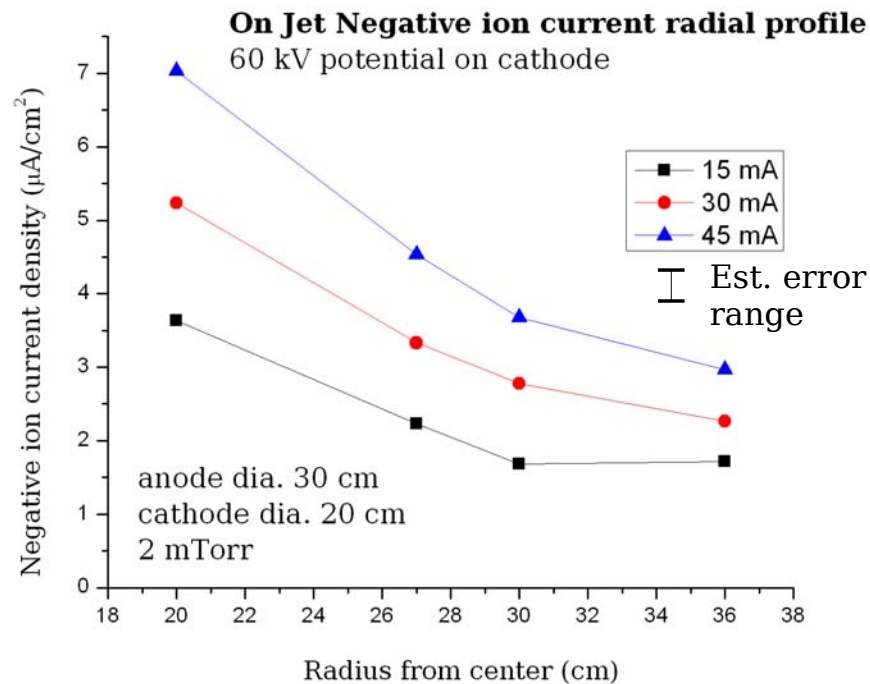


Figure VI-22: Comparison of how Faraday cup measurements of negative ion current changes with radius in an IEC device with a 30 cm diameter anode and 20 cm diameter cathode, aligned with a plasma jet. This plot shows three different negative ion currents, with 60 kV of potential applied to the cathode. This is the same data is shown in fig. VI-19.

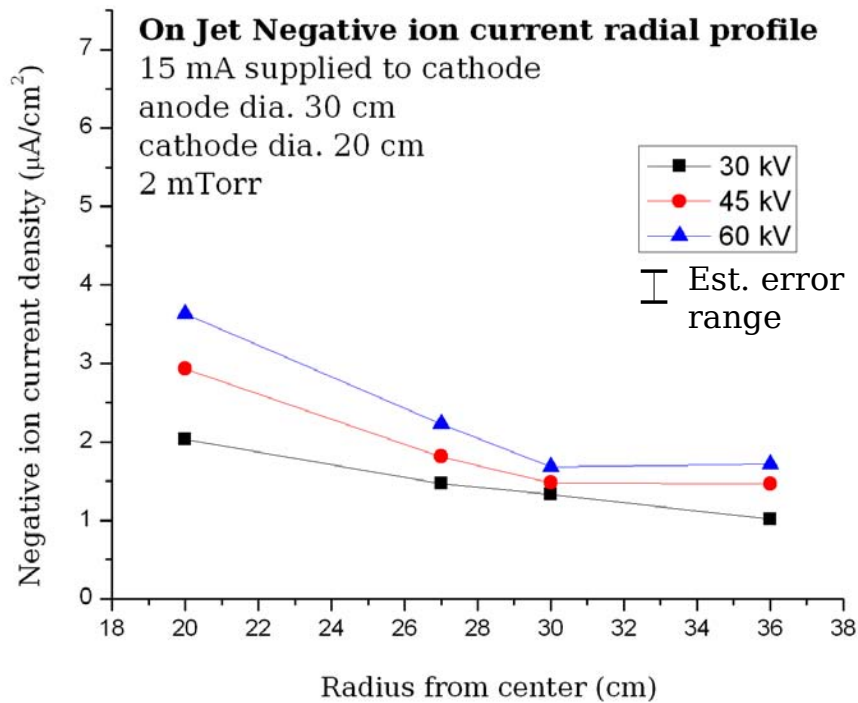


Figure VI-23: Comparison of how Faraday cup measurements of negative ion current changes with radius in an IEC device with a 50 cm diameter anode and 20 cm diameter cathode, aligned with a cathode wire. This plot shows three different negative ion currents, with 15 mA of meter current supplied to the cathode. This is the same data is shown in fig. VI-19.

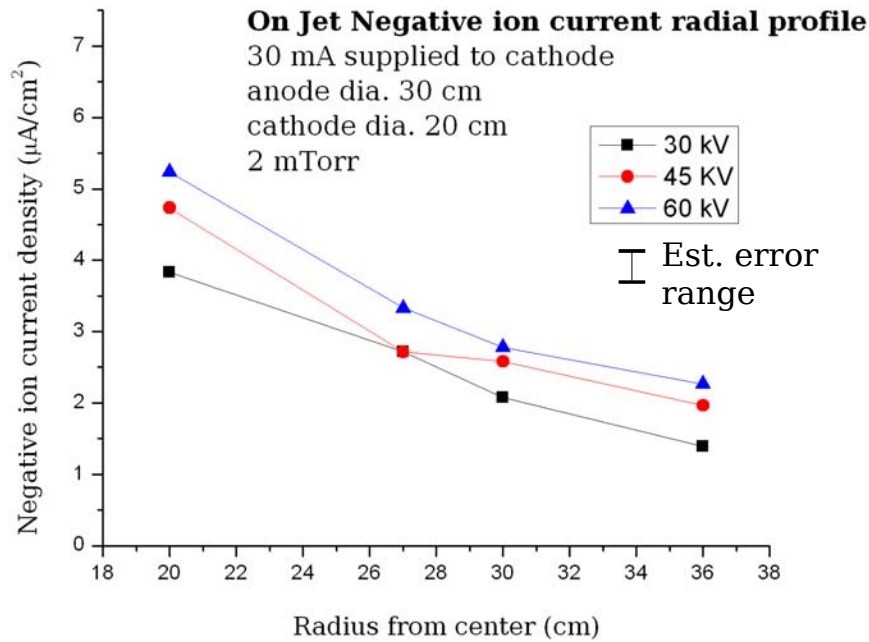


Figure VI-24: Comparison of how Faraday cup measurements of negative ion current changes with radius in an IEC device with a 50 cm diameter anode and 20 cm diameter cathode, aligned with a cathode wire. This plot shows three different negative ion currents, with 30 mA of meter current supplied to the cathode. This is the same data is shown in fig. VI-19.

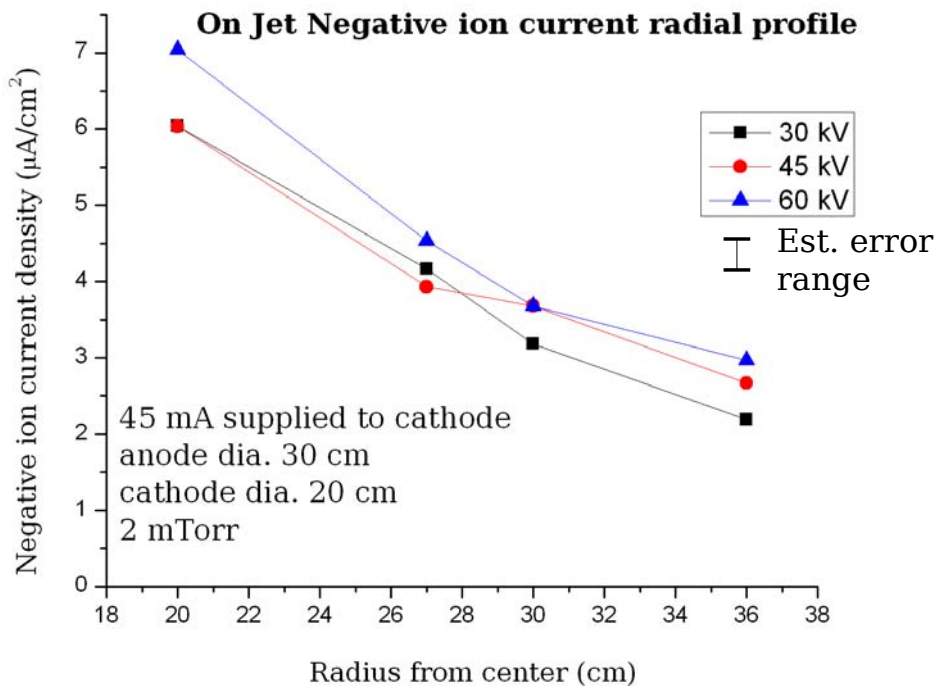


Figure VI-25: Comparison of how Faraday cup measurements of negative ion current changes with radius in an IEC device with a 50 cm diameter anode and 20 cm diameter cathode, aligned with a cathode wire. This plot shows three different negative ion currents, with 45 mA of meter current supplied to the cathode. This is the same data is shown in fig. VI-19.

VI.2.2: Faraday cup azimuthal measurements

Azimuthal profile measurements were taken only with the 20 cm cathode – 30 cm anode configuration. The field of view allowed a scan across two jets and part of a third. The jet positioned such that its center is equidistant from the neighboring columns of filaments will be referred to as the central jet. The neighboring jets will be referred to as the left and right jets, as viewed through the window opposite the Faraday cup field of view, as illustrated in fig. VI-26. These azimuthal measurements were taken at a

radius of 27 and 32 cm from the center of the anode and cathode.

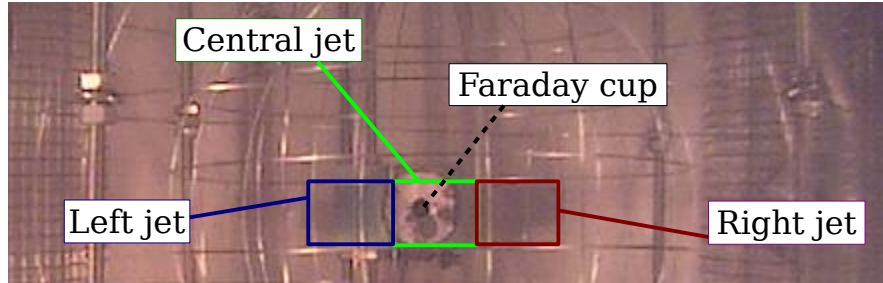


Figure VI-26: Photograph of Faraday cup and its field of view in the HOMER IEC device in the 30 cm anode - 20 cm cathode configuration. The cathode holes that give rise to the left, central, and right jets are called out.

As discussed in the previous section, the measurements from the Faraday cup are read from the average calculated by an oscilloscope. As such, the Faraday cup measurement does not lend itself to rigorously calculating statistical error without developing a more sophisticated data taking apparatus. As before, the variation in the measured average is reported, and in the data reported in this section varied by as much as $\pm 0.2 \mu\text{A}$; this is lower than in the previous section, because the bandwidth on the low pass filter was set to a lower frequency.

As shown in figures VI-27 and 28, the jet profiles were not the same across the measured jets. The peak and minimum magnitude at similar parameters are roughly the same magnitude across the measured jets, but the widths of the jets are different. The jets also evolved differently with distance from the center of the spherical cathode. The magnitude of the central jet varied with distance from the center of the cathode, but the left jet showed a different jet shape when comparing radii. The field of view

was not wide enough to obtain a good measurements of the right jet profile for comparison.

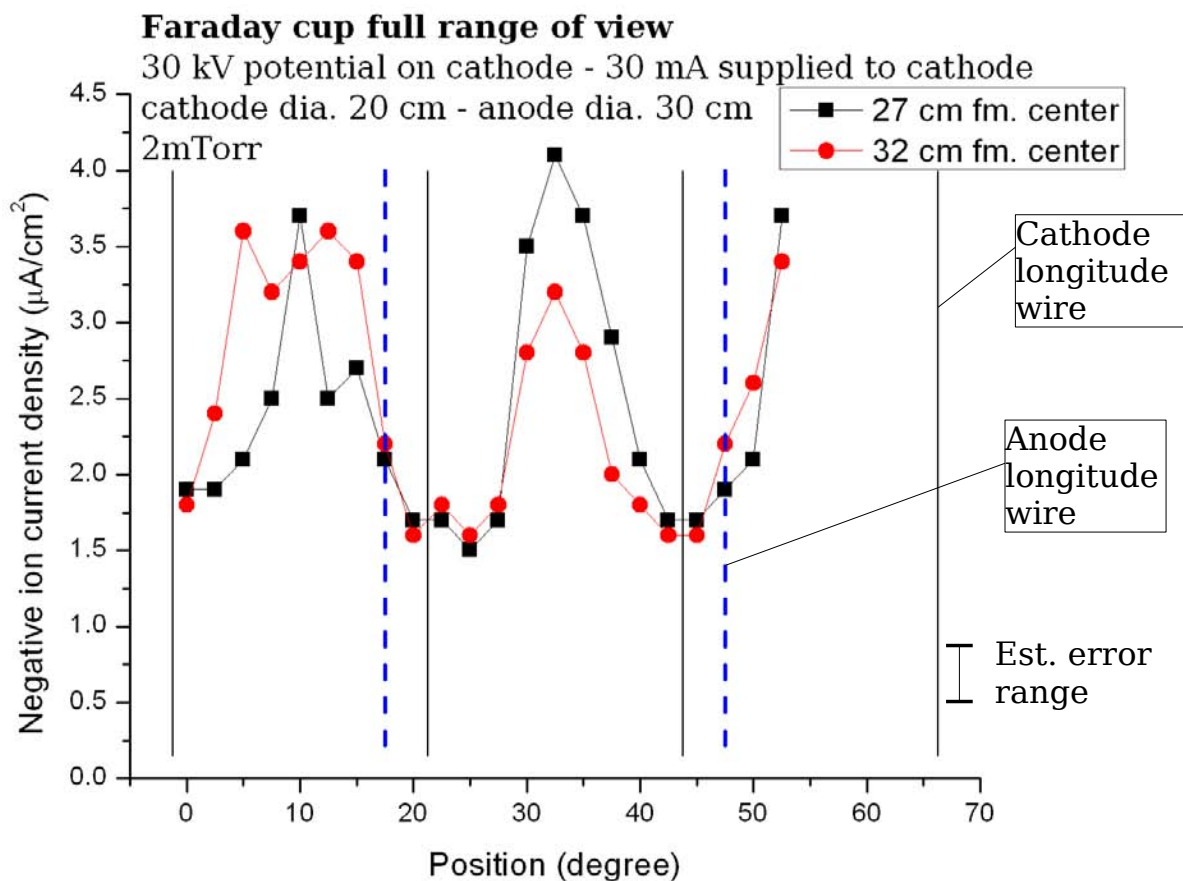


Figure VI-27: Full azimuthal range field of view at 30 kV potential applied to the cathode and 30 mA meter current supplied to the cathode, at 27 and 32 cm from the center of the cathode. The HOMER IEC device was run with a 20 cm diameter cathode and 30 cm diameter anode, with a background pressure of 2 mTorr.

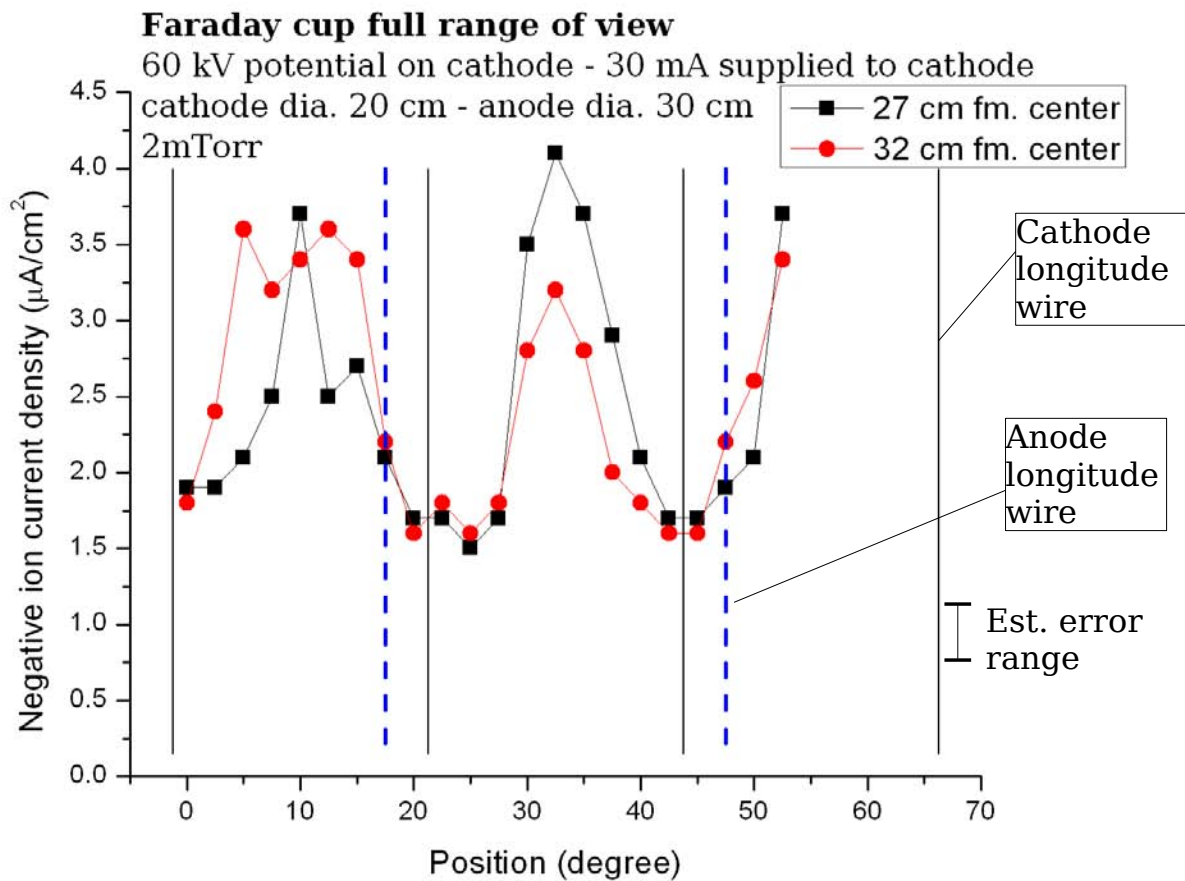


Figure VI-28: Full azimuthal range field of view at 60 kV potential applied to the cathode and 30 mA meter current supplied to the cathode, at 27 and 32 cm from the center of the cathode. The HOMER IEC device was run with a 20 cm diameter cathode and 30 cm diameter anode, with a background pressure of 2 mTorr.

A variety of parametric scans were done, measuring jets in the Faraday cup field of view. Parametric scans of current supplied to the cathode were carried out on the central jet in the same anode-cathode orientation as in figures 27 and 28, and were significant because they

confirm that the negative ion current has a linear dependence on the cathode current. The shape of the negative ion current profile in a jet seems to be insensitive to cathode current, evidencing only a linear change in magnitude, as shown in figures VI-29 and 30. This result gives confidence that parametric scans can be carried out at constant cathode current because jet profiles will not be perturbed by cathode current.

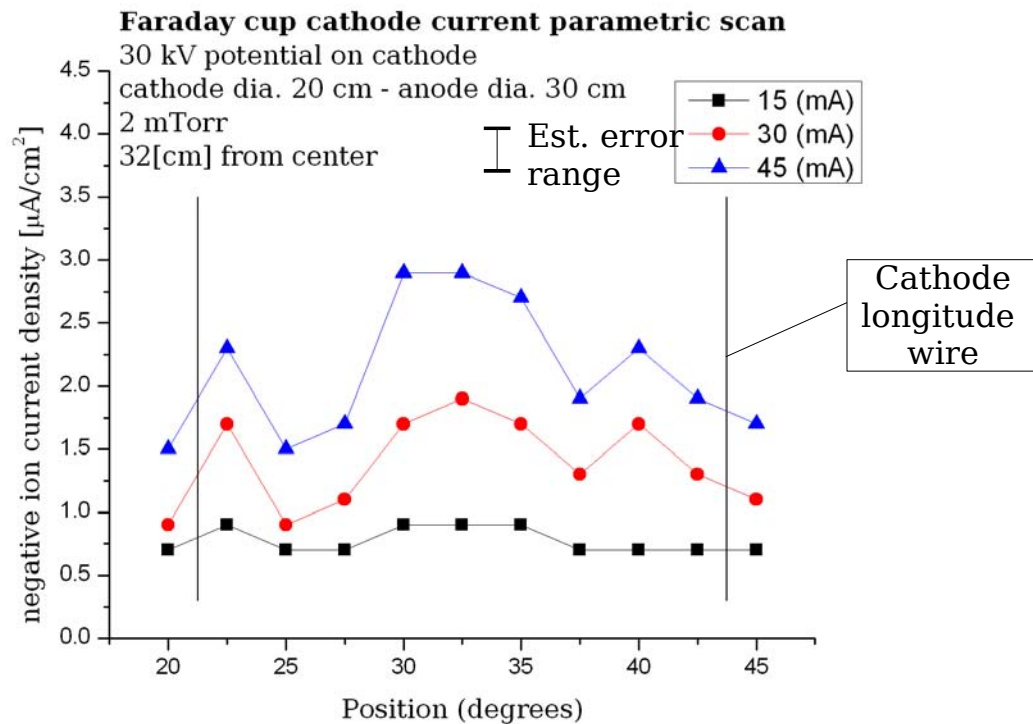


Figure VI-29: Cathode current parametric scan of the negative ion jet with a 30 kV potential applied to the cathode. The HOMER IEC device was run with a 20 cm diameter cathode and 30 cm diameter anode, with a background pressure of 2 mTorr.

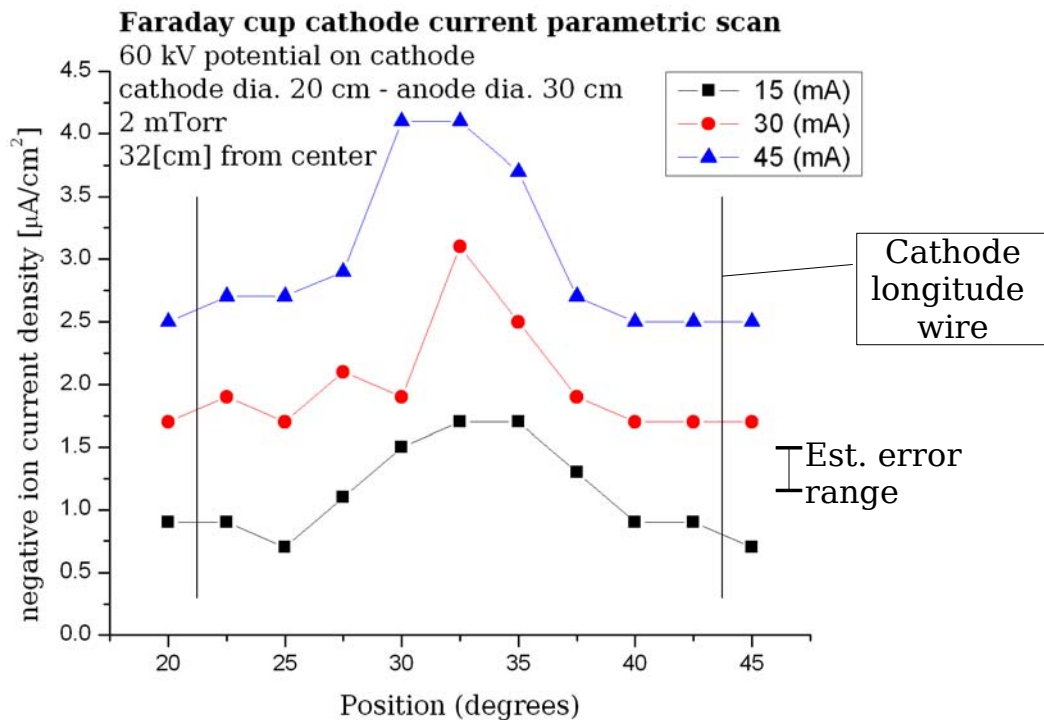


Figure VI-30: Cathode current parametric scan of the negative ion jet with a 30 kV potential applied to the cathode. The HOMER IEC device was run with a 20 cm diameter cathode and 30 cm diameter anode, with a background pressure of 2 mTorr.

Cathode voltage parametric scans at 27 cm from the center of the chamber show that the magnitude and profile of the central jet respond to the cathode voltage, as illustrated in fig. VI-31. This cathode voltage parametric scan can be compared with a similar parametric scan at 32 cm from the center of the chamber to compare how the profile responds to cathode voltage at a higher radius, as shown in fig. VI-32.

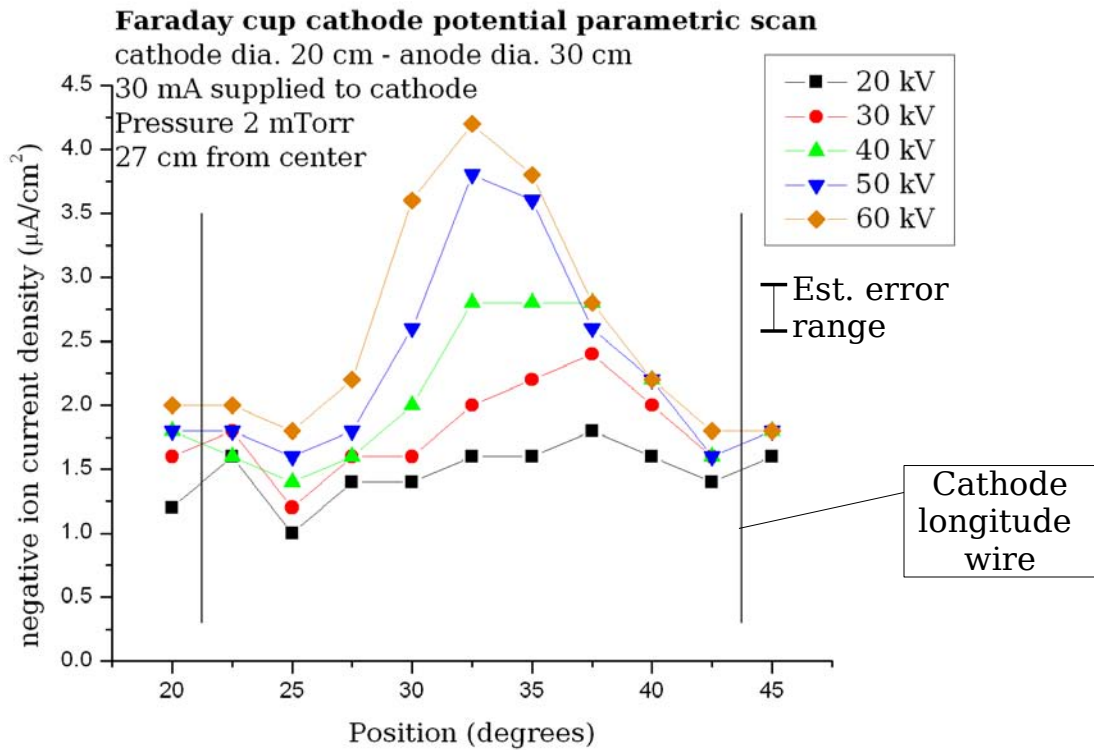


Figure VI-31: Cathode voltage parametric scan of negative ion central jet profile at 27 cm from the center of the HOMER IEC device with a cathode of 20 cm diameter and anode of 30 cm diameter, 30 mA of meter current supplied to the cathode, and background pressure of 2 mTorr.

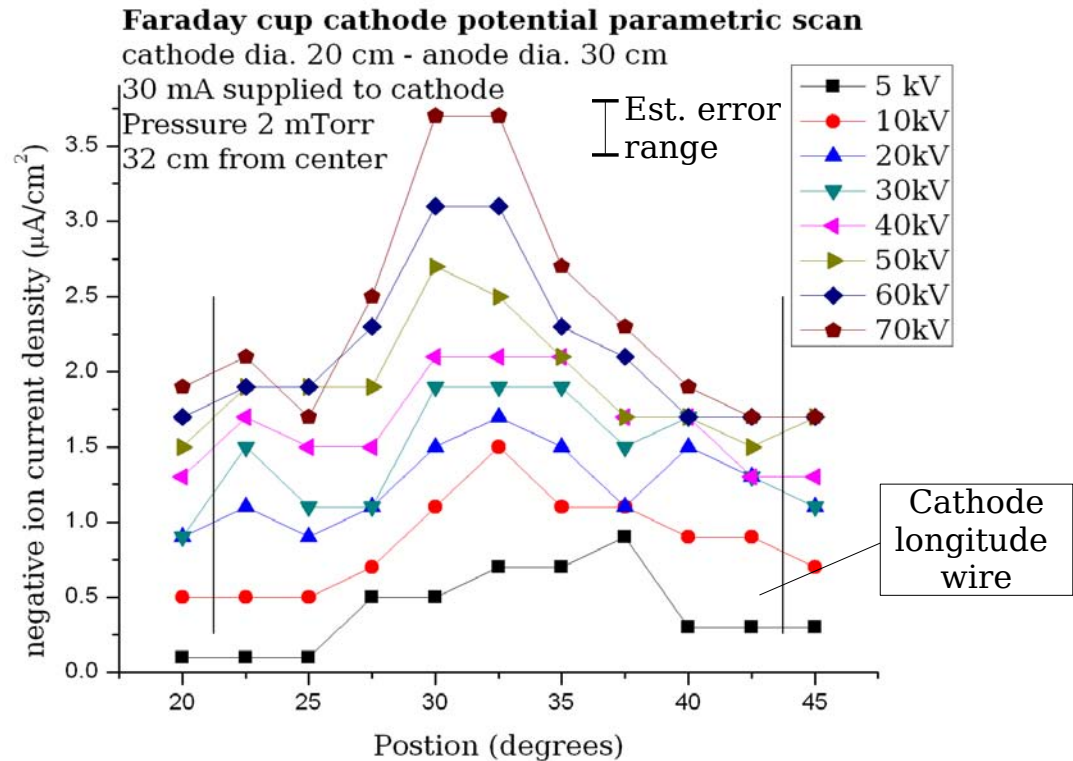


Figure VI-32: Cathode voltage parametric scan of negative ion central jet profile at 32 cm from the center of the HOMER IEC device with a cathode of 20 cm diameter and anode of 30 cm diameter, 30 mA of meter current supplied to the cathode, and background pressure of 2 mTorr.

The total current across the azimuth can be summed to produce a sense of how the total negative ion current in an IEC device jet changes with potential on the cathode. This current provides the low bound for the magnitude of the negative ion current in the jet at studied parameters. Taking the data from figures VI-31 & 32, at the previously described conditions, the sum of the current measured across the azimuth is given in fig. VI-33.

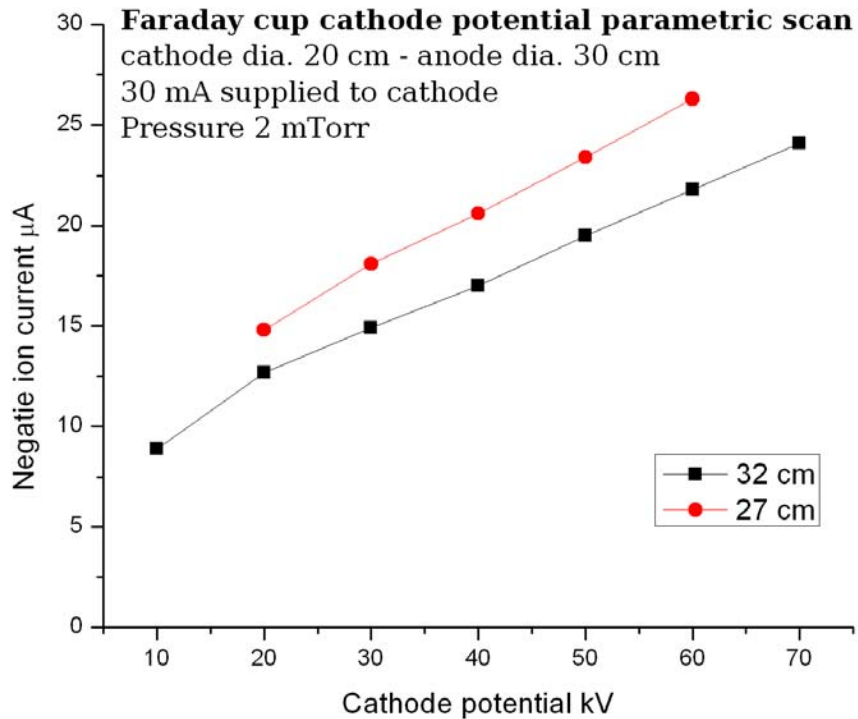


Figure VI-33: Cathode voltage parametric scan of total negative ion central jet current measured across the azimuth of the jet at 27 cm and 32 cm from the center of the HOMER IEC device with a cathode of 20 cm diameter and anode of 30 cm diameter; 30 mA of meter current supplied to the cathode, and background pressure of 2 mTorr.

Measurements were also made at constant cathode voltage and cathode current, but with different columns of filaments powered to study how the ion source created by the filaments impacted the negative ion current in the jets, and determine if the electron emitting filaments are responsible for the observed variation in jet profile. These electron emitting filaments produce the source plasma and are discussed in section V.2 with diagrams showing their position relative to the Faraday cup in figures V-14 through 16.

Measurements with varied configurations of filaments powered were taken at 27 cm from the center of the spherical cathode, with a 30 kV potential on the cathode and 30 mA of meter current supplied to the cathode and 2 mTorr of background gas, are shown in figs. VI-34 to 36. For these experiments, an anode longitude line was positioned just off the center of the central jet. The influence of the anode on the negative ions profile was not obvious in these or other experiments.

This data was taken earlier in the experimental series, before methods to determine the absolute positioning of the Faraday cup had been developed, as discussed in Chapter V. In the following plots, perturbations to the filaments were made at the same position, before adjusting the Faraday cup positioning. Therefore, although the accuracy of the shape of the jets is inconclusive, comparing the change in current at a given position yields valid information about the change in current due to the change in filaments.

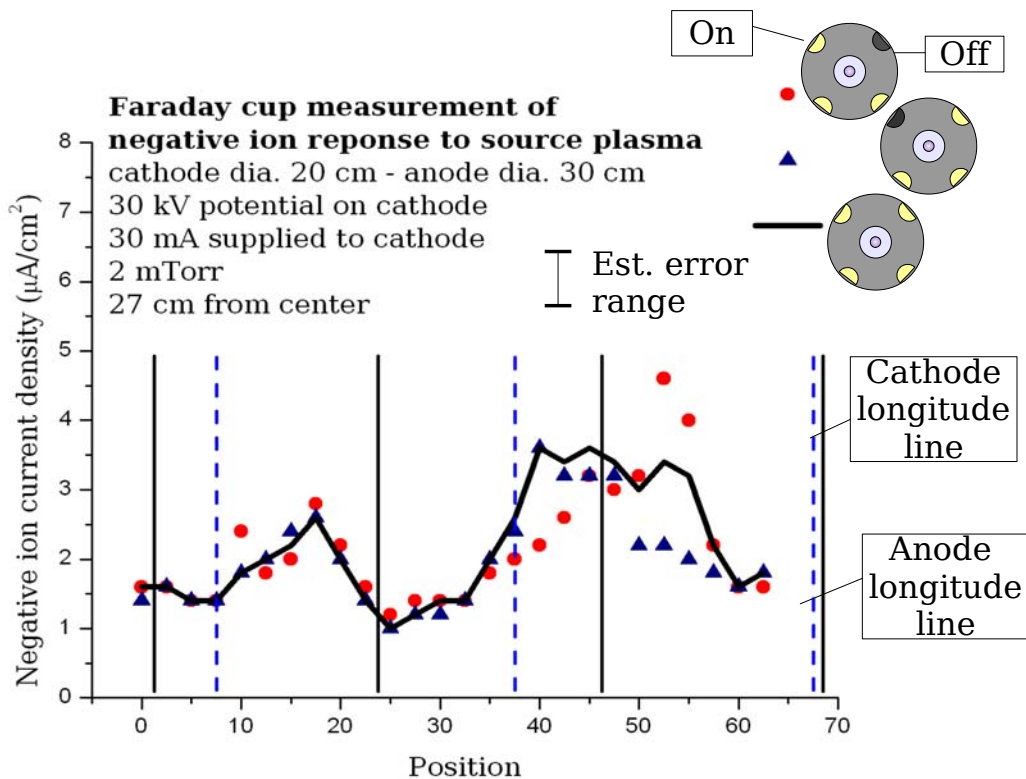


Figure VI-34: Negative ion current measurements by Faraday cup in HOMER IEC device across multiple jets, showing change as single filament columns are disconnected. The cathode diameter is 20 cm and the anode diameter is 30 cm; 30kV of potential is applied to the cathode, and 30 mA of meter current is supplied to the cathode, with a background pressure of 2 mTorr. The legend utilizes a simple diagram of the IEC device, with anode-cathode at the center, Faraday field of view at the top, and yellow filament positions showing the filaments that are active.

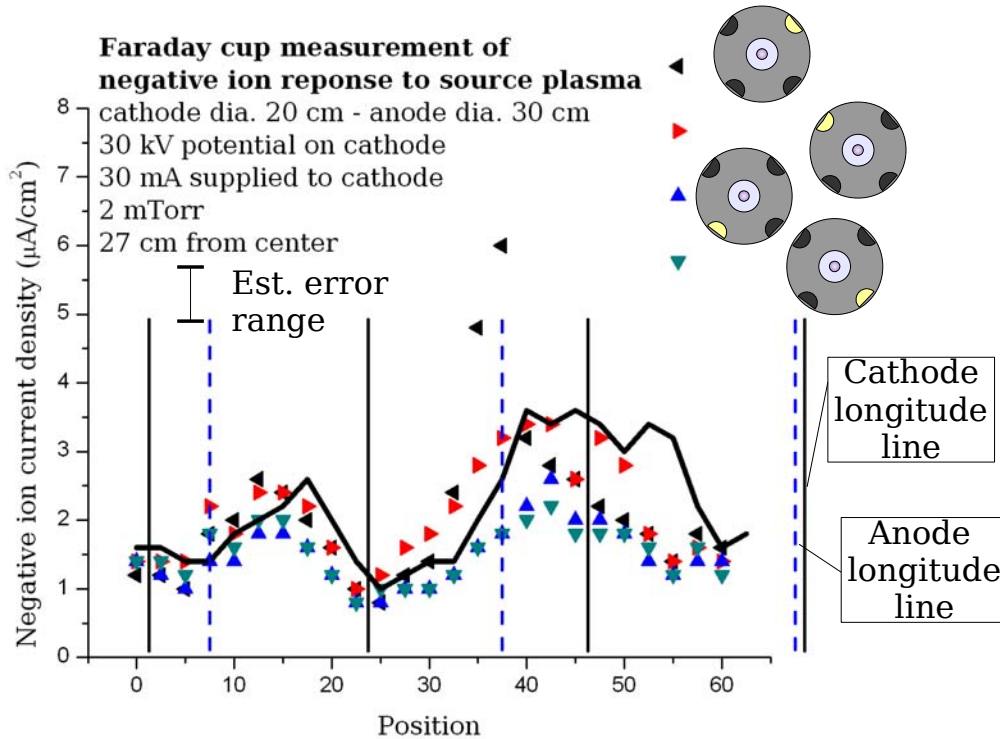


Figure VI-35: Negative ion current measurements by Faraday cup in HOMER IEC device across multiple jets, showing change as single filament columns are powered. The cathode diameter is 20 cm and the anode diameter is 30 cm; 30kV of potential is applied to the cathode, and 30 mA of meter current is supplied to the cathode, with a background pressure of 2 mTorr. The legend utilizes a simple diagram of the IEC device, with anode-cathode at the center, Faraday field of view at the top, and yellow filament positions showing the filaments that are active. The black line shows all the filaments on.

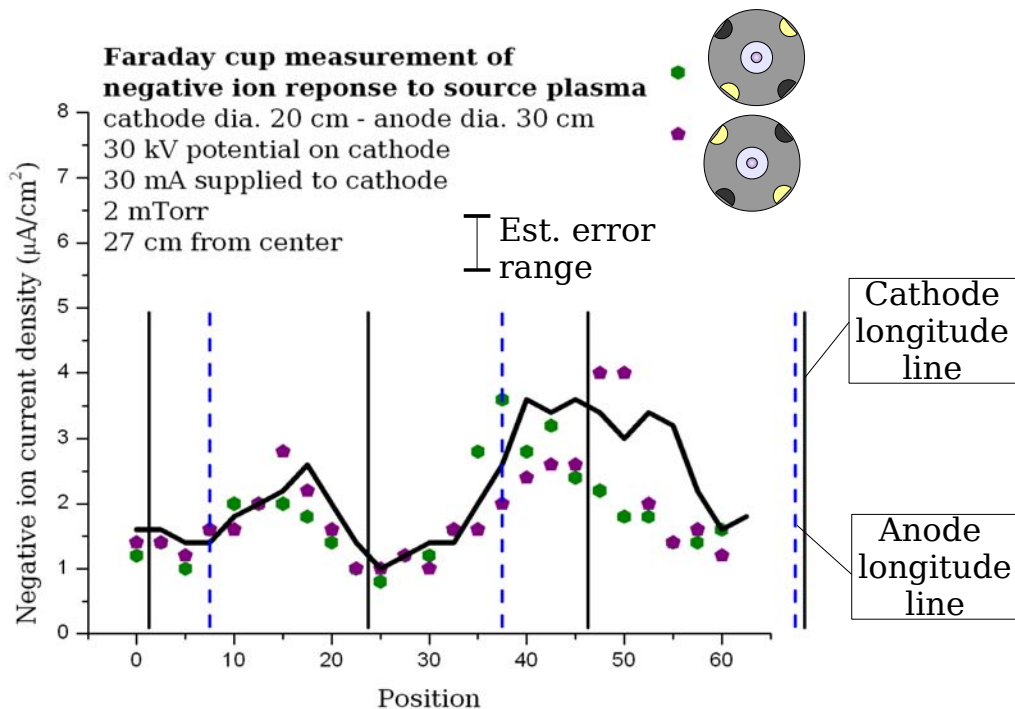


Figure VI-36: Negative ion current measurements by Faraday cup in HOMER IEC device across multiple jets, showing change as opposite pairs of filament columns are powered. The cathode diameter is 20 cm and the anode diameter is 30 cm; 30kV of potential is applied to the cathode, and 30 mA of meter current is supplied to the cathode, with a background pressure of 2 mTorr. The legend utilizes a simple diagram of the IEC device, with anode-cathode at the center, Faraday field of view at the top, and yellow filament positions showing the filaments that are active. The black line shows all the filaments on.

These plots show that the negative ion current has isolated response to perturbations to the filaments that emit electrons that produce the source plasma in the HOMER IEC device. For much of the observations the negative ion current perturbation from the electron emitting filaments was within the variation of the reading, but the cases where a variation was observed the change was as much as a factor of 3. In particular, the

filament to the right of the azimuthal field of view of the Faraday cup seems to cause an increase in negative ion current near 37.5° , rather close to an anode wire. The cause for this and how the anode impacts the negative ion current has not been explored. Further study should be undertaken to see if the variation in negative ion current in response to perturbation in the source plasma is significant.

Hysteresis scans were performed to determine if a time dependent effect, such as grid heating, impacts the shape of the plasma jets in an IEC device. This scan was performed by scanning from right to left (starting at 52.5 and proceeding to 0 in the terminology established in section V.4.4) instead of the left to right as typically undertaken. The results of this hysteresis scan are shown in fig. VI-37.

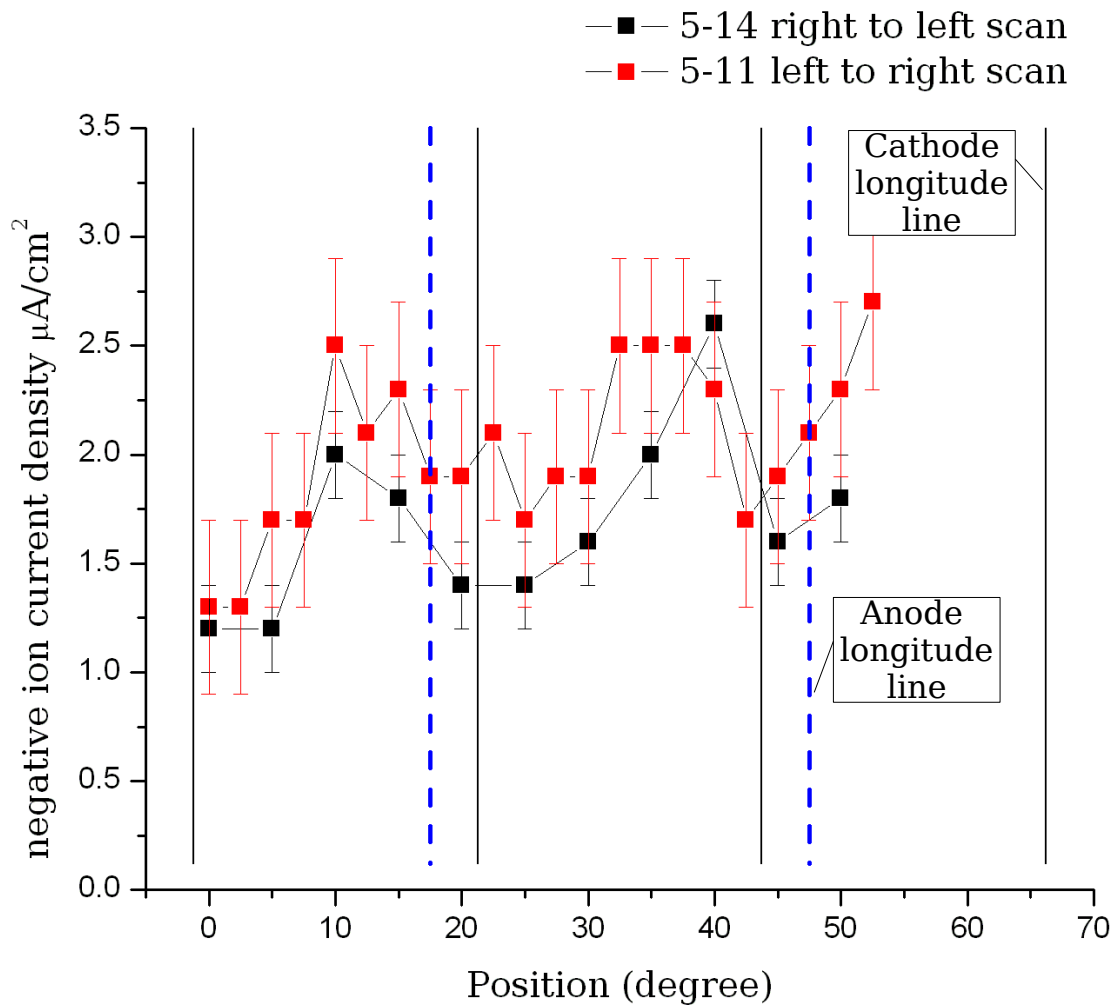


Figure VI-37: Hysteresis scan taken in the HOMER IEC device with a cathode of diameter 20 cm and anode of 30 cm, 30 kV potential on the cathode and 30 mA meter current supplied to the cathode. The measurements were taken 27 cm from the center of the cathode. The hysteresis scan shows that the data measured currents overlap within the variation of the measurement, confirming that the negative ion current is mainly insensitive to time dependent phenomenon.

It may be that the jet profiles are impacted by the anode or cathode positioning slightly off center producing asymmetric electric fields. This hypothesis has not been experimentally tested.

A number of broad conclusions can be drawn from the results presented in this chapter:

- The first computational simulation of negative ion currents in an IEC device has been executed and is producing results that can be compared with experimental measurements.
- The VICTER negative ion subroutine predicts that almost all negative ions are born from atomic fast neutrals in the IEC device.
- The VICTER negative ion subroutine results contradict the hypothesis that the structure of the negative ion energy spectrum arises from the atomic and molecular weights of the parentage of the negative ions distributing momentum to their daughter products when they undergo charge exchange and dissociation reactions. Positive ions that are grandparent to the negative ions in an IEC device contribute across the entire negative ion energy spectrum.
- Radial negative ion measurements from a Faraday cup in the HOMER IEC device confirm that the negative ion current density decreases with radius. The falloff in intensity responds to potential on the cathode.
- Azimuthal measurements from a Faraday cup in the HOMER IEC device confirm that negative ions are a component of the plasma jets observed in an IEC device. These measurements confirm that these

jets exist in conditions where the jets are not visible, and have provided the first measurements of an IEC device plasma jet profile.

- Azimuthal measurements from a Faraday cup in the HOMER IEC device have also shown that jets may not be uniform in profile, though in the observed jets the peak and minimum magnitude were similar at constant conditions. The reason for variation across these jets is unknown.
- The variation in the filaments producing a filament assisted source plasma may contribute to the variation in jets to some extent, and misalignment in anode-cathode centering likely results in jet variation as well.
- Time dependent effects in an IEC device do not seem to impact the production of negative ions.

- [VI-1] D. R. Boris, "Novel Diagnostic Approaches to Characterizing the Performance of the Wisconsin Inertial Electrostatic Confinement Plasma," Ph.D. Thesis, University of Wisconsin - Madison, 2009.
- [VI-2] D. R. Boris, E. C. Alderson, et al., "Deuterium anions in inertial electrostatic confinement devices," *Physical Review E*, vol. 80, no. 3, pp. 036408, 2009.

VII: Discussion of Results

This chapter will compare the VICTER code [VII-1,2] and its negative ion subroutine results to experimental results. More specifically, a negative ion energy spectrum predicted by VICTER will be compared to Magnetic Deflection Energy Analyzer (MDEA) diagnostic results [VII-3,4]. Next, VICTER negative ion subroutine parametric studies will be compared to Faraday cup measurements in experimental parametric campaigns. The results will provide benchmarks for the VICTER code, and provide guidance for improving the VICTER code. Finally, the negative ion jet profiles will be examined and extrapolations will be made.

VII.1: Experimental and modeling energy spectrum comparisons

There are multiple ways to assess the VICTER results. The first element is the predicted VICTER negative ion energy spectrum. The most direct comparison one can make is the VICTER energy spectrum predicted at the wall of HOMER, shown in fig. VII-1, and the energy spectrum determined by the Magnetic Deflection Energy Analyzer (MDEA) at the same conditions, shown in fig. VII-2.

These spectra have a variety of features in common. They both show a mulit-peaked energy structure with the peaks of a width on the order of 10 to 20 keV. Comparing the energy spectra below 100 keV in the VICTER simulation to the MDEA result, both show the energy range of the Gaussians is roughly 60 keV wide. However, the the energy spectra in the VICTER simulations is between 1 and 60 keV, while the energy spectra in the MDEA result is between 40 and 100 keV. The obvious question at this juncture is, which energy spectrum is correct? There is supporting evidence for both positions.

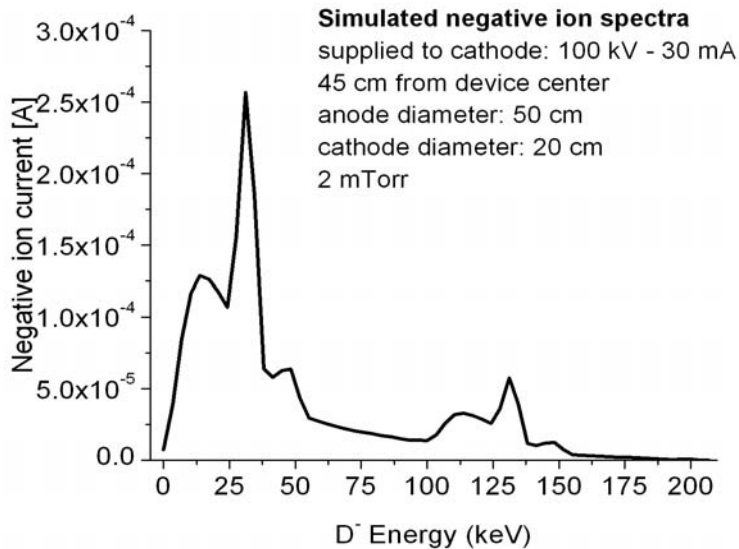


Figure VII-1: VICTER simulation of the negative ion energy spectrum at 45 cm from center of an IEC device with a 20 cm cathode, 50 cm anode with a -100 kV potential on the cathode and 30 mA supplied to the cathode, with a 2 mTorr background pressure.

The energy calibration of the MDEA diagnostic was determined from a SIMION simulation of negative ions traveling between the poles of a magnet to pass through a pair of 100 μm diameter irises, as diagrammed in fig. II-12. The magnetic field between the poles was measured, and applied to the SIMION simulation, but the results of the simulation were highly sensitive to fringing fields. If the actual field did not conform to the SIMION simulation the results would be significantly different. Also, the pair of 100 μm irises were simulated as perfectly aligned, which may not have been the case. The potential impact of iris misalignment on the energy calibration has not been determined at this time.

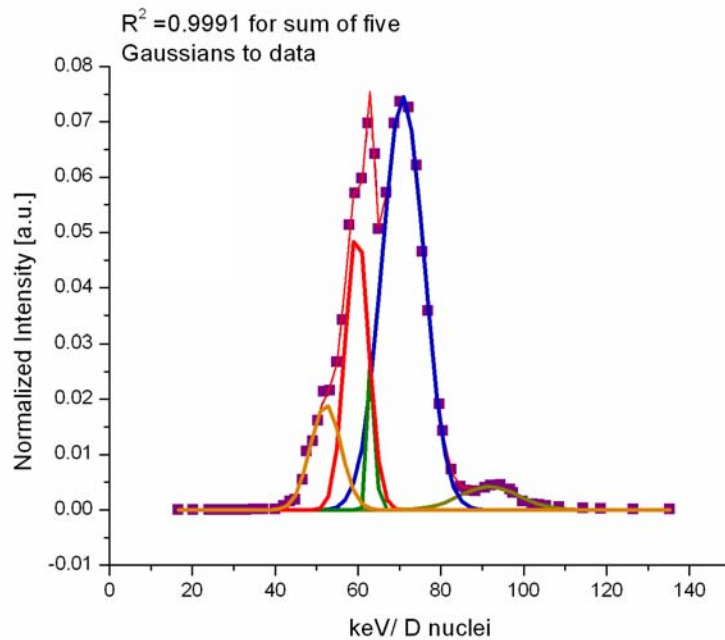


Figure VII-2: The negative ion energy spectrum determined by the Magnetic Deflection Energy Analyzer in the HOMER IEC device with a cathode dia. of 20 cm and anode dia. of 50 cm with -100 kV potential on the cathode and 30 mA of current supplied to the cathode, with 2 mTorr background pressure [VII-3]. The purple dots are data points, and the thin red line is the sum of the five Gaussian curves.

The Fusion Ion DOppler (FIDO) diagnostic is closely related to the MDEA, but the magnet is reversed to bend positively charged fusion products into a solid state detector [VII-3,5]. The count rate is low enough that energy of the fusion products can be resolved, and the Doppler shift of these fusion products can be used to determine the energy of the fast deuterium parent that produced the fusion reaction. An example of the resultant energy spectrum produced by this diagnostic can be found in fig. VII-3 [VII-5]. A voltage parametric scan showed a slight hardening of the fast deuterium energy spectrum at higher cathode potential [VII-3], but the

shape of the deuterium spectrum was largely unchanged.

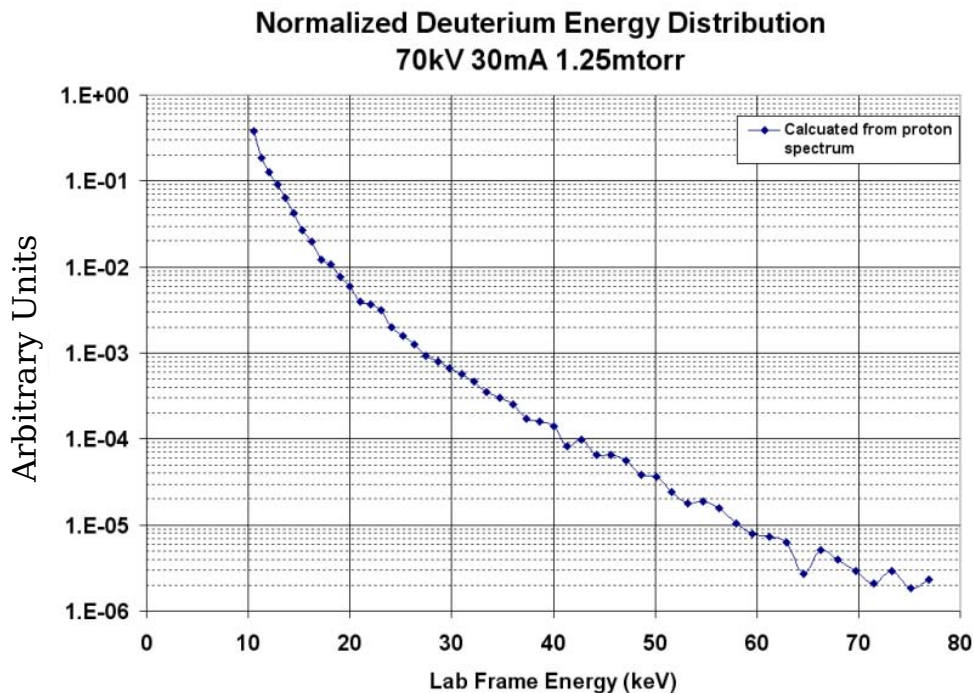


Figure VII-3: Energy spectrum of deuterium producing fusion in HOMER with -70 kV potential on the cathode and 30 mA meter current supplied to the cathode and a background pressure of 1.25 mTorr [VII-3,5].

Figure VII-3 shows that the vast majority of energetic deuterium producing fusion reactions are created by deuterium of an energy much lower than the cathode voltage. This deuterium spectrum consists of charged particles and fast neutrals. The results of the FIDO diagnostic suggest that the majority of the energetic deuterium of any charge state has less than 20 keV of kinetic energy, which should be reflected in the negative ion energy spectrum. The fact that there are no measurable negative ions of less than 30 keV apparent in the MDEA diagnostic results, as shown in figures VII-2 and 4, is suspect. If other comparisons between VICTER

results and measurements compared favorably, that would support the position that VICTER is modeling energy correctly, which we will discuss in the next section.

Further, VICTER is not the only simulation of negative ion current in an IEC device. Arthur Phelps developed a model of an IEC device that uses somewhat different assumptions from the VICTER code [VII-6], but produces results that are qualitatively similar. The negative ion simulations in his work also show a negative ion energy spectrum with a strong low energy component.

A voltage parametric scan carried out with the MDEA shows the negative ion current energy spectrum softens and the low energy threshold of the spectrum is lowered as cathode potential is reduced, as shown in fig. VII-4 [VII-3,4]. This softening shows that, if there is a mistake in the MDEA diagnostic, it is not simply one of simple miscalibration. There is some electrostatic potential leakage from the cathode outside the anode, which may accelerate negative ions born outside the anode and move the energy range lower threshold, but the potential leakage is not expected to be high enough in magnitude to account for the 10 to 15 kV difference in the low energy threshold observed in the MDEA diagnostic cathode potential parametric scan.

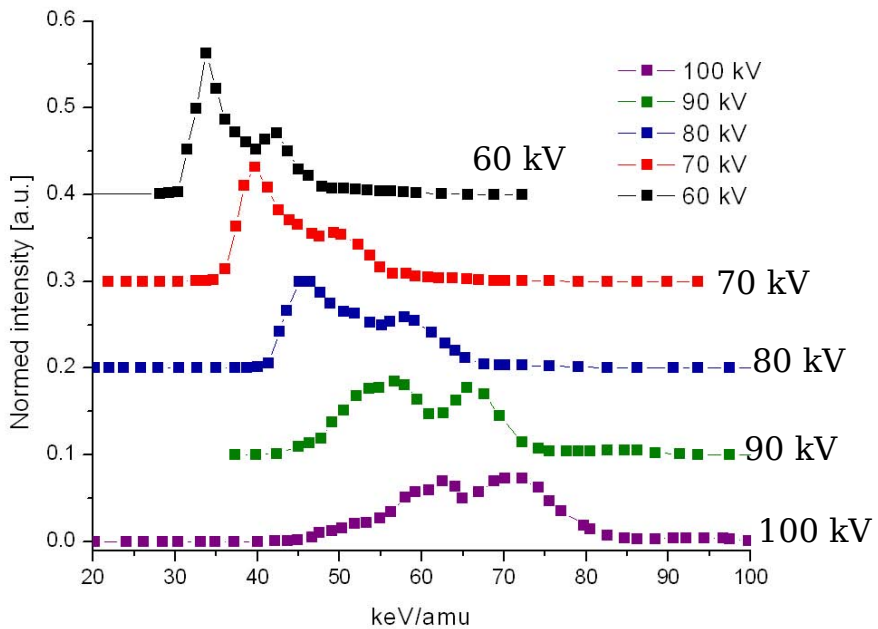


Figure VII-4: Voltage parametric scan from the Magnetic Deflection Energy Analyzer diagnostic in the HOMER IEC device at 30 mA supplied to the cathode and 2 mTorr background gas pressure [VII-3,4].

The uncertainty in the energy spectrum calibration produced by the analysis of the MDEA data impacts the previous interpretation that some of the observed Gaussian curves in fig. VII-2 are from electron attachment inside the cathode [VII-3, 4]. To begin with, it has not been established that one of the Gaussian curves correlates to deuterium at nearly the cathode energy, as the energy calibration is now in doubt. Further, the suggested Gaussian curve attributed to D_2^- is also in doubt because its energy may not be correct. Even more fundamentally, all other things being equal, a signal from D_2^- would not appear in the MDEA signal at 1/2 the energy of D^- with the same energy but rather $\sqrt{(1/2)}$ the energy of D^- with the same energy.

Ultimately, this discussion shows the need for further study. Calibration of the energy spectrum of the MDEA should be a priority in this effort. While the signal was too strong to obtain energy resolution with a pair of 100 μm irises, effort should be made with a single smaller iris, to reduce the negative ion count rate to a point that energy discrimination of the negative ion current can be made and correlated to magnetic field. Further modeling should be extended to examine how variation of the magnetic field and iris alignment can modify the results of the MDEA diagnostic. Once the results are well characterized, comparisons can confidently be made with VICTER results.

VII.2: Experimental and modeling parametric comparisons

VICTER can also be used to perform a variety of parametric simulations (cathode potential, cathode current, pressure, cathode and anode diameter, distance from center of the cathode, etc). There are multiple types of simulation that can be compared to Faraday cup measurements in the HOMER device. However, these comparisons should be made with the caveat that VICTER's results are the product of a one-dimensional simulation, which is being compared to a 1 cm^2 diagnostic sample of a system that exhibits the three-dimensional physics of plasma jets. Simply comparing absolute values between the VICTER simulation and Faraday cup measurements would be a poor comparison, but if VICTER is

properly modeling the physics in an IEC device, within a 1 dimensional limit, experiment and simulation should exhibit the same parametric trends. As such, the results of the simulation and measurements must be normalized to make meaningful comparisons.

For the purposes of radial comparisons the analysis compares on-jet and off-jet radial measurements, using the 50 cm diameter anode, 20 cm diameter cathode at 2 mTorr as reported in Chapter VI. These results are compared to to the radial negative ion current densities predicted by VICTER at the same conditions. Such comparisons will be made with constant cathode current or cathode voltage. Each set of data (VICTER predictions, on-jet, and and off-jet measurements) will be normalized separately to the peak current for the parameter held constant. This may appear to show an off jet measurement higher than the on jet measurement for the same parameters, but in reality this is an artifact of the normalized value.

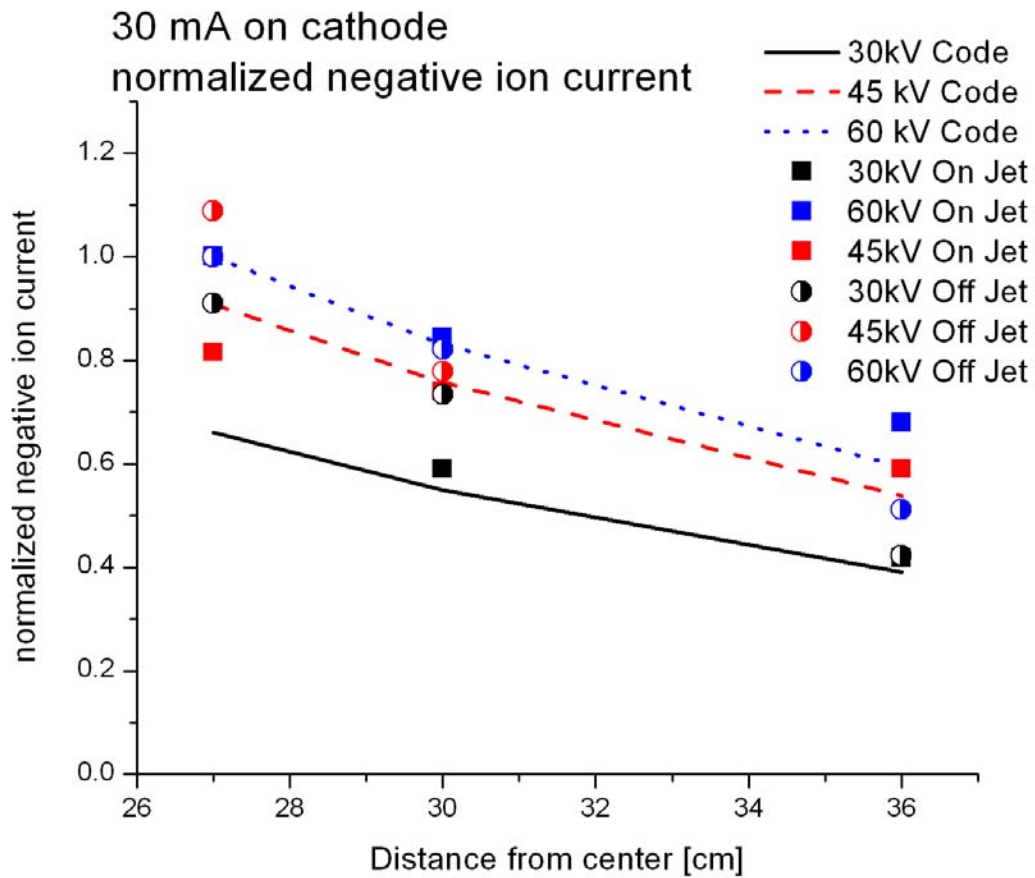


Figure VII-5: Normalized change in negative ion current with radial position at 30 mA supplied to the cathode and 30, 45, and 60 kV supplied to the cathode, as predicted by the VICTER negative ion subroutine, and as measured by the Faraday cup in the HOMER IEC device.

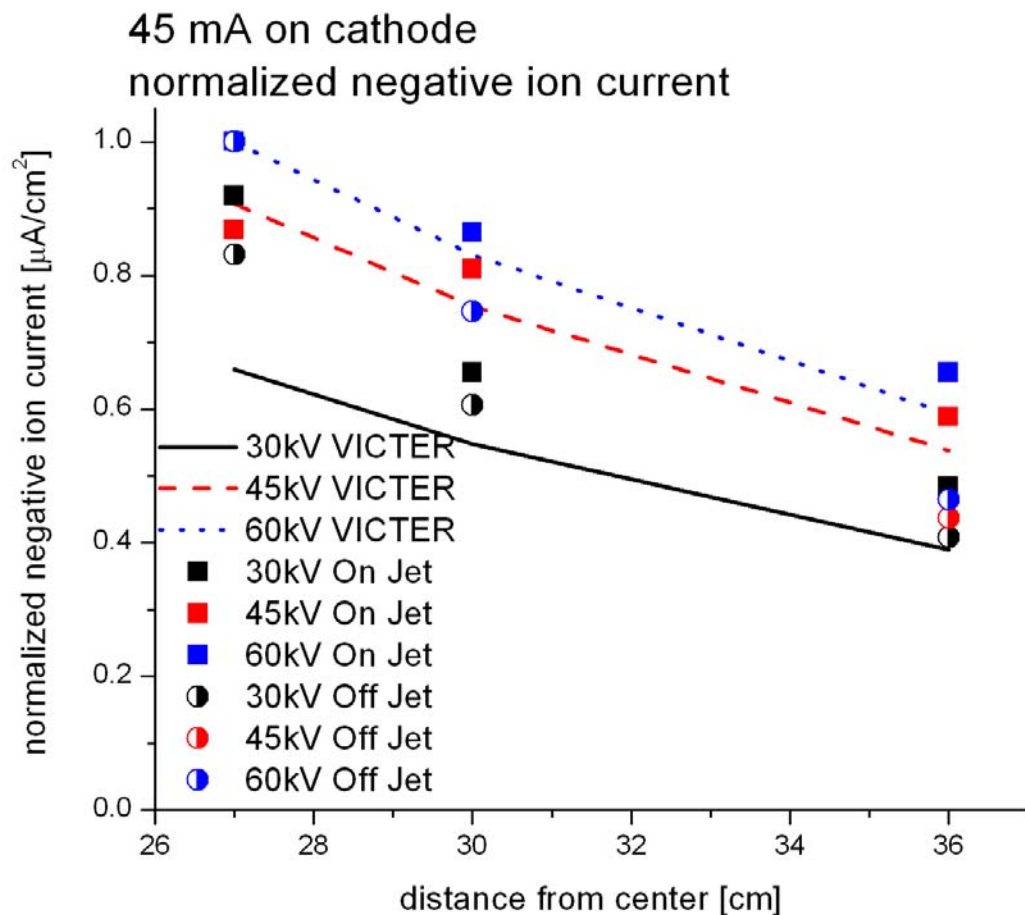


Figure VII-6: Normalized change in negative ion current with radial position at 45 mA supplied to the cathode and 30, 45, and 60 kV supplied to the cathode, as predicted by the VICTER negative ion subroutine, and as measured by the Faraday cup in the HOMER IEC device.

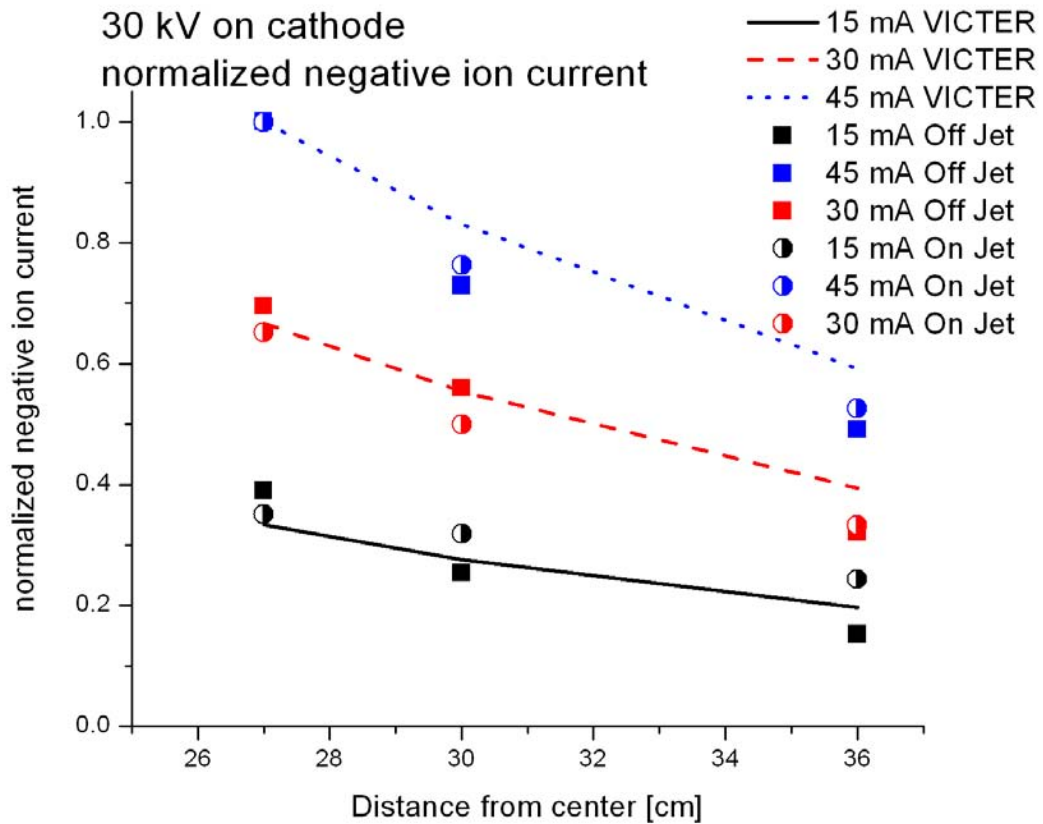


Figure VII-7: Normalized change in negative ion current with radial position at 30 kV supplied to the cathode and 15, 30, and 45 mA supplied to the cathode, as predicted by the VICTER negative ion subroutine, and as measured by the Faraday cup in the HOMER IEC device.

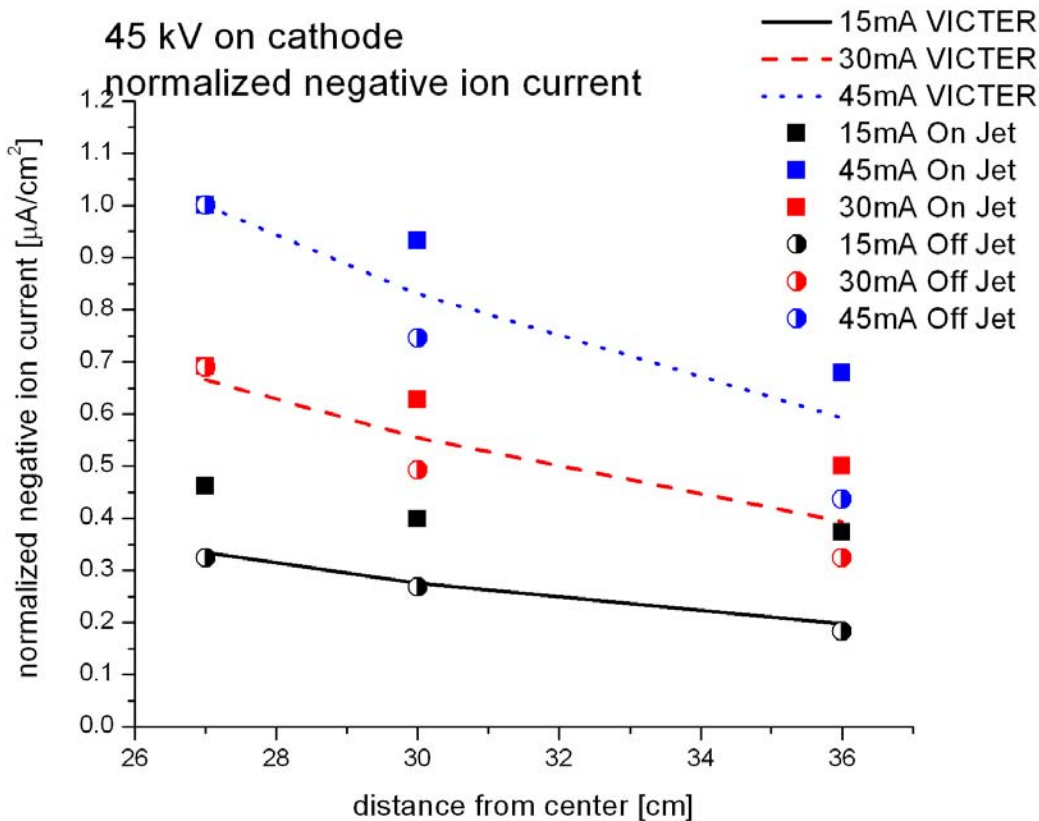


Figure VII-8: Normalized change in negative ion current with radial position at 45 kV supplied to the cathode and 15, 30, and 45 mA supplied to the cathode, as predicted by the VICTER negative ion subroutine, and as measured by the Faraday cup in the HOMER IEC device.

Figures VII-5 to 8 show that, within the parametric range explored, the VICTER negative ion subroutine does a reasonable job of modeling the trend of negative ion current change with radius in an IEC device. Also, the negative ion current radial response is similar on and off jet in the jet examined.

The next parametric study to be considered is how the negative ion current changes with cathode potential. As the voltage difference between

the cathode and anode is increased, the depth of the potential well is increased. This increases the energy the negative ions can reach as they move radial outward, but it also increases the number of low energy charge exchange reactions that can occur as positive ions travel down the potential well. The charge exchange reactions leave behind cold positive ions that can in turn undergo the same process. Because the well is deeper more generations of cold positive ions can accelerate to the energy where the charge exchange cross section is strong.

Because the cathode potential parametric measurements are compared at a constant radius, one can sum the voltage parametric jet profile measurements across the azimuth of the plasma jet and compare this sum with the VICTER results. Summing the measurements across the jet has a variety of advantages to comparing with the measurement at one location. Firstly, summing the current reduces uncertainty from each individual measurement. Summing the currents also mitigates variation between azimuthal positions as the profile of the jet evolves in response to the cathode potential. Further, summing the negative ion current in the azimuthal profile provides a more accurate sense of the total current in a jet for comparison. Following this approach, utilizing the previously gathered data, the potential parametric scan can be carried out at 27 cm in fig. VII-9 and 32 cm in fig. VII-10.

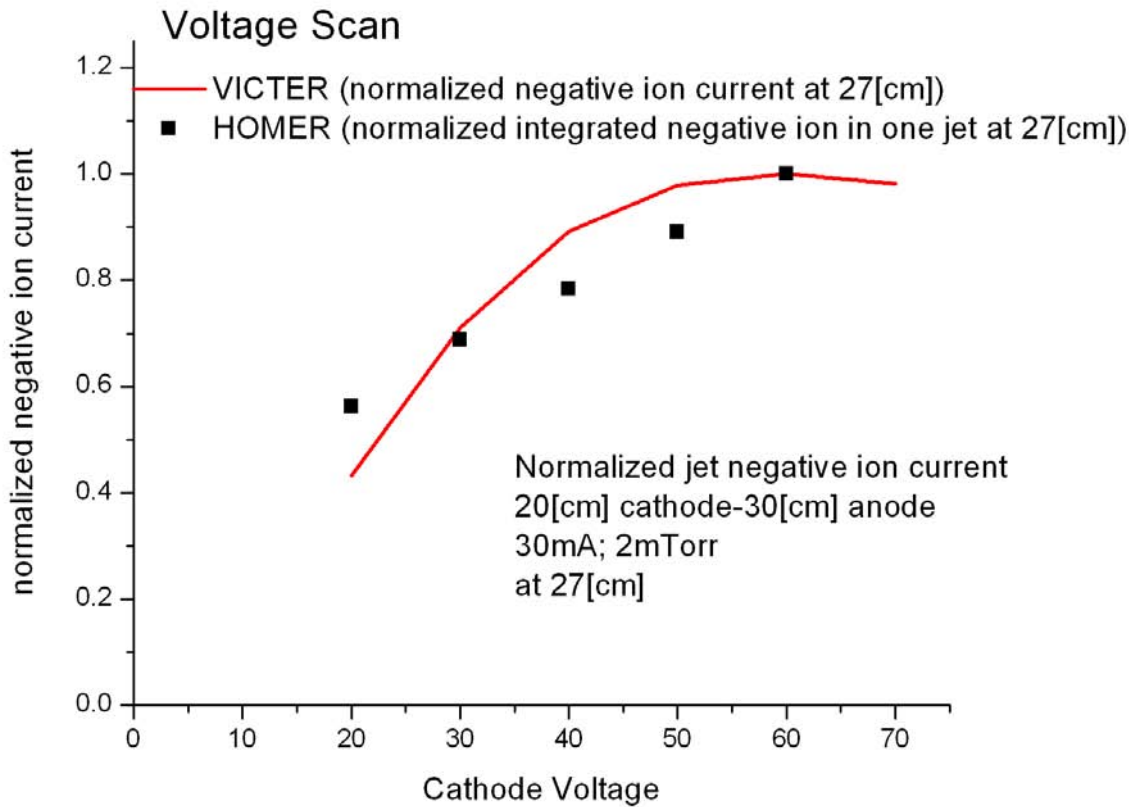


Figure VII-9: Cathode potential parametric comparison between the VICTER negative ion subroutine and Faraday cup measurements in the HOMER IEC device at 27 cm from the center of the potential well. This comparison shows qualitatively similar behavior, but differences in slope are evident.

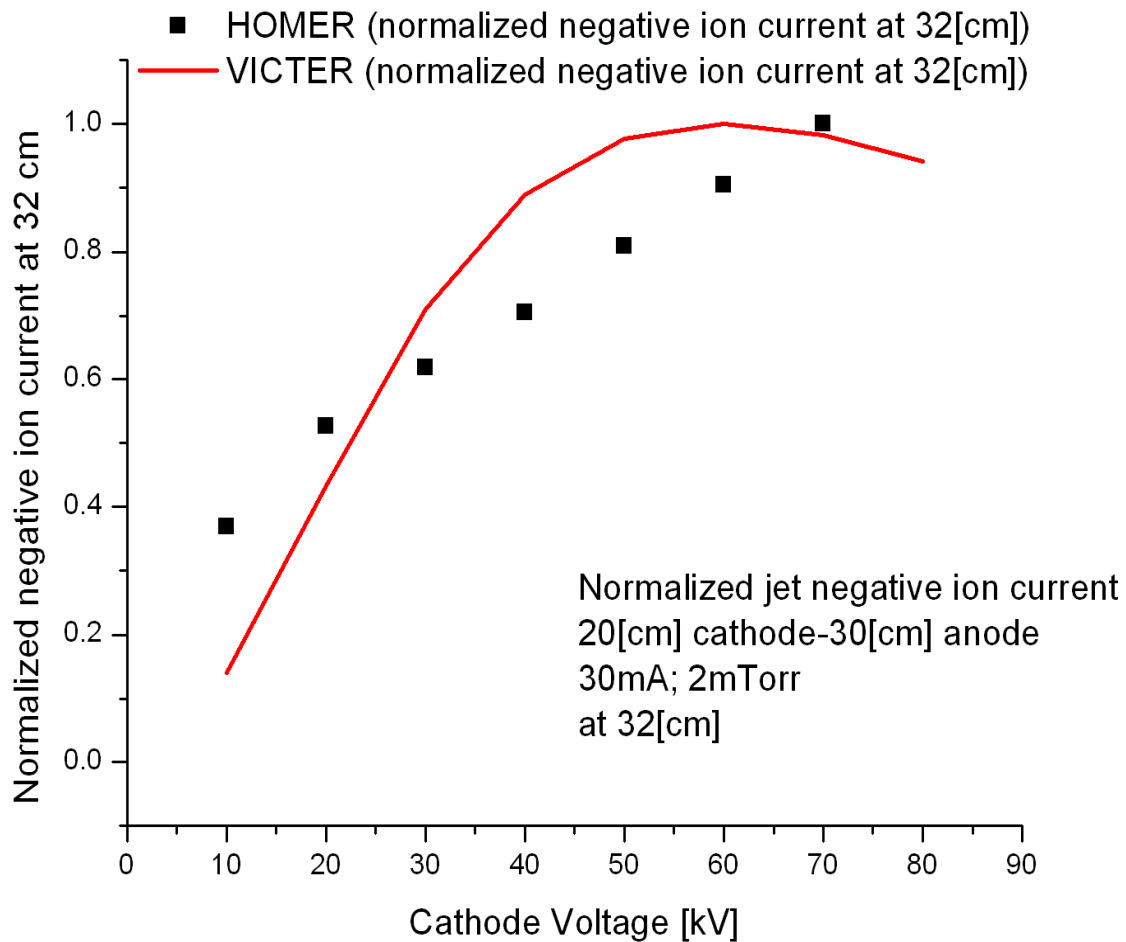


Figure VII-10: Cathode potential parametric comparison between the VICTER negative ion subroutine and Faraday cup measurements in the HOMER IEC device at 32 cm from the center of the potential well. This comparison shows qualitatively similar behavior, but differences in slope are evident.

The results of this parametric comparison are mixed. While the general trends agree, the slopes of the normalized currents have limited agreement. The VICTER prediction shows a rollover in negative ion current beyond 60 kV, which is not apparent in the Faraday cup measurements in

the HOMER IEC device.

The normalized cathode current parametric scan measurements showed a linear relationship with negative ion current in a jet. Using the previously discussed method of summing over the azimuthal angle at constant parametric conditions, we compare the dependence of the cathode current with the VICTER prediction in fig. VII-11.

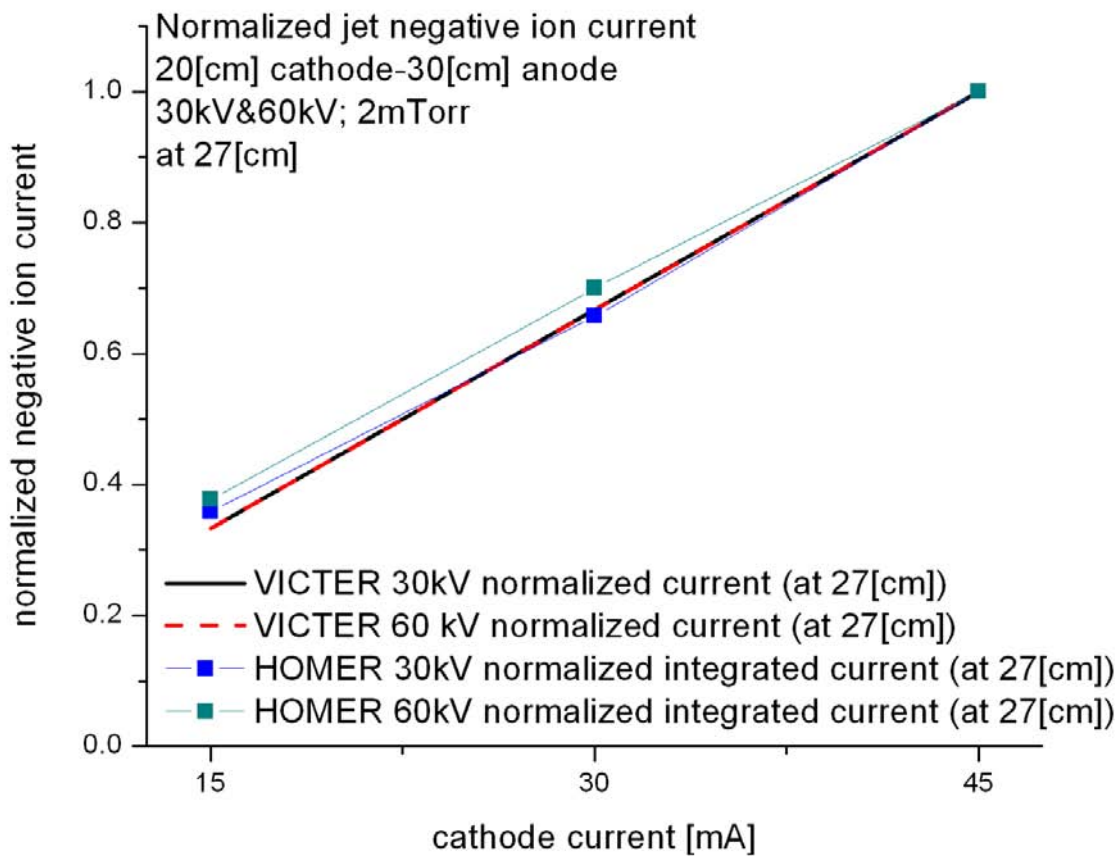


Figure VII-11: Cathode meter current parametric comparison between the VICTER negative ion subroutine and Faraday cup measurements in the HOMER IEC device at 27 cm from the center of the potential well. This comparison shows good agreement in highly linear behavior.

This comparison shows very good agreement between the VICTER prediction and the measured cathode current parametric scan. Both show a factor of 3 increase in negative ion current as the cathode meter current increases from 15 to 45 mA. This holds true at 30 kV and 60 kV potential applied to the cathode.

Finally, negative ion dependence on pressure in an IEC device is examined for parametric comparison. Unfortunately this parametric scan had very poor agreement between the VICTER prediction and Faraday cup measurement in the HOMER IEC device, as shown in figures VII-12&13.

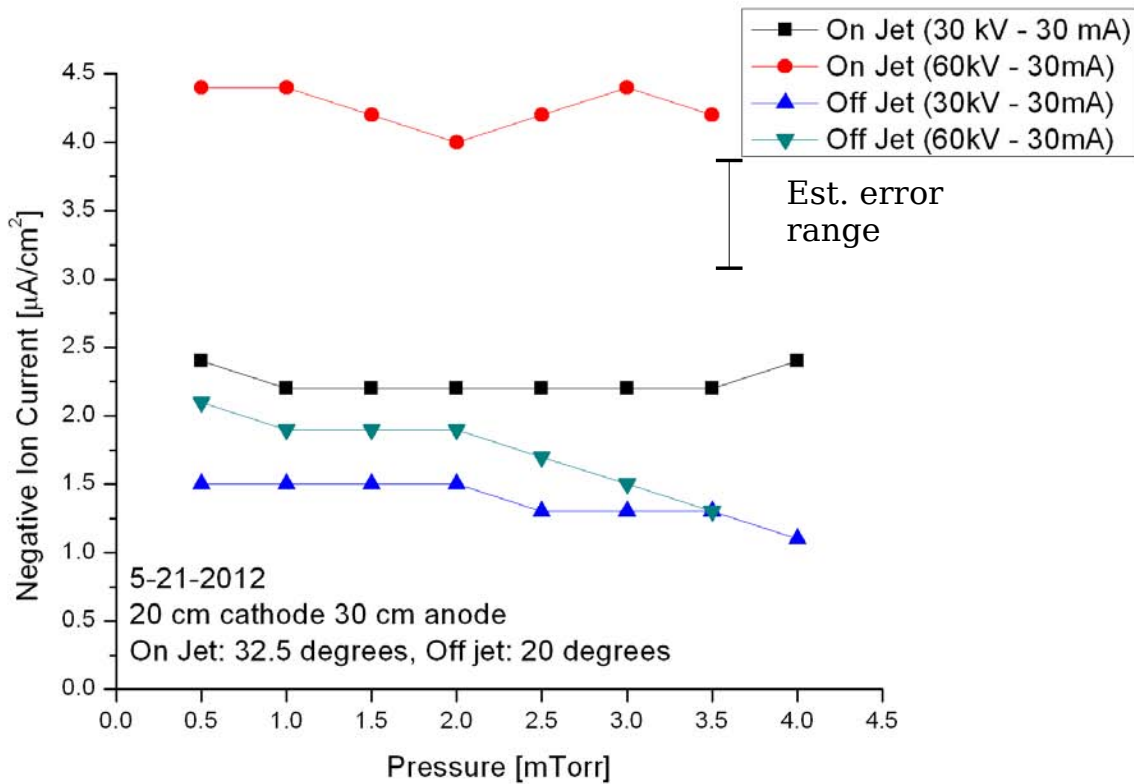


Figure VII-12: Pressure parametric negative ion measurements in the HOMER IEC device, on and off jet, with a 30 kV potential and 60 kV potential on the cathode and 30 mA supplied to the cathode. This parametric scan shows the negative ion current is essentially insensitive to chamber pressure, so long as cathode potential and supplied current are constant.

This experimental result is surprisingly insensitivity to pressure. The negative ion current must necessarily drop to zero at 0 mTorr, but the cathode current cannot be sustained at that pressure either, so the parametric scan was not extended to below 0.5 mTorr. The Faraday trap measurement in Dr. Boris' research showed roughly a factor of 2 increase from 0.5 mTorr to 2.5 mTorr and a factor of 2 decrease from 2.5 mTorr to

4 mTorr in negative ion current [VII-3]. The reason for the difference in behavior not apparent.

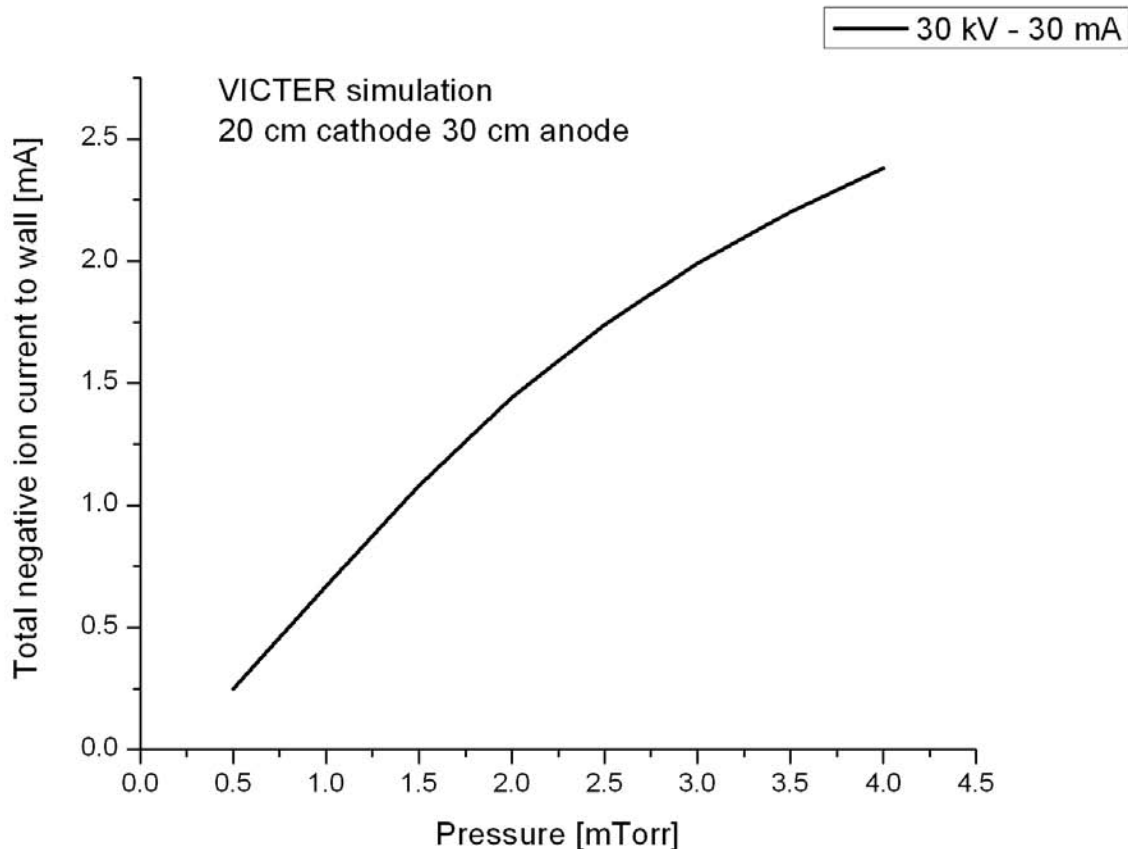


Figure VII-13: Pressure parametric negative ion prediction by the VICTER negative ion subroutine 30 kV potential on the cathode and 30 mA supplied to the cathode. This parametric scan predicts the negative ion current is highly sensitive to chamber pressure, even when cathode potential and supplied current are constant.

The VICTER negative ion subroutine results show negative ion current strongly dependent on background pressure, with an increase of nearly a factor of 10 between 0.5 mTorr and 4 mTorr, with no other change in IEC device conditions. This contradicts the measurements in the HOMER IEC

device, which only showed between 11% and 33% change in the negative ion current over the same range, and the trend for this change was a decrease at the high end of the examined pressure range. The author and Emmert, two of the authors of the VICTER code, have examined the code for errors that would account for the vastly different pressure response, but no error has been found at this time. The response of negative ions to voltage and pressure requires further study.

VII.3: Negative ion jet profiles and extrapolations

The jet profile clearly responds to cathode potential and radius in somewhat unexpected ways. The qualitative response of the jet profile to cathode potential can be seen in figures VI-31 and 32. At low cathode potential the jet profile is more flat than at high cathode potential where the jet profile is more peaked. The comparison of percent increase from the profile minimum to maximum taken from fig. VI-31 in the 27 cm case and fig. VI-32 in the 32 cm case is in table VII-1.

cathode potential	30 kV	60 kV
radius		
27 cm	~33%	~56%
32 cm	~40%	~100%

Table VII-1: Percent increase from plasma jet negative ion profile minimum to maximum at 30 kV and 60 kV potential applied to the cathode for an IEC device with a cathode diameter of 20 cm and an anode diameter of 30 cm, operating at 2 mTorr. The profile used at 27 cm is shown in fig. VI-31 and the profile used at 32 cm is shown in fig. VI-32.

The data shows a trend of the plasma jet negative ion profile peaking increasing with potential on the cathode and radius. This peaking is a separate consideration from the magnitude of negative ion current, which increases with potential on the cathode and decreases with radius.

Qualitatively, the jet evolves from a flatter profile with low voltage applied to the cathode, and becomes more peaked as more negative voltage is applied to the cathode. Further study is warranted to determine what implications this has for our understanding of the potential structure at the cathode.

Further study needs to be carried out on the plasma jet negative ion profile to better determine how the profile changes with radius. This requires both measurement of the profiles at a series of radii and higher resolution scans that can be deconvoluted to produce a more accurate

profile.

The left jet and the central jet in the Faraday cup's azimuthal field of view, shown in figures VI-27 and 28, show qualitatively different behavior. The central jet shows a behavior that we might expect, where the profile at the larger radius is similar to the profile at the smaller radius, only decreased in magnitude. The resemblance is particularly good at high voltage where the structure is more peaked. In the left jet, the data taken with a 30 kV potential on the cathode shows largely similar profiles at 27 cm and 32 cm from the center of the chamber, but at 60 kV potential on the cathode the profiles are more peaked but the peak is broader at 32 cm than at 27 cm. The peak current measured at 32 cm is only slightly lower than at 27 cm, suggesting there is more current in the jet at 32 cm than 27 cm. Further study is warranted on the variation between jets and their evolution with radius and cathode potential.

Finally, we would like to extrapolate these measurements to predict the total negative ion current produced in a jet and the IEC device. These predictions will be performed for the 27 cm distance from the center of the chamber, as the Faraday cup azimuthal resolution was 2.5° , which produces sub millimeter overlap between Faraday cup aperture positions, if the angular positioning is correct. These extrapolations are done with the caveat, that they are based on the azimuthal profile only, but are applied to the entire system, and also variation among the jets has been demonstrated.

At 20 kV potential on the cathode and 30 mA meter current, the negative ion profile is flat within the variation of the measurement, with an average of $1.5 \mu\text{A}/\text{cm}^2$. In the cathode with the diameter 20 cm, the distance between cathode longitude wires is 3.9 cm, while the distance between the latitude wires spanning the equator is 2.8 cm. This produces a hole with an area of roughly 11 cm^2 . Projecting out this solid angle to a sphere with a radius of 27 cm, the longitudinal width is 10.6 cm and the latitudinal height is 7.6 cm. The area of this solid angle at a radius of 27 cm is roughly 80.6 cm^2 . This yields a total negative ion current in the jet of of 120 μA , or 0.4% of the meter current, which seems like a reasonable first order extrapolation.

Extrapolating a more peaked profile requires more analysis. We will use the terminology of elevation and azimuth for purposes of orientation in the spherical coordinate system, as shown in fig. VI-14.

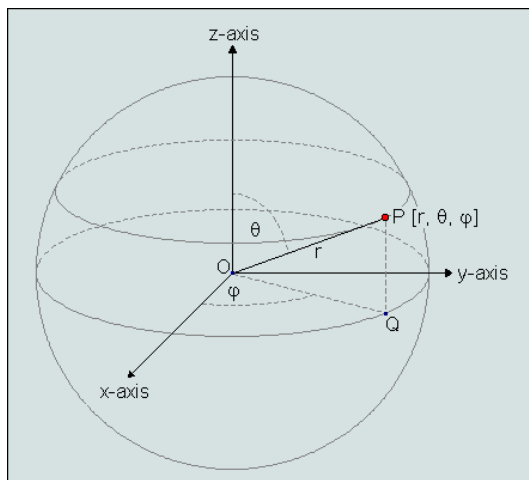


Figure VII-14: Spherical coordinate system, where azimuth is labeled by the symbol φ , and elevation is labeled by the symbol θ .

At 2.5° resolution 27 cm from the center of the cathode, the Faraday cup with a 1 cm^2 collection area reads 11 positions, nearly 1 cm apart, across a jet at the equator with nearly no overlap. Across the elevation of the same jet at 27 cm the Faraday cup would read 9 positions with the same resolution and distance apart.

We assume the azimuthal profile across the equator is the peak profile as it is in the center of the elevation range of the jet at the equator. The extrapolation is begun by plotting the negative ion current profile across the center of the elevation of the cathode hole (the equator) projected to 27 cm, as in fig. VI-15. We'll let this measured profile be represented by the function $f(x)$, whose values are given by Faraday cup measurements.

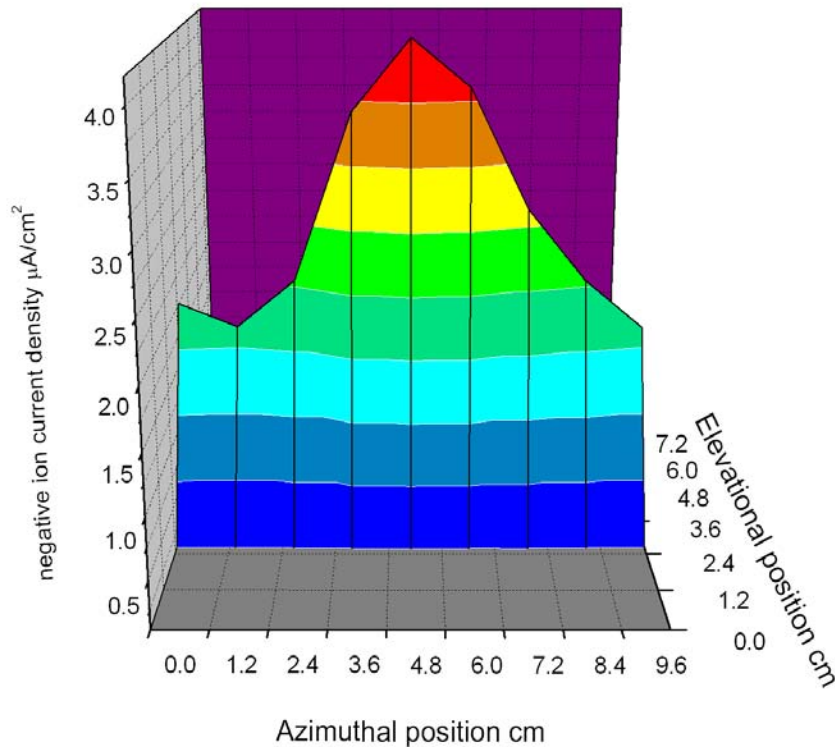


Figure VII-15: Faraday cup measurement of the azimuthal profile of the negative ion current in an IEC device plasma jet with a cathode of diameter 20 cm and anode of diameter 30 cm, with 30 kV potential on the cathode, 30 mA meter current and a pressure of 2 mTorr, taken 27 cm from the center of the cathode. This profile is taken at the center of the elevation range (the equator of the cathode).

This profile can be assumed for the peak elevation profile as well, at the center of the azimuthal range in the jet. This profile will be called $g(y)$, where $g(y)=f(x*7.6/10.6)$, thus the width of the azimuthal profile is normalized and applied to the elevation profile. A linear interpolation is used to pick negative ion current at the 9 positions the Faraday cup aperture would take in an elevation scan of the same resolution as the azimuthal scan. A picture of this extrapolation is shown in fig. VII-16.

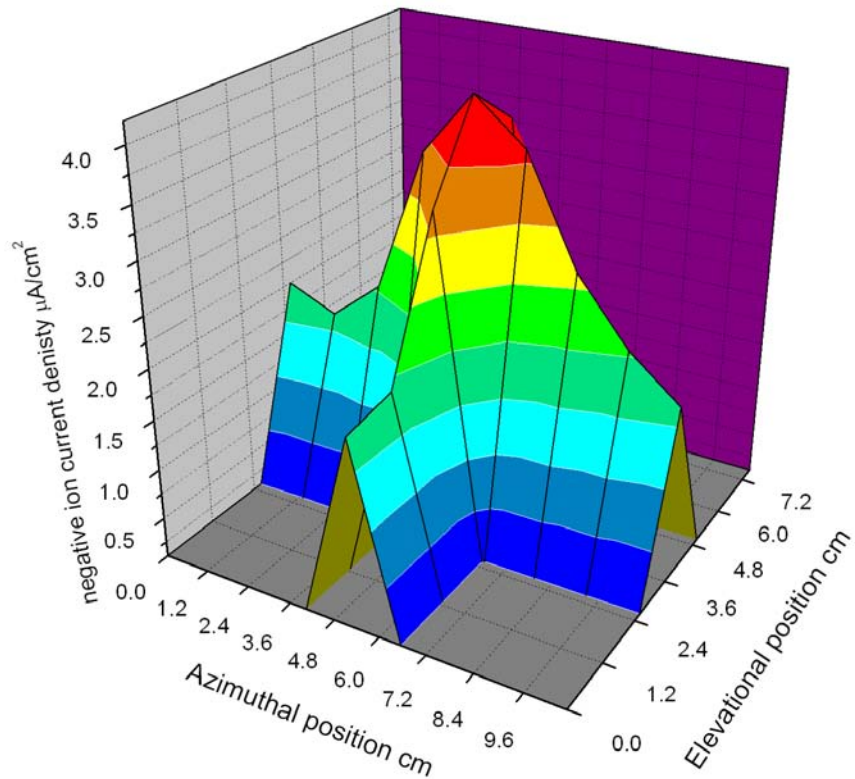


Figure VII-16: The azimuthal profile is the same as in fig. VII-15, the profile about the center of the elevation is based on normalizing the width, and interpolating the positions in the profile.

To interpolate the profile between the center of the azimuth and elevation profiles the formalism of $h(x, y) = \sqrt{f^2(x) + g^2(x)}$ is used. This produces the profile in fig. VII-17.

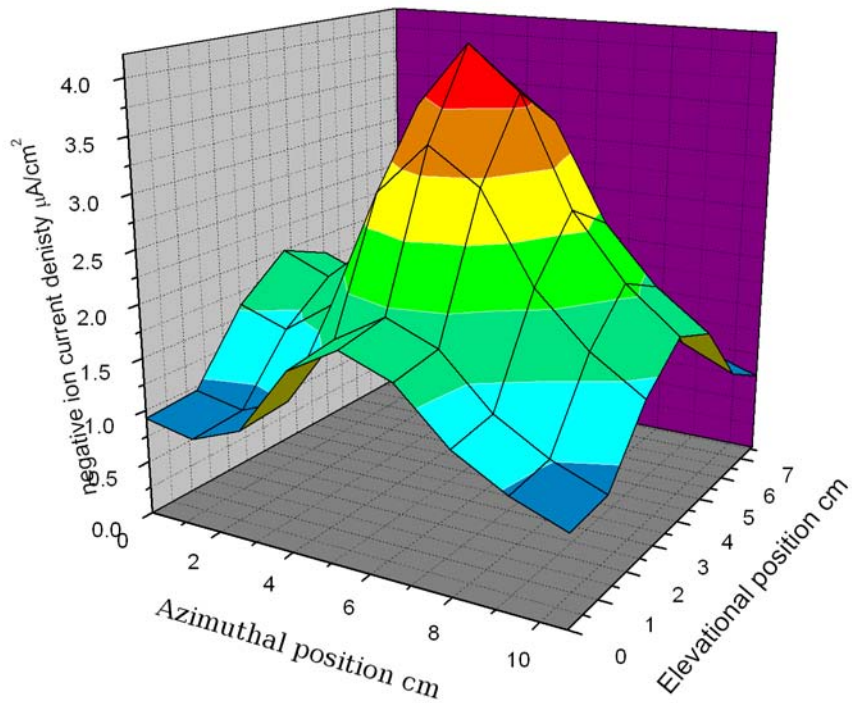


Figure VII-17: This full extrapolation is extend from fig. VII-16, with the profile between the peak azimuthal and elevation profiles inferred from the product of the peak azimuthal and elevation profiles.

Summing the total extrapolated negative ion current in this profile suggests the jet under consideration has a little more than 100 μA in it, or 0.3% of the current supplied to the cathode.

Extrapolating this number to the 264 grid holes in this cathode is almost certainly incorrect, as that would suggest a total negative ion current of 29.97 mA, which is more than 99% of the meter current provided to the cathode, leaving none of the meter current as ion impact and electron emission. It is expected the negative ion current will be weaker near the poles due to the geometric spacing of the holes in the cathode and

interference from the stalk that provides the potential to the cathode. Further study will be needed to make a more accurate extrapolation.

A number of broad observations about IEC device operation in deuterium can be drawn from this discussion and analysis of results presented in this chapter:

- Radial parametric comparisons between the VICTER negative ion subroutine results and the Faraday cup measurements in the HOMER IEC device show reasonably good agreement when normalized. These comparisons were made in an IEC device with a cathode diameter of 20 cm and anode diameter of 30 cm, between 25 and 36 cm from the center of the cathode. Over this range the negative ion current density decreased with radius, but the amount of change was dependent on the cathode potential and meter current.
- The comparison of energy spectra predicted by the VICTER code and its negative ion subroutine and measured by the MDEA diagnostic show some elements of agreement in qualitative shape and spread of the negative ion energy spectrum, but the numerical magnitude of the energy spectrum has significant disagreement.
- Comparisons between normalized negative ion current densities predicted by the VICTER negative ion subroutine and normalized Faraday cup measurements of negative ion current densities in the

HOMER device show similar trends in response to change in potential on the cathode, but the agreement is not particularly striking.

- Comparisons between normalized negative ion current densities predicted by the VICTER negative ion subroutine and normalized Faraday cup measurements of negative ion current densities in the HOMER device show very good, highly linear agreement in response to change in current supplied to the cathode, with a factor of three increase in negative ion current from 15 mA to 45 mA cathode meter current.
- The dependence of negative ion current on background D₂ pressure was shown to be mostly insensitive by the Faraday cup measurement in the HOMER IEC device. In contrast, the VICTER code predicts a strong dependence of negative ion current on background pressure, predicting behavior that is not at all similar to measurement.
- Results where trends between the VICTER predictions and measurements in HOMER disagree require further scrutiny.
- The negative ion profile in the plasma jet became more peaked with cathode potential at all observed radii. The current for the 32 cm radius measurement was lower in magnitude but had a more centrally peaked profile than was the case for the 27 cm measurement.

- [VII-1] G. A. Emmert and J. F. Santarius, "Atomic and molecular effects on spherically convergent ion flow. I. Single atomic species," *Physics of Plasmas*, vol. 17, pp. 013502, 2010.
- [VII-2] G. A. Emmert and J. F. Santarius, "Atomic and molecular effects on spherically convergent ion flow. II. Multiple molecular species," *Physics of Plasmas*, vol. 17, pp. 013503, 2010.
- [VII-3] D. R. Boris, "Novel Diagnostic Approaches to Characterizing the Performance of the Wisconsin Inertial Electrostatic Confinement Plasma," Ph.D. Thesis, University of Wisconsin - Madison, 2009.
- [VII-4] D. R. Boris, E. C. Alderson, et al., "Deuterium anions in inertial electrostatic confinement devices," *Physical Review E*, vol. 80, no. 3, p. 036408, 2009.
- [VII-5] D. C. Donovan, "Spatial Profiling Using a Time of Flight Diagnostic and Applications of Deuterium-Deuterium Fusion in Inertial Electrostatic Confinement Fusion Devices," Ph.D. Thesis, University of Wisconsin - Madison, 2011.
- [VII-6] A. V. Phelps, "Collisional kinetics of non-uniform electric field, low-pressure, direct-current discharges in H 2," *Plasma Sources Science and Technology*, vol. 20, no. 4, p. 43001, 2011.

VIII: Conclusions

Plasma jets observed in an IEC device operated with a deuterium gas are believed to consist of 4 types of energetic species:

- Positive ions
- Electrons
- Fast neutrals
- Negative ions

Outside the anode only the latter three are energetic (within the approximation that the potential is flat outside the anode). This work has extended the original discovery of a substantial negative ion current in an IEC device, by modeling this population and measuring the radial and azimuthal profiles of negative ion current.

VIII.1: Measurements of negative ions in an IEC device

- Radial and azimuthal profiles of negative ions fluxes in IEC device plasma jets have been measured and characterized outside of a mostly transparent anode, leading to the following conclusions.
 - Jets exist in an IEC device, even in conditions where spectroscopic emission from the plasma jets is not visible to the eye.

- The radial spatial profile showed the negative ion current density decreased with increasing radius outside an anode of an IEC device, but the radial dependence and absolute amount of decrease was dependent on the cathode potential.
- The azimuthal profile evolves with cathode potential and radius from the center of the cathode. While the magnitude of the negative ion current is reduced at larger radius, the jet is more peaked at larger radius: in the IEC device studied, at 32 cm the maximum negative ion flux measured in a jet is twice the minimum at 60 kV, while at 27 cm the maximum is only 56% higher than the minimum at the same conditions.
- The magnitude of the negative ion current in a jet changed with supplied cathode current, increasing linearly by a factor of three from 15 mA to 45 mA supplied to the cathode.
- Negative ions in plasma jets show limited response, outside the error of the observation, to changes in which electron emitting filaments provide the source plasma. There were isolated observations where the current changed as much as a factor of three in response to the location of the electron emitting filaments.
- Negative ions currents seem insensitive to time dependent IEC device parameters, e.g. cathode temperature, as evident by hysteresis scans.

- The background pressure in an IEC device appears to produce little perturbation to the negative ion current between 0.5 and 2 mTorr, with a measured decrease between 11% and 33% when the pressure is increased from 2 to 4 mTorr.
- Extrapolations of the negative ion current in the jet studied suggest that the negative ion current in that specific jet is on the order of 0.3 – 0.4% of the current supplied to the cathode. Analysis shows that extending the extrapolation of the negative ion current in a single jet at the equator of an IEC device predict negative ion creation in the entire device would be erroneous.

VIII.2: Negative ion subroutine in the VICTER code

- The negative ion subroutine in VICTER has enhances the simulation capability of the VICTER code by improving the code accuracy and providing a new set of benchmarks to compare against.
- The negative ion subroutine in VICTER results shows reasonably good agreement with Magnetic Deflection Energy Analyzer (MDEA) results in the shape of the negative ion energy spectrum and spread of the energy range, but the VICTER negative ion subroutine predicts a softer energy spectrum than the MDEA results. It is not yet clear what the real negative ion energy spectrum is, and further study in both VICTER and the MDEA is warranted.

- It is difficult to make direct comparisons between the one dimensional VICTER simulations and experimental measurements from an IEC device where the potentials are three dimensional. However, normalized VICTER results and Faraday cup measurements of negative ion currents show good agreement in trends for the response to variations in radius and cathode current.
- The VICTER simulations and Faraday cup measurements show broadly similar trends in the response of negative ion current to cathode potential.
- VICTER results suggest negative ion currents have strong dependence on system pressure, while the Faraday cup results suggest the system is relatively insensitive to pressure for constant cathode voltage and current. This disagreement requires further study.

VIII.3: Related work

- An analytic expression for the equivalent of the mean free path of a sequence of reactions of arbitrary number has been derived and can be applied to numerous fields of study. As applied to the creation of negative ions, this analysis suggests most negative ions in an IEC device come from fast neutrals.

- A system has been designed and constructed that is able to safely deliver up to 300 kV and hundreds of milliamperes of current to one of four experiments via an arrangement of movable electrodes. This system has selectable inline resistance and a switchable capacitor system for pulsing operation. This switching system is undergoing final qualification testing and will be implemented for future IEC device experiments.

IX: Future work

The study of negative ions in IEC devices is still in the early stages, and can be extended in a variety of ways:

- The MDEA negative ion energy spectrum calibration requires further analysis. VICTER's implementation of the negative ion simulation also needs further examination in light of the discrepancies with the MDEA results. The product of this study should be used to benchmark the prediction of the energy spectrum from the VICTER negative ion subroutine.
- The profile measurements must be extended to achieve a more complete understanding of negative ions in a gridded IEC device and perform reliable extrapolations.
 - Measurements should be taken of the elevation profile (i.e. above and below the equator).
 - Measurements should be taken across a wider azimuthal area to examine variation between jets. Variation between jets at various anode-cathode grid-wire orientations should be examined also.
- Finer motion control of the Faraday cup should be pursued to produce higher resolution profile measurements of the plasma jet in an IEC device.
- Experimental measurements of electrons and fast neutrals in IEC device plasma jets should be undertaken.

- Study of plasma jets in IEC devices of varying cathode and anode diameters should be explored as a means maximize or minimize negative ion production, and provide another way to benchmark the VICTER code.
- Benchmarking of the VICTER code needs to be continued in the context of further MDEA and Faraday cup results.